Theoretical Investigations in Vibrational Spectroscopy

by

Douglas R. Beck

A dissertation submitted in partial fulfillment
of the requirements for the degree of

Doctor of Philosophy

University of Washington

1996

Approved by 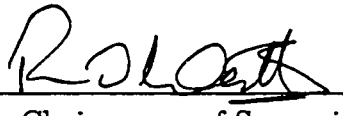
Chairperson of Supervisory Committee

Program Authorized
to Offer Degree Chemistry

Date June 5, 1996

In presenting this dissertation in partial fulfillment of the requirements for the Doctoral degree at the University of Washington, I agree that the Library shall make its copies freely available for inspection. I further agree that extensive copying of this dissertation is allowable only for scholarly purposes, consistent with "fair use" as prescribed in the U.S. Copyright Law. Requests for copying or reproduction of this dissertation may be referred to University Microfilms, 1490 Eisenhower Place, P.O. Box 975, Ann Arbor, MI 48106, to whom the author has granted "the right to reproduce and sell (a) copies of the manuscript in microform and/or (b) printed copies of the manuscript made from microform."

Signature Douglas L Beck

Date June 26, 1996

University of Washington

Abstract

Theoretical Investigations in Vibrational Spectroscopy

by Douglas R. Beck

Chairperson of the Supervisory Committee: *Professor* Robert O. Watts

Department of Chemistry

Radiationless Transitions

Franck-Condon factors govern many important molecular processes, including electronic spectroscopy and radiationless transitions. Those processes that are classified as "vertical" transitions are well understood via the Franck-Condon principle and involve large overlaps. On the other hand, those that fall in the "nonvertical" transition category are more problematical. Not only are the overlaps small, the nuclei must tunnel from one configuration to another in order for the processes to occur, i.e. they are highly nonclassical. Consequently, our usual intuitions based on the Franck-Condon principle may fail. Thus, it is our goal to provide a framework whereby we may establish new intuitions to understand these processes. We adopt

the concept of accepting modes and develop a technique which generalizes these to accepting *zones* in phase space.

Helium Clusters

Currently, much research concentrates on elucidating the properties of helium clusters by probing how they affect embedded impurities. A Diffusion Monte Carlo study was conducted to calculate frequency shifts for the asymmetric stretch, symmetric stretch, and bend fundamentals of a water monomer embedded in helium clusters. We included all degrees of freedom in the simulation and studied clusters ranging in size from one to fifteen helium atoms. The asymmetric stretch fundamental exhibits a red shift for most cluster sizes studied and is on the order of $1.5\ cm^{-1}$. To the contrary, the symmetric stretch and bend fundamentals exhibit shifts to the blue in the range from 4.0 to $6.0\ cm^{-1}$. The helium cluster is not isotropically distributed about the water monomer, which may account for the differences.

Contents

Introduction

Radiationless Transitions 3

1 Introduction 4

2 Position versus Momentum Jumps 11
2.1 The traditional semiclassical perspective 11
2.2 Simple Phase Space Picture 14
2.3 One Dimensional Examples 17
2.4 Pulsed Transient Wave Packet 23
2.5 Wigner phase space analysis 26

3 Two-mode competition: separable Morse oscillators 35

4 Phase Space Analysis of Benzene Radiationless Decay 43
4.1 Historical orientation 43
4.2 Issues 44
4.3 Model 48
4.4 Method of Analysis 50

5 Results and Conclusions 52

Induced Frequency Shifts of a Water Monomer Embedded in Helium Clusters 62

6 Introduction 63

7 Diffusion Monte Carlo 68
7.1 Monte Carlo Methods 68
7.2 Evolution Operator 69
7.3 Ground State DMC 71
7.3.1 Simple Algorithm 71

7.3.2 Energy Estimates . . . 73
7.3.3 Importance sampling . . . 75
7.4 Population Renormalization . . . 77
7.5 Excited State Fixed Node DMC . . . 78

8 Excited State Dynamic-Node DMC **81**
8.1 Introduction . . . 81
8.2 Theory . . . 82
8.3 One Dimensional Morse Oscillator . . . 84
8.3.1 System Description . . . 84
8.3.2 First Excited State . . . 85
8.3.3 Second Excited State . . . 86
8.3.4 Third Excited State . . . 87
8.4 Hydrogen Fluoride . . . 89
8.4.1 System Description . . . 89
8.4.2 $\nu = 0, l = 1$ . . . 90
8.4.3 $\nu = 0, l = 2$ . . . 91
8.4.4 $\nu = 1, l = 0$ . . . 92
8.4.5 $\nu = 1, l = 1$ . . . 93
8.4.6 Results . . . 93
8.5 Future Developments . . . 95

9 System Potentials **96**
9.1 Introduction . . . 96
9.2 Water Monomer . . . 97
9.3 Helium-Water Intermolecular Potential . . . 98
9.4 Helium Interatomic Potential . . . 102

10 Trial Wave Functions **105**
10.1 Ground State . . . 106
10.1.1 Monomer Intramolecular Trial Function . . . 106
10.1.2 Monomer-Helium Intermolecular Trial Function . . . 107
10.1.3 Helium-Helium Intermolecular Trial Function . . . 108
10.2 Asymmetric Stretch . . . 108
10.3 Symmetric Stretch . . . 109
10.4 Bend . . . 109

11 Results and Conclusions **111**
11.0.1 Simulation Parameters and Errors . . . 111
11.0.2 Energies . . . 114

11.0.3 Frequency Shifts 115
11.0.4 Conclusions 124

Bibliography **129**

List of Figures

1.1 The construction of the nonclassical wings of an absorption band from the crossing of the donor and acceptor Born-Oppenheimer potential energy surfaces. 7

2.1 The overlap of two vibrational wave functions in three extreme cases where position jumps or momentum jumps dominate. 16

2.2 For cases A and B, we show schematic potential energy surfaces for the inward (A) and outward (B) displacements, and below each the corresponding phase space diagram. Case A corresponds to position jumping (or tunneling in position space) and case B, to momentum jumping. (A small component of position jump in case B can also be seen). Note the real crossing of the potential energy surfaces in case A. 19

2.3 The base 10 logarithm of the Franck-Condon factors for the two Morse oscillator cases, A and B, and the matched frequency harmonic oscillator case C are shown. Note the much more rapid decline of the Franck-Condon factors for case B as a function of energy, and the concave shape of the case A curve. Case C is for two harmonic potential energy surfaces of matched curvature to the Morse oscillators at the minimum of the potential. Using the same displacement then gives a meaningful comparison with the Morse oscillator. Note that case C has the highest fall off and is *convex*. 21

2.4 For a momentum jump case with $D_A = D_D = 20$, $a_A = 0.2, a_D = 0.26$, $b_D - b_A = 0.2$, the dips can be seen which result from interference between the $\pm p^\dagger$ stationary phase contributions. 22

2.5 Position versus momentum jump for two lightly varying Morse oscillators. The top shows a position jump scenario as is evidenced by the pulsed state produced. The bottom scenario on the other hand shows a momentum jump as is seen by the numerous oscillations in the pulsed state produced. 27

3.1 The acceptor potential energy surface contours (E=16 darkened) together with the pulse excited wave packet and the phase space density of the Wigner function of the donor ground state, ρ_d at E=16. The latter is plotted as a phase space distribution, as a series of line segments representing the momentum distribution at selected positions. The direction of a line segment shows the direction of the momentum, and its length is proportional to the magnitude of ρ_d as a function of momentum for the given position, not the momentum itself. Note that the wave packet and the phase space distribution agree on the predominantly independent bond momentum jump in this case (the wave packet is a linear combination of two symmetrically related wave packets, each with energy mostly in one bond. 40

3.2 Same as Fig. for case 2. The wave packet and the phase space distribution agree on the correlated bond position jump (the wave packet has both bonds sharing the energy simultaneously). 41

4.1 The two dimensional energy mode competition for separable harmonic oscillators. Two scenarios are illustrated. As seen, the scenario depicting most of the energy residing in the higher frequency mode results in the largest overall Franck-Condon factor, which is a product of the two one dimensional overlaps. 46

5.1 Plot of the maximum of $\ln(\rho_W)$ versus frequency of each normal mode for both C_6H_6 and C_6D_6. Each peak corresponds to the classical situation of putting all the vibrational energy into the respective normal mode, as designate by the frequency. The plot represents the "0-0" transition. 54

5.2 Same as 5.1 for the case of a transition to the designated energy. Along with the other plots, this shows how the competition ensues between modes as the energy gap is increased. 56

5.3 Same as 5.1 for the energy gap corresponding to a radiationless transition, for our model. Here, the higher frequency modes clearly dominate. 57

11.1 Ground State Energy as a function of cluster size. 116

11.2 Asymmetric stretch fundamental energy as a function of cluster size. 117

11.3 Symmetric stretch fundamental energy as a function of cluster size. . 118

11.4 Bend fundamental energy as a function of cluster size. 119

11.5 Approximate ground state radial density profiles for helium atom cluster sizes of 6, 9, 12, and 15 atoms. 120

11.6 Asymmetric stretch fundamental frequency shift as a function of cluster size. 126
11.7 Symmetric stretch fundamental frequency shift as a function of cluster size. 127
11.8 Bend fundamental frequency shift as a function of cluster size. . . . 128

List of Tables

2.1 The real and imaginary parts of the position $x^\dagger$ (and associated momentum $p^\dagger$) satisfying to $V_A(x) = V_D(x)$ as a function of the energy gap E_n of the Morse oscillator $E_n = \sqrt{2D}a(n+1/2) - \frac{1}{2}a^2(n+1/2)^2$ with $D = 25, a = 0.2$ 18

4.1 Vibrational frequencies (cm^{-1}) of C_6H_6 for the $^1A_{1g}$ and $^1B_{2u}$ states. 47
4.2 Vibrational frequencies (cm^{-1}) of C_6D_6 for the $^1A_{1g}$ and $^1B_{2u}$ states. 49

5.1 Optimum Energy Distributions. Wigner classical energy versus Franck-Condon quantum number distributions. 58

8.1 Dynamic-node, Morse first excited state simulation. 86
8.2 Dynamic-node, Morse second excited state simulation. 88
8.3 Dynamic node Morse third excited state simulation. 88
8.4 HF dynamic-node DMC results. 94

9.1 Monomer potential energy parameters, atomic units are used. 98
9.2 HFD potential parameters of Palma et al. All values are given in atomic units. 102
9.3 Water-Helium SCF associated Legendre coefficients for center-of-mass parameters. Atomic units are used. 103
9.4 Helium Interatomic Potential Parameters of Aziz 104

11.1 Comparison for DMC frequencies to the experimental values of Robertson and Williams. All energies are in wave numbers. 114
11.2 Energies and frequency shifts as a function of cluster atom mass. The cluster contained 7 atoms. 123
11.3 Approximate structural characteristics of the helium clusters for N = 6, 9, 12, and 15 helium atoms. Distances are in Å. C is the center of mass of the helium atoms. 124

ACKNOWLEDGEMENTS

The author wishes to acknowledge Professor Robert O. Watts, not only for his research guidance, but for caring and providing support; without which this manuscript may never have been written. He also wishes to thank Professor E. J. Heller for many years of invaluable research guidance. Special appreciation goes to Professor Michael J. Schurr for being supportive and for all the helpful advice through the years. The author also wishes to thank the following coworkers for their stimulating conversations and interactions: Kip Stevenson, Alexandra Goldstein, Jian Wu, Pat Heath, John Gebe, Frank Grossmann, Pedro Muiño, Susan Rempe, Jeff Delrow, John Hunter, Steve Tomsovic, Miguel Sepulveda, Song Ling and Michelle Shulman.

The author wishes to express special gratitude and thanks to Patrick William O'Connor. As well as being a great friend, he has been a mentor and has influenced the author in ways too numerous to express in written form. It is extremely likely that this dissertation may never have been written without his continual support and stimulating conversations. He was always a source of eye-opening insight and thoughtful and probing questions. He continually managed to raise issues that had never occurred to the author and to provide ingenious solutions to countless hurdles.

Last but certainly not least, special recognition goes to his wife, Renée Marie Lirette. Her support and companionship is invaluable, and makes life rewarding.

To my loving parents, Jerald and Betse Beck, whom I miss dearly.

INTRODUCTION

This doctoral dissertation is divided into two separate parts. The first part is comprised of work performed under the direction of E. J. Heller at the University of Washington. The focus of that project was to develop a theory which would elucidate the nature of the wave function produced during a nonradiative transition. The second part involves work performed under the guidance of Robert O. Watts. Here we developed and implemented a quantum simulation (Diffusion Monte Carlo) to study vibrational frequency shifts associated with embedding a water monomer in small to medium helium clusters. Following are brief introductions of the two research projects. More detailed introductions exist at the beginning of each part.

Molecular radiationless processes often involve transitions between multiple electronic states. For isolated molecules in the gas phase, the nuclear configuration must rearrange in order to conserve energy. Therefore, the question of how this molecular deformation occurs naturally arises. Typically, analyses of these processes involve calculation of Franck-Condon factors in order to understand how the energy is partitioned among the various modes in the molecule. We develop and present

a novel phase space method, based on Wigner functions, for interpreting the short time dynamics of these processes. Not only does our technique provide insight into partitioning of energy among various modes, but how the energy is deposited into these modes; in other words, must the nuclei momentum tunnel, position tunnel, or some combination of the two? We provide a derivation of the technique, based on Fermi's Golden Rule, and present an analysis for the radiationless decay of benzene.

Superfluid helium is a fascinating substance which is receiving an intense amount of research attention. In addition, helium clusters are currently the focus of much research which aims to determine if they, like bulk liquid helium, also posses superfluid properties at very low temperatures. Many researchers study the spectroscopic properties of embedded impurities in order to nondestructively probe their interactions with the cluster, with the hopes that this will give insight into this quantum fluid. We developed and implemented a Diffusion Monte Carlo algorithm to calculate the frequency shifts of an embedded water monomer in ^{4}He clusters at 0K. The clusters ranged in size from zero to fifteen helium atoms and the energy was calculated for the ground state and the first excited states for the asymmetric stretch, the bend, and the symmetric stretch modes of the monomer. The frequencies were then obtained by difference and the shifts determined relative to the isolated monomer. The specifics of the methodology and the results are presented.

Radiationless Transitions

1

Introduction

Radiative and radiationless transitions depend critically on vibrational overlap factors (Franck-Condon factors) involving eigenstates from two different Born-Oppenheimer potential energy surfaces. The Franck-Condon factors provide propensity rules which spectroscopists take almost for granted. For example, if a bending mode is by far the most displaced coordinate in one electronic state relative to another, it is assumed that states with bending excitation will be produced in an electronic transition between the Born-Oppenheimer potential energy surfaces. There may be issues of the subsequent decay of the energy of the bending motion, but the bending is considered to be initially excited.

We distinguish two regimes for Franck-Condon factors: classical and nonclassical. In the classical (vertical) regime, the usual intuition of the Franck-Condon principle

is correct. The classical regime corresponds to the realm of favorable conditions for the Franck-Condon overlap. The nonclassical (nonvertical) regime of small Franck-Condon factors and violations of the "usual intuition" is the subject of this paper.

Both radiative and radiationless transitions depend on the overlap of vibrational states normally coupled by a weak perturbation. In the radiative case, this coupling is the transition moment which is a function of the nuclear coordinates (after integrating over the electronic coordinates). Whereas in the radiationless case, the coupling is due to the nonadiabatic terms in the Hamiltonian, which again are functions of the nuclear coordinates. Given these similarities, it is useful to raise (lower) the initial Born-Oppenheimer surface by $\hbar\omega$, where ω is the frequency of the absorbed (emitted) light, and treat the radiative process much like a radiationless transition. This is feasible so long as the electronic couplings are weak (e.g. spin orbit coupling in a radiationless transition or the electromagnetic coupling in a radiative one), and the relevant coupling for a given ω takes place only between approximately degenerate vibrational states. With this slight adjustment, we can speak of both radiative and radiationless transitions simultaneously.

Consider the absorption spectrum for a bound state going to a steep part of an excited electronic state as shown in Fig. 1.1. As the incident light frequency is increased, we proceed from the "red" wing, through the band center, to the "blue" wing. Drawing a horizontal line between the two classical turning points of the

"donor" or initial surface defines the classically allowed region of the donor wave function. This surface is progressively raised by increasing $\hbar\omega$. We focus attention on the critical issue of the intersection of the two potential energy surfaces. At first, the intersection occurs to the right of the classically allowed region, then within it, and finally to the left of it as ω is increased. Representative diagrams showing the overlap of the two vibrational states are given in each of the three regions. When the surfaces cross in the classically allowed region, the overlap is good and the spectrum is near its maximum. When they cross outside the classically allowed region, the overlap is poor and corresponds to the nonclassical wings. This distinction extends to any number of dimensions, and defines the concept of the "nonclassical" region of Franck-Condon factors. Loosely speaking, when the surfaces cross in classically allowed regions, the electronic state change can occur without any instantaneous change or jump in position or momentum of the nuclear coordinates. Otherwise, in the nonclassical wings, a jump is required (i.e. tunneling for the nuclear coordinates). In two or more dimensions, it may be the case that a given state on the acceptor potential energy surface has enough energy to reach the crossing, but that its classical region does not cross the line or surface of intersection of the two potential energy surfaces. The corresponding Franck-Condon factor is nonclassical, even though it is in the classical regime; other states of nearly the same energy must necessarily straddle the crossing.

A more common situation occurs when there is a small relative horizontal dis-

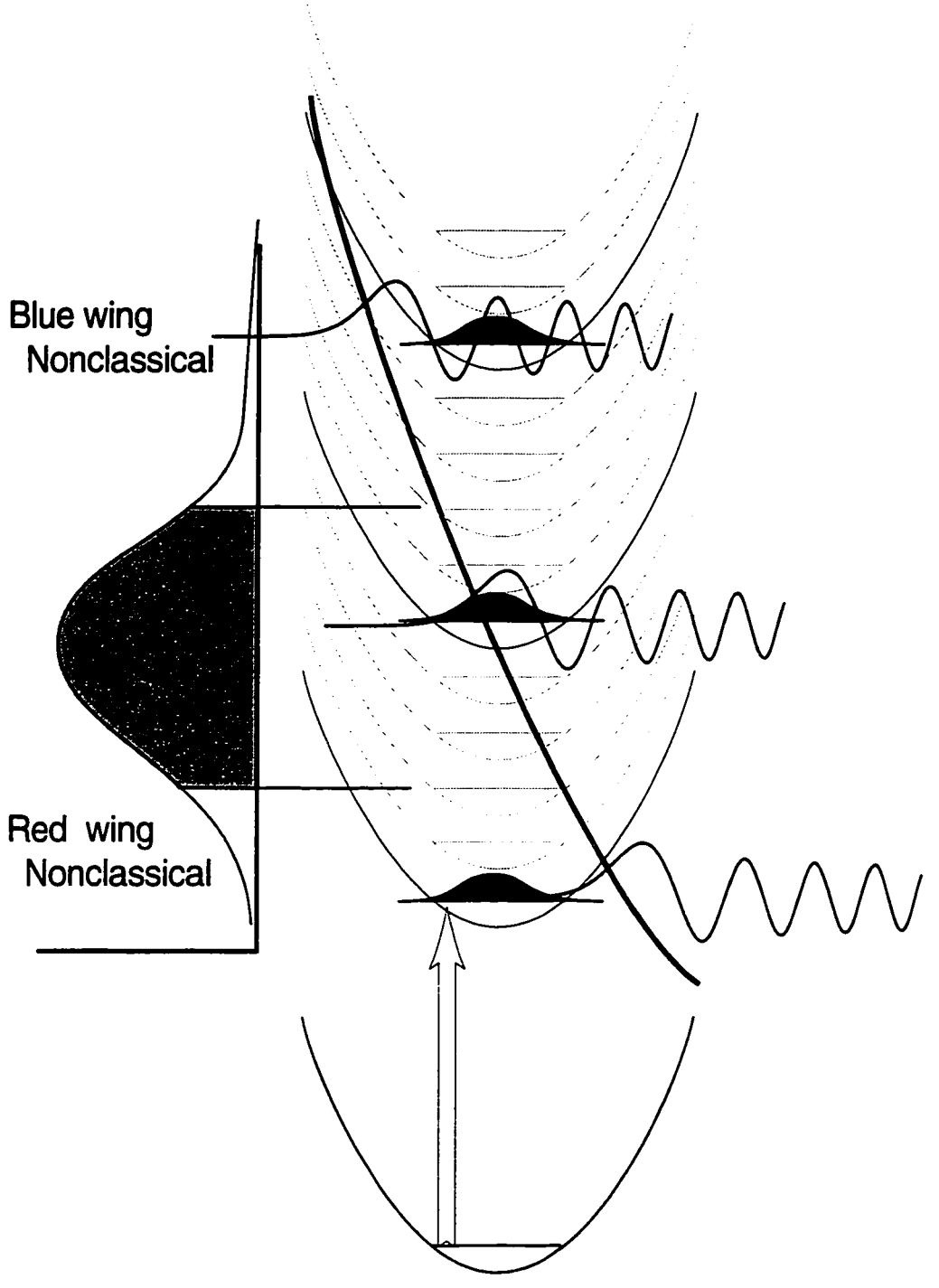

Figure 1.1: The construction of the nonclassical wings of an absorption band from the crossing of the donor and acceptor Born-Oppenheimer potential energy surfaces.

placement between the two surfaces. Thus, there is no red wing, and the blue wing starts just after the strong "0-0" transition. This case has interesting experimental implications, since by tuning to the blue of the 0-0 line the nonclassical region is reached with the potential energy surfaces nested, yet other excited potential energy surfaces may be separated enough in energy so that their interactions may be neglected. The energy gap is controlled simply by the laser wavelength allowing the spectrum and energy deposition in the excited state to be studied as a function of the energy gap. Alternatively, one could populate the ground vibrational level of the excited potential energy surface and examine the emission to the red of the 0-0 line, either *via* spontaneous emission or SEP (stimulated emission pumping) [2].

The issue is identical for radiationless transitions, except that one cannot lift the potential energy surfaces relative to each other (except for very small adjustments with external fields). Thus, the radiationless transition case is "stuck" at one value of the vertical displacement. Quite often, this value places the system in question in the nonclassical regime (as is the case for benzene during an electronic transition from the S_1 surface to the ground S_0 surface).

Nonclassical Franck-Condon factors are necessarily small, since either the amplitudes or the nodal structures (or both) of the two wave functions are incompatible. In the red wing, only the tails of the wave functions overlap; the integral is clearly small. This is shown in Fig. 1.1, bottom. In the classical region, the amplitudes

and nodes are compatible, and the overlap is large. In the blue wing, the nodes in one of the eigenstates kill the overlap even though the amplitude is fairly large for both states over a portion of coordinate space (Fig. 1.1, top). This is all well known. However, there is a subtle point about the blue wing Franck-Condon factors, since there are two possibilities for interpreting their residual value. Either the residual results from an incomplete nodal cancellation in the region of large amplitude, or, it could come from the overlapping region of the tails of the two states, which after all still contribute. While this distinction may seem almost recreational, we shall see that it leads to important effects in two or more dimensions.

We present a technique which allows us to study these processes in several dimensions. We then use it to analyze a simple model, based on a normal mode analysis, of benzene radiationless decay from the first excited singlet to the ground singlet. Given this simple model, the questions we address are: 1) Does our technique corroborate the observation that the C-H stretching modes are the best accepting modes? 2) Is the excess electronic energy shared equally or unequally among the "local" C-H stretching modes? 3) Does our model predict the radiationless decay rate decrease brought about by deuteration? Benzene serves as an ideal model since there is a wealth of data and theory to which we may compare our analysis.

The present paper compliments others from our group. In a recent study, we investigated the two and many- dimensional case of radiationless transitions which take

place *above* the crossing energy and thus in the classically allowed, vertical regime. The semiclassical picture is one of surface hopping, and the focus of [5] was the complete mode energy scrambling which hopping and re-hopping produces. The present paper is concerned with the tunneling regime and focuses on the initially prepared states, not the effect of long time dynamics.

An earlier paper [6] also dealt with the nonclassical regime, but was concerned mainly with radiationless rates as a function of excess vibrational energy. Here, we are more concerned with the overlaps as a function of electronic energy (or the "energy gap"), as well as other features of the participating Born-Oppenheimer potential energy surfaces. Also, our earlier work considered only what we shall refer to here as position jump (as opposed to momentum jump) nonclassical transitions.

2

Position versus Momentum Jumps

Before presenting our technique, we provide three alternate viewpoints in one dimension to illustrate the issues involved in a nonclassical transition. We will show how each of these viewpoints predicts whether the nonclassical transition occurs via position or momentum tunneling.

2.1 The traditional semiclassical perspective

The semiclassical eigenstates may be represented as a sum of terms of the form

$$\psi(x) \approx \frac{1}{p(x)^{1/2}} e^{i \int p(x')\, dx'} \tag{2.1}$$

A Franck-Condon overlap between two such states, with each on its own Born-Oppenheimer potential energy surface, is

$$\langle \psi_A | \psi_D \rangle \approx \int \frac{1}{p_A(x)^{1/2} p_D(x)^{1/2}} e^{-i\int^x p_A(x')\,dx' + i\int^x p_D(x')dx'}\,dx \tag{2.2}$$

The stationary phase evaluation of this integral requires

$$\frac{d}{dx}\left(-\int^x p_A(x')\,dx' + \int^x p_D(x')\,dx'\right) = 0 \tag{2.3}$$

or

$$p_A(x) = p_D(x) \tag{2.4}$$

which implies, since the total energy is the same on both potential energy surfaces,

$$V_A(x) = V_D(x). \tag{2.5}$$

This is the well known result that the semiclassical contribution arises where the potential energy surfaces cross. There may of course be more than one stationary phase point; in what follows, we shall assume we are dealing with the dominant contribution. There are two possibilities for a crossing in the nonclassical regime. If it occurs at a real value of $x^\dagger$, then the position of the crossing is real and the momentum at the crossing, $p_A(x^\dagger) = p_D(x^\dagger)$ is pure imaginary. (Real momentum *and* real position correspond to the classical regime where no "jumping" is required). This is the case of a position jump, where the contribution to the integral is coming

from the tails of the wave functions. Both $p_A(x^\dagger)$ and $p_A(x^\dagger)^*$ are stationary phase points, but one of them corresponds to exponentially increasing wave functionand is discarded.

The crossing may be at complex values of x. The momentum will no longer be purely imaginary, but will generally be complex. However, it often happens that the position is *mostly* imaginary, and the corresponding momentum is mostly real, giving a jump which is largely in momentum. If the crossing happens at $p = p^\dagger$, it also must occur for opposite sign $p = -p^\dagger$. For pure imaginary momentum, this is the same as $p^{\dagger *}$, but now, counting the discarded solutions giving rise to increasing rather than decreasing wave functions in the classically forbidden region, there are four stationary phase momenta. Two are discarded leaving two still remaining. There may be constructive or destructive interference between these distinct but equal magnitude stationary phase amplitudes. This fact was noted already by Medvedev [8] and separately by Child [7]. An example of this will be seen below, where the system cycles through constructive and destructive interference as a function of the energy gap. Of course, intermediate cases more evenly split between position and momentum tunneling can also arise.

Given two potential energy surfaces, it is possible to infer the propensity (as a function of the energy gap) for position *versus* momentum tunneling or jumping using Eq. (2.5). This is a very direct and convenient tool.

Objections might be raised to the representation of the vibrational state of the upper Born-Oppenheimer surface by its semiclassical form, because we often take it to be the ground state, which is seemingly a dubious candidate for semiclassical approximation. At a very simple level, we may note that we are using the semiclassical form only in the classically forbidden region, and normally deeply within it. As pointed out long ago by Miller [9], semiclassical approximations should work well so long as the absolute value of the momentum is large enough. At a more exact level, we note the work of Nikitin [10] which builds on the work of Landau and Lifschitz [11], showing how semiclassical matrix elements involving even the ground vibrational state may be accurately given. We have verified related formulae for the Franck-Condon factors for two Morse potentials, but the qualitative discussion given here is sufficient, and the detailed semiclassical theory will be omitted. In this case, the technology of the detailed semiclassical theory is neither so well developed nor the insight so keen as to warrant its presentation.

2.2 Simple Phase Space Picture

A foundation for intuition for nonclassical Franck-Condon factors is provided in Fig. 2.1. Shown there are the coordinate space plots for three nonclassical situations, and to the right in each case are the corresponding phase space pictures. The top most case is the straightforward overlap of the "tails" of the wave functions. We

denote this case a position jump because, as we shall see, the amplitude may be thought of as leaving the initial donor state, and appearing near the turning point region of the repulsive, accepting potential. The phase space picture to the right shows approximate locations of the Wignerphase space density of each of the two states. The two distributions do not overlap; if they did, the Franck-Condon factor would belong to the classical variety. However, it is easy to see that the nearest path between the two states involves a position shift at zero momentum.

The middle case in Fig. 2.1 shows a narrowed and shifted Gaussian overlapping the same second state. Because the Gaussian is so narrow, the oscillations of the second function are not so effective at killing the integral, and at the same time the tail of the Gaussian is vastly diminished. There is no doubt that the overlap, while still small, comes from the region where the Gaussian is large. We call this a momentum jump case, because the amplitude leaving the Gaussian state may be thought of as appearing near the Gaussian, with considerable momentum, on the repulsive potential. The phase space picture shows the shifted location of the Gaussian in coordinate, but also reflects the increased momentum uncertainty and decreased position uncertainty associated with the narrow coordinate space distribution. It is clear, that a shift in momentum at (nearly) constant position gives the shortest path between the two distributions.

Finally, at the bottom in Fig. 2.1 we see a much wider Gaussian centered as in the

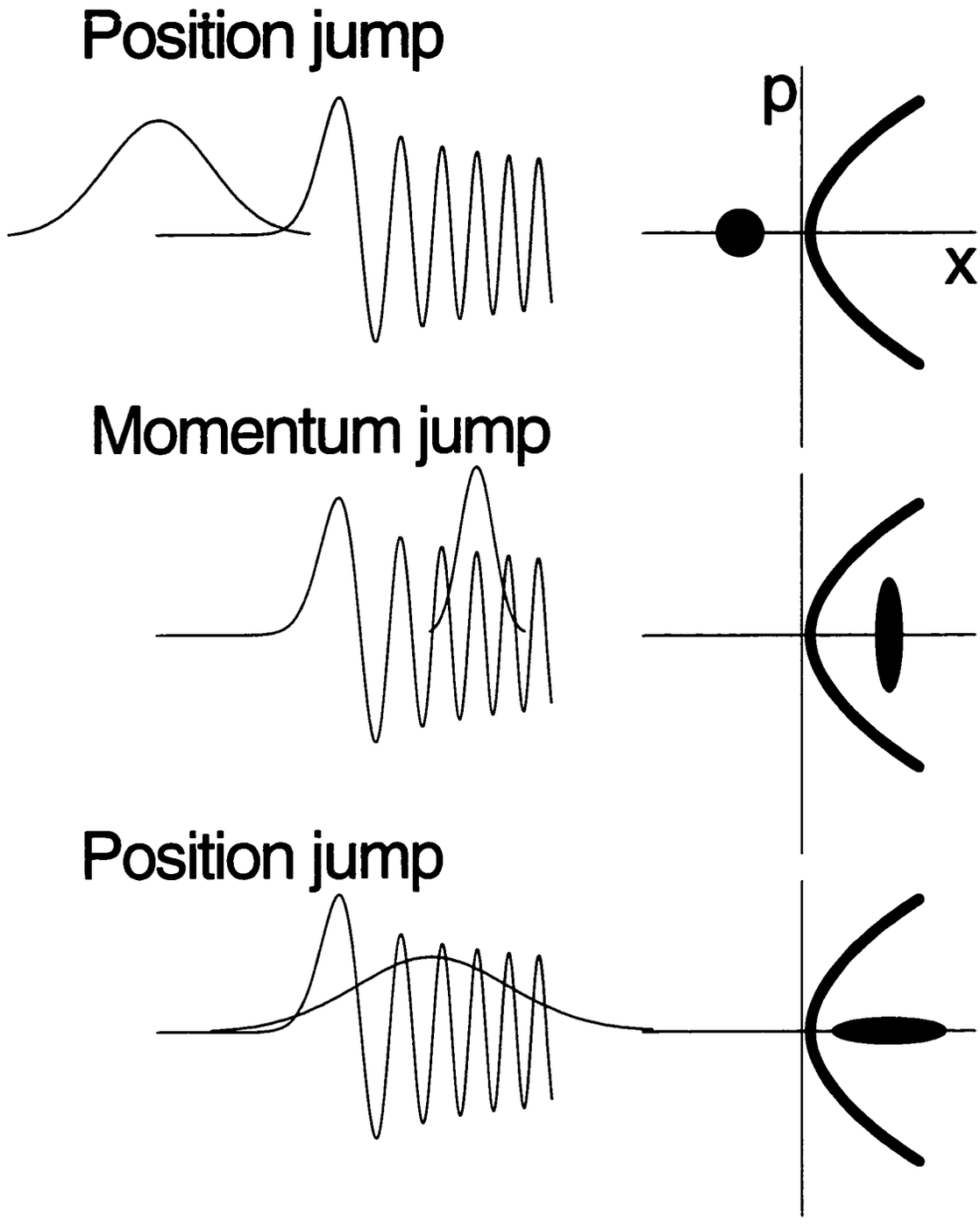

Figure 2.1: The overlap of two vibrational wave functions in three extreme cases where position jumps or momentum jumps dominate.

previous case. A glance at the wave function plot shows there is now good overlap of the tails, and a much more complete cancellation of the integral in the oscillatory region. The integral is coming mostly from the region of the tails, and the phase space plot shows that a position jump (again at zero momentum) gives the shortest path between the two states.

2.3 One Dimensional Examples

We first consider two Morse potentials differing by only a coordinate displacement. We examine the ground state (acceptor) Morse potential

$$V_A(x) = D_A\{1 - \exp[-a_A(x - b_A)]\}^2 \tag{2.6}$$

and the excited state (donor) potential

$$V_D(x) = D_D\{1 - \exp[-a_D(x - b_D)]\}^2 + E_0 \tag{2.7}$$

We take, in dimensionless units, $D_A = D_D = 25$, $a_A = a_D = 0.2$, and cases A, $b_D - b_A = -0.1$, and B, $b_D - b_A = 0.1$. Case A represents an inward displacement of the upper potential energy surface; case B, and outward one. In Fig. 2.2, we see coordinate space and phase space pictures of the two cases. In the upper part of Fig. 2.2, the potential energy surfaces are shown, and in the lower part we see the corresponding phase space diagram. It is evident why case A should be a position

jump, and case B (mostly) a momentum jump. The real crossing of the potential energy surfaces in case A is shown. The surfaces do not cross for any real x in case B.

These qualitative conclusions are augmented by the position and momentum of the crossing as a function of energy. They are shown for cases A and B in Table 2.1. The inward and outward displacements have drastically different behavior. Case A leads to real crossings in x with pure imaginary momentum while Case B leads to complex values of both variables, with the real part of the momentum dominating the imaginary part.

Table 2.1: The real and imaginary parts of the position $x^\dagger$ (and associated momentum $p^\dagger$) satisfying to $V_A(x) = V_D(x)$ as a function of the energy gap E_n of the Morse oscillator $E_n = \sqrt{2D}a(n+1/2) - \frac{1}{2}a^2(n+1/2)^2$ with $D = 25, a = 0.2$

	Case A (position jump)		Case B (momentum jump)	
	$x^\dagger$ (Re,Im)	$p^\dagger$ (Re,Im)	$x^\dagger$ (Re,Im)	$p^\dagger$ (Re,Im)
$n=1$	(-3.02 , 0.)	(0., ±8.82)	(-1.18, 5.80)	(8.28 ,-3.48)
$n=2$	(-4.07, 0.)	(0., ±11.16)	(-2.72,6.36)	(11.68, -3.49)
$n=3$	(-4.75, 0.)	(0., ±13.12)	(-3.64, 6.62)	(14.24, -3.49)
$n=4$	(-5.25, 0.)	(0., ±14.82)	(-4.29, 6.77)	(16.33, -3.49)
$n=5$	(-5.66, 0.)	(0., ±16.32)	(-4.79, 6.88)	(18.13,-3.50)

The Franck-Condon factors for the two cases are shown in Fig. 2.3. Also shown are the Franck-Condon factors for a pair of harmonic oscillator potentials matched to the Morse potentials of cases A and B. The harmonic frequency was taken to be

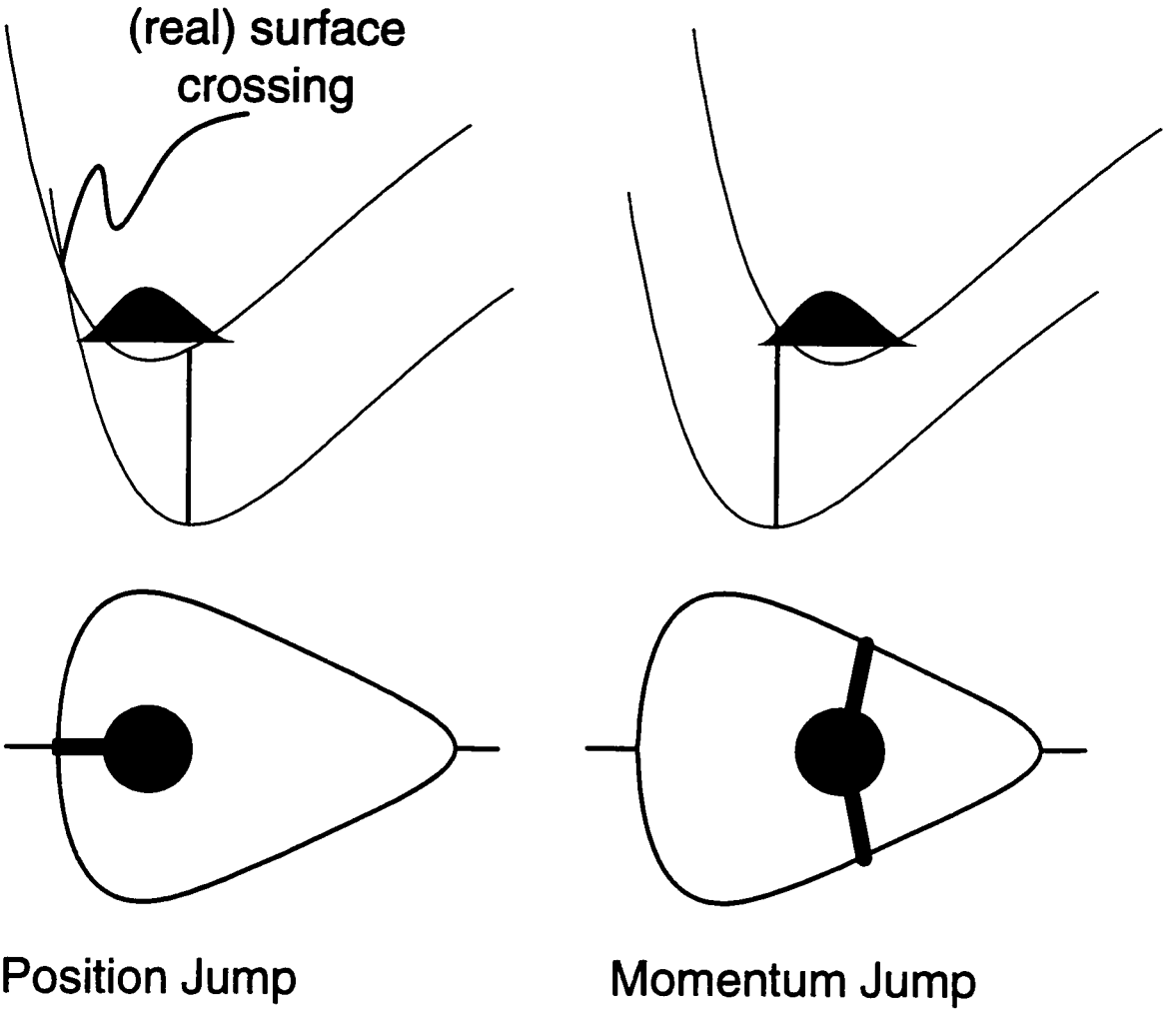

Figure 2.2: For cases A and B, we show schematic potential energy surfaces for the inward (A) and outward (B) displacements, and below each the corresponding phase space diagram. Case A corresponds to position jumping (or tunneling in position space) and case B, to momentum jumping. (A small component of position jump in case B can also be seen). Note the real crossing of the potential energy surfaces in case A.

$\omega = \sqrt{2Da} = \sqrt{2}$, and the displacement was also 0.1. The sign of the displacement does not matter for the harmonic case; both lead to position jumping (in opposite directions) and both give the same Franck-Condon factors. Note that the decline of the logarithm of the Franck-Condon factor in all three cases is approximately linear, which corroborates an exponential energy gap law. Case B (momentum tunneling) Franck-Condon factors decay much faster with energy than case A, and the harmonic potential gives the fastest decline. Note also the slightly concave shape of the case A Franck-Condon factor plot, whereas the harmonic case C is convex. (The concave shape is not a universal feature or Morse potential Franck-Condon factors). This has important consequences for the sharing of energy in multimode transitions (see section 3) .

Another case of momentum tunneling is shown in Figure 2.4. The domains of destructive interference between the two contributing stationary phase momenta are seen as dips in the Franck-Condon factors as a function of the final energy.

There are many more situations in one dimension which could be tested, including various changes in shape of the two potential energy surfaces. However, other such single mode Franck-Condon factors are also qualitatively predicted by simple phase space pictures of the type considered above. Nearly quantitative results can be obtained by detailed semiclassical analysis, but simpler methods are needed for convenient predictions, given the shapes of the surfaces.

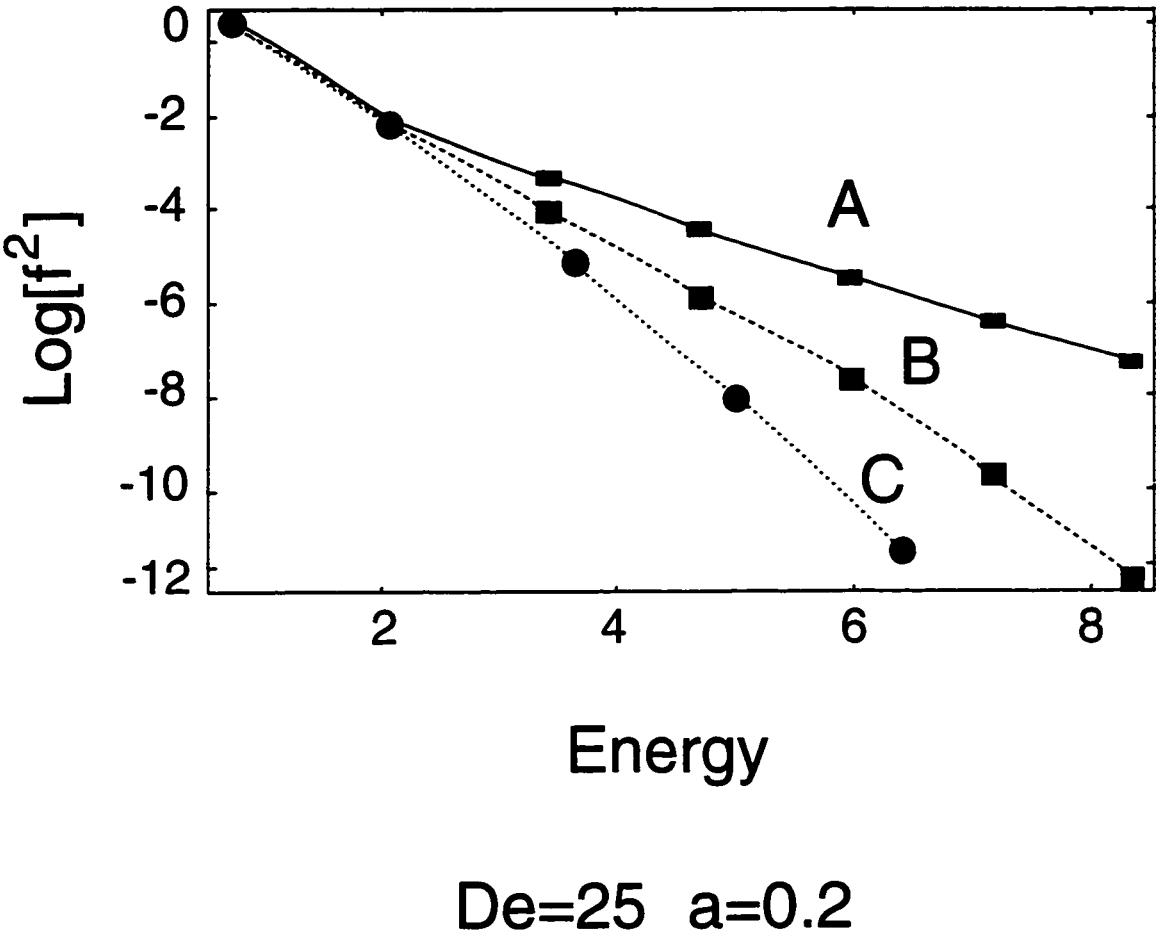

Figure 2.3: The base 10 logarithm of the Franck-Condon factors for the two Morse oscillator cases, A and B, and the matched frequency harmonic oscillator case C are shown. Note the much more rapid decline of the Franck-Condon factors for case B as a function of energy, and the concave shape of the case A curve. Case C is for two harmonic potential energy surfaces of matched curvature to the Morse oscillators at the minimum of the potential. Using the same displacement then gives a meaningful comparison with the Morse oscillator. Note that case C has the highest fall off and is *convex*.

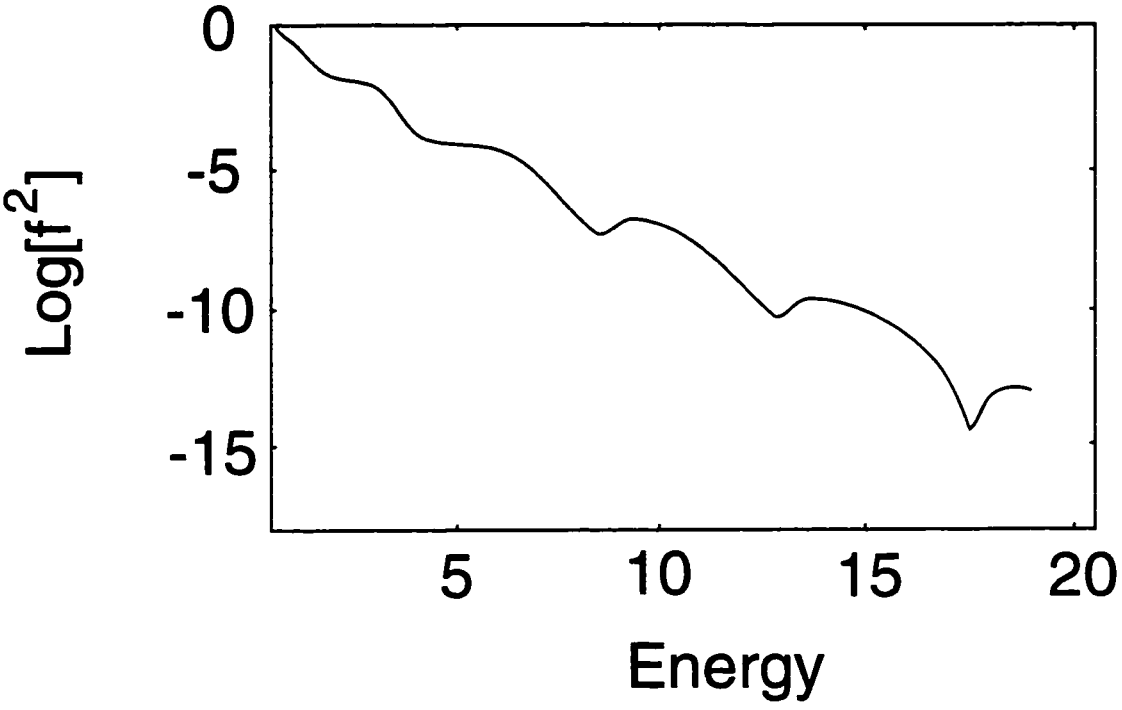

Figure 2.4: For a momentum jump case with $D_A = D_D = 20$, $a_A = 0.2, a_D = 0.26$, $b_D - b_A = 0.2$, the dips can be seen which result from interference between the $\pm p^{\dagger}$ stationary phase contributions.

2.4 Pulsed Transient Wave Packet

Another useful point of view is based on the possibility of a pulsed laser (typically of 50 femtoseconds to a few picoseconds in duration) preparation of a nonstationary wave packet on the acceptor potential energy surface. The idea is not to create the "whole" wave packet on the excited potential energy surface with an ultrashort laser pulse whose FWHM covers the whole of the energy envelope of the Franck-Condon wave packet $|\phi\rangle$. Rather we want to create a "nonclassical" wave packet by tuning the laser frequency off center (typically to the blue) of the absorption band and adjusting the pulse duration so that an appropriate band of states is excited. The population in each of the eigenstates will then be governed by two factors: the Franck-Condon factor and the energy density of the pulse at that frequency, which is controlled by the pulse duration and center frequency. There is an associated transient wave packet which we may define as (from first order time dependent perturbation theory)

$$|\phi_{\omega_0,\sigma}\rangle = \sum_n e^{-(E_n-\hbar\omega_0)^2/(2\sigma^2)}|n\rangle\langle n|\phi\rangle \tag{2.8}$$

Clearly, $|\phi_{\omega_0,\sigma}\rangle$ is a nonstationary wave packet which can be prepared rather easily in the laboratory. The experimentalist has control of ω_0 and σ, but the Franck-Condon factors are fixed. What is the nature of $|\phi_{\omega_0,\sigma}\rangle$? That is, is it a more or less localized state, and if so, what modes, or better, what part of phase space is populated?

Again, this question gets all the more interesting in two and more dimensions, but

the position *versus* momentum competition can readily be seen in one dimension. To this end we consider two cases, one clearly a momentum jump case and the other, a position jump. The two cases use the same acceptor Morse potential

$$V_A(x) = D_A(1 - \exp[-a_A(x - b_A)])^2$$

and a different donor potential

$$V_D(x) = D_D(1 - \exp[-a_D(x - b_D)])^2 \tag{2.9}$$

with $D_A = 20$, $a_A = 0.2$. The momentum jump case uses $D_D = 25$, $a_D = 0.22$, $b_D - b_A = \delta x = 0.3$, which is a stiffer potential energy surface displaced outward, and the position jump uses $D_D = 20$, $a_D = 0.2$, $\delta x = -0.3$, which is the same shape potential energy surface displaced inward. The Franck-Condon amplitudes are computed analytically [12]:

$$\langle n_A|0_D\rangle = (-1)^n \left(\mathrm{F}\ n!(1 - n/s)\frac{\Gamma[2s+1]}{\Gamma[2s+1-n]} \right)^{1/2} \tag{2.10}$$

$$\frac{\Gamma[2s+u-n]}{\Gamma[2s+u](1+z)^n}\ \mathrm{J}[n, u-1, 2s-2n, 1+2z] \tag{2.11}$$

Where $\mathrm{J}[n, \alpha, \beta, z]$ is the usual Jacobi polynomial, and

$$\begin{aligned} u &= (s + 1/2)\frac{\delta\omega}{\omega_A} \\ z &= \frac{2}{[1 + (1 + \frac{\delta\omega}{\omega_A}\exp[a_A\delta x])]} - 1 \\ \mathrm{F} &= \frac{\Gamma[2s+u]^2}{\Gamma[2s+2u]\Gamma[2s]}(1-z)^{2s+2u}(1+z)^{2s} \end{aligned}$$

$$
\begin{aligned}
s &= \frac{2D_A}{\omega_A} - \frac{1}{2} \\
\omega_i &= \sqrt{\frac{2D_i}{\mu}}\, a_i \\
\delta\omega &= \omega_D - \omega_A \\
\delta x &= b_D - b_A
\end{aligned}
$$

The energy eigenvalues of the Morse potential can be written ($\hbar = 1$):

$$E[n, D_i, a_i] = (n + 1/2)\omega_i - \frac{a_i^2}{2\mu}(n + 1/2)^2 \tag{2.12}$$

with the eigenfunctions

$$\psi_n(x) = \eta_n w^{\alpha/2-n} e^{-w/2} \mathrm{L}_n^{\alpha-2n}(w) \tag{2.13}$$

where

$$
\begin{aligned}
\eta_n &= \sqrt{\frac{a_i(\alpha - 2n)n!}{\Gamma[2k - n]}} \\
\alpha &= 2k - 1 \\
k &= \sqrt{2D_i}/a_i \\
w &= 2k \exp[-a_i x]
\end{aligned}
$$

In Fig. 2.5 plots of the donor and accepter Morse potentials are shown, together with the ground state $|\phi\rangle$ of the donor. The states $|\phi_{\omega_0,\sigma}\rangle$ are shown below the wave

function plots in the two cases. The position jump case is shown at the top; the momentum jump looks very similar. The states $|\phi\rangle$ differ very little. Yet the states $|\phi_{\omega_0,\sigma}\rangle$ differ substantially. Both were obtained from Eq. 2.8 with $\hbar\omega_0 = 12, \sigma = 2$. The position jump, obtained by a slight inward displacement of the donor potential energy surface, gives a $|\phi_{\omega_0,\sigma}\rangle$ showing a substantial tendency toward the inward displacement, while the momentum jump case shows a definite propensity to be large in the Franck-Condon region with oscillations. This is consistent with the labels "position jump" and "momentum jump".

The zero order states satisfy the condition

$$\sqrt{\frac{\hbar}{2\pi\sigma^2}} \int d\omega_0 |\phi_{\omega_0,\sigma}\rangle = |\phi\rangle \tag{2.14}$$

i.e., the state $|\phi_{\omega_0,\sigma}\rangle$ is a piece of the whole wave packet $|\phi\rangle$ in the above sense.

2.5 Wigner phase space analysis

We have just seen that position shifts and momentum shifts can compete for the major contribution to the Franck-Condon integral in the nonclassical regime. In several dimensions, each position and each momentum for each coordinate become contestants. The winning coordinate or momentum shift can be quite unexpected, and can change systematically as the energy is scanned through the nonclassical region. The result is that the propensity rules mentioned above can be very misleading. For

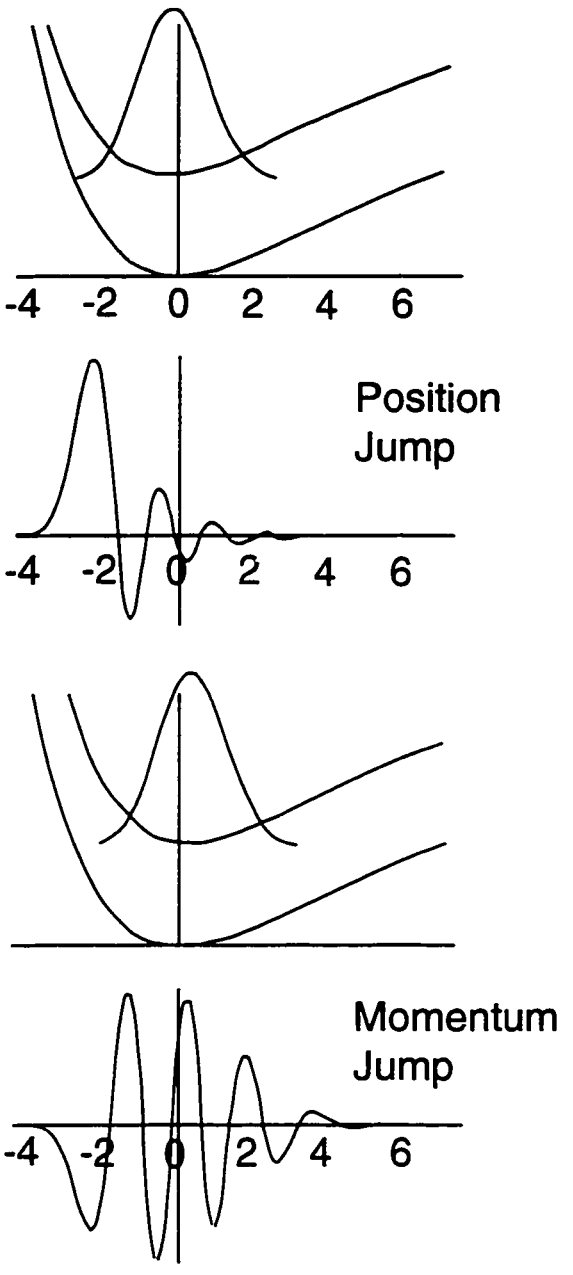

Figure 2.5: Position versus momentum jump for two lightly varying Morse oscillators. The top shows a position jump scenario as is evidenced by the pulsed state produced. The bottom scenario on the other hand shows a momentum jump as is seen by the numerous oscillations in the pulsed state produced.

example, the mode with the largest equilibrium position displacement need not be excited in a nonclassical Franck-Condon transition.

Some examples of this kind are well known. For example, radiationless transitions in aromatic hydrocarbons can be dominated by the carbon-hydrogen stretching motion even though the carbon-carbon backbone is much more displaced. The two Born-Oppenheimer potential energy surfaces involved, typically the ground singlet (S_0) or triplet (T_1) state and the excited (S_1A) state, are "nested" one inside the other, with no nearby crossing, certainly not one in the classically allowed region of the initial vibrational state on S_1. Therefore, the Franck-Condon factors are nonclassical. The C-H stretching is the acknowledged "accepting" mode for the conversion of electronic energy into excess vibrational energy. This is initially surprising in that it is the C-C bonds that are much more distorted. The replacement of hydrogen by deuterium can reduce radiationless rates by partially quenching the advantage the C-H bonds have in accepting the energy. This effect has been shown in studies of the magnitude of the Franck-Condon factors, but we shall gain additional insight with a fresh approach to the problem, and we will see this effect to be part of a much larger story involving anomalous nonclassical Franck-Condon factors.

Related phenomena include the exponential energy gap law of radiationless transitions [3] and the exponential momentum gap law of Ewing [4] for vibrational predissociation (where a high frequency vibrational mode plays the role of the electronic

state, relative to a low frequency Van der Waals mode). In these studies, considerable effort has been devoted to developing new intuition for nonclassical Franck-Condon factors. The emphasis has been on the mode competition problem, and the overall dependence of rates on the energy or quantum number gaps. Our emphasis is instead directly on the features of the potential energy surfaces which control the Franck-Condon factors, which in turn control the rates. Moreover, we go beyond the concept of accepting modes to one of accepting zones (in phase space), because these are more general.

The simple phase space pictures previously discussed, although useful as a guide for intuitive purposes, are obviously insufficient for multidimensional analysis. Here we present a method which quantifies the simple phase space pictures by evaluating the densities they represent. In one dimension, this will give an estimate of a Franck-Condon factor. The goal changes in several dimensions. First, we recall that our objective is to understand the *initial appearance* of amplitude on the acceptor potential energy surface. Calculating a multidimensional Franck-Condon factor requires detailed knowledge of the dynamics on the acceptor potential energy surface. Indeed, *getting* this knowledge out of a spectrum requires understanding the nature of the wave function initially prepared, so to speak, on the acceptor potential energy surface, which leads us back to our objective. The donor wave function on the other hand often lies near the minimum of its potential and it is not too much to expect to

know something about it.

In accord with these objectives, we will focus on the rate of radiationless relaxation (or local magnitude of the photoabsorption cross section in the optical case), by averaging over a narrow range of quasidegenerate states in a way familiar from the Golden Rule. This eliminates the need to calculate individual Franck-Condon factors. But more significantly, we will be able to analyze the rate expression, which is an integral over all phase space, in terms of the *regions* of phase space which contribute most. In the classic cases of C-H bonds playing the role of accepting modes, for example, regions in phase space corresponding to excited C-H motion will have the biggest contribution (which we will show for the case of benzene radiationless decay). In addition, we can go beyond that to say whether the C-H bonds are produced with a position or momentum jump, and whether one C-H bond or many (if there are many) will accept the amplitude from the donor. We are building the concept of accepting zones in phase space. All this will be possible with knowledge of the donor wave function and the shape of the acceptor potential energy surface, and without calculating any Franck-Condon factors. (Even the shape of the acceptor potential energy surface is a great deal to ask; fortunately, the analysis can also help to determine that as well, from experimental data.)

A very similar method for the total rates was used in our earlier paper where we were concerned with corrections to the reflection approximation [1]. That pa-

per was not especially concerned with the nonclassical region, although the limited investigation of it gave promising results.

An average over a "small" range of energy is necessary to smooth over possible structure in the spectrum, or to give the average squared matrix element in the Golden Rule formula,

$$\text{rate} = \frac{2\pi}{\hbar} < V^2 > \rho(E) \tag{2.15}$$

where $\rho(E)$ is the density of states. In radiationless transitions and photoabsorption-photoemission there can be structure on many scales in the spectra, so the issue of how large an energy average is required is problematical. Our working formula, derived below, depends on a short time approximation, and it will be ignorant of the recurrences in the time domain which give rise to the frequency domain structure. Such recurrences are, after all, events which happen after the initial preparation on the accepting potential energy surface, so to keep the concept of an accepting zone, where the amplitude first arrives in phase space valid, we must average over a large enough energy interval to remove such structure.

For the optical case, the absorption/emission spectrum is given (apart from some constants and a trivial frequency dependence) by the Fourier transform of the correlation function $\langle\phi|\phi(t)\rangle$:

$$\Sigma(\omega) = \frac{1}{2\pi}\int_{-\infty}^{\infty} e^{iE\tau}\langle\phi|\phi(\tau)\rangle d\tau. \tag{2.16}$$

Here we have defined $\phi = \mu_{fi}|\chi_i\rangle$, where χ_i is the initial vibrational wave function

and μ_{fi} is the transition moment (which often is nearly constant over the domain of χ_i).

Both the photoabsorption/emission cross section and the rate of radiationless decay (Formula 2.15) can be written as (apart from some constants)

$$\text{rate} \propto \Sigma(\omega) = \text{Tr}[\delta(E - H)\rho_\phi], \tag{2.17}$$

where Tr is the quantum trace operation, H is the full quantum Hamiltonian for the acceptor electronic state, and $\rho_\phi = \mu_{fi}|\chi_i\rangle\langle\chi_i|\mu_{fi} \equiv |\phi\rangle\langle\phi|$. Formula 2.17 serves as our basis for the phase space analysis of nonclassical Franck-Condon factors.

We wish to transform equation 2.17 to an equivalent Wigner phase space form, in powers of $\hbar$. The lowest order term in the expansion will provide us with our tool to study position vs. momentum hops. The method shown here parallels that discussed in Ref. [1], and is illustrated here for completeness.

The Wigner transform of an operator or density matrix A is defined as (for N dimensions)

$$A_W(q,p) = \left(\frac{1}{\pi\hbar}\right)^N \int_{-\infty}^{\infty} ds\ e^{2ips/\hbar}\langle q - s|a|q + s\rangle. \tag{2.18}$$

The useful property

$$\text{Tr}(AB) = (2\pi\hbar)^N \int dpdq\ A_W(p,q)B_W(p,q) \tag{2.19}$$

relates the quantum trace to the classical phase space trace over the Wigner repre-

sentations of the operators. The right hand side of Equation 2.17 can thus be written

$$\mathrm{Tr}[\delta(E-H)\rho_\phi] = (2\pi\hbar)^N \int dpdq\ \delta(E-H)_W\ \rho_{\phi,W}. \tag{2.20}$$

Where $\rho_{\phi,W}$ is the phase space distribution which is the product of the transition dipole operator and the initial vibrational state. However, note that in general, $(AB)_W \neq A_W B_W$. The Wigner transform of the product of operators is given by (Ref. 22 in Ref. [1])

$$(AB)_W = A_W[e^{\hbar\Lambda/2i}]B_W \tag{2.21}$$

with

$$\Lambda = \sum_k \frac{\overleftarrow{\partial}}{\partial p_k}\frac{\overrightarrow{\partial}}{\partial q_k} - \frac{\overleftarrow{\partial}}{\partial q_k}\frac{\overrightarrow{\partial}}{\partial p_k},$$

where the arrows indicate the direction to take the derivatives. Next we need an expression for $\delta(E-H)_W$. Given that

$$\delta(E-H) = \frac{1}{2\pi\hbar}\int_{-\infty}^{\infty} e^{i(E-H)\tau/\hbar}d\tau,$$

straightforward algebra leads to the result (Ref. 2.16)

$$(2\pi\hbar)^N\delta(E-H)_W \simeq \delta(E-H_c) - \hbar^2\frac{\partial^2}{\partial E^2}\delta(E-H_c)f_1 + \hbar^2\frac{\partial^3}{\partial E^3}\delta(E-H_c)f_2. \tag{2.22}$$

where

$$f_1 = \sum_k V_{kk}/(8m_k) \tag{2.23}$$

$$f_2 = \sum_k (V_k)^2/(24m_k) + \sum_{kk'} P_k P_{k'}/(24m_k m_{k'}) \tag{2.24}$$

where $V_k \equiv \partial V/\partial q_k$.

Using the lowest order part of this we get for the total absorption to 0^{th} order in $\hbar$

$$\Sigma(\omega) = \int dpdq\delta[E - H_c(p,q)]\rho_{\phi,W}(p,q) \tag{2.25}$$

We can interpret $\delta[E - H_c(p,q)]\rho_{\phi,W}(p,q)$ as the phase space density of particles of total energy E corresponding to the state $|\phi\rangle = \mu_{fi}|\chi_i\rangle$. By analyzing the *integrand* of equation 2.25 we can determine the propensity of a state to make either a position or momentum hop during a Born-Oppenheimer electronic surface transition.

3

Two-mode competition: separable Morse oscillators

The method of section 2.5 is capable of handling nonseparable multimode potential energy surfaces. However, much can be learned by the consideration of separable modes. The additional element introduced by having more than one mode involved leads to interesting effects even for separable systems with identical mode structure on both potential energy surfaces.

Suppose we are interested in Franck-Condon factors involving the ground state of surface 1 with excited states of surface 2 in some energy range, ΔE. The system has several or many "choices" for arriving at the necessary energy from two (or more) modes. The number of choices is simply $\rho(E)\Delta E$, where $\rho(E)$ is the density of

states. However, in general, these choices will differ drastically in their Franck-Condon overlap with the initial state, even though they fall in the same narrow energy range.

We focus attention on one issue out of many which should be addressed. Consider two identical, separable Morse oscillators. They may represent two equivalent C-H bond stretches in the same molecule, for example. Both the donor and the acceptor potential energy surface are Morse potentials but the equilibrium positions, well depths, and effective force constants will vary between the donor and acceptor states. Even in this simplified donor $\rightarrow$ acceptor transition, several interesting scenarios are possible:

- Either position jumps or momentum jumps can be dominant.
- The C-H bonds may share the energy in the acceptor nonclassical wave packet equally, or one may be excited much more than the other.
- The two previous items, each with two extremes, combine to make four scenarios.

In what follows we shall see two of the four scenarios arise with slight adjustments of the *donor* potential only; the acceptor potential will remain the same. (Indeed it is only the differences in the two potentials that matter). We will examine the cases with two tools: first, we create the nonclassical Franck-Condon wave packet for a given (blue) band center detuning (or equivalently the energy gap, or red detuning

in emission) and transform limited pulse bandwidth. By inspecting the location and nodal structure of the nonclassical pulsed wave packets, the various possibilities for position and momentum jumps become apparent. Second, we plot the phase space density of the function

$$\delta[E_0 - H_a(\vec{p},\vec{q})]\,\rho_d(\vec{p},\vec{q}) \tag{3.1}$$

where $\delta[E - H_a(\vec{p},\vec{q})]$ is the energy hypersurface ("energy contour") of the accepting Born-Oppenheimer Hamiltonian, and $\rho_d(\vec{p},\vec{q})$ is the Wigner density of the donor wave function. The Wigner method is fast and applicable to several nonseparable degrees of freedom, making it possible to explore the effects of small changes in the potential energy surfaces rather easily.

The parameters for the two cases are as follows. Both have the acceptor potential energy surface

$$V_a(x,y) = D_a[1 - \exp(-\lambda_a x)]^2 + D_a[1 - \exp(-\lambda_a y)]^2 \tag{3.2}$$

with $D_a = 20.$, $\lambda_a = 0.2$. The kinetic energy is simply

$$T = \frac{1}{2}(p_x^2 + p_y^2) \tag{3.3}$$

The two donor potential energy surfaces are of the form

$$V_d(x,y) = D_d[1 - \exp(-\lambda_d(x - x_0))]^2 + D_d[1 - \exp(-\lambda_d(y - y_0))]^2 \tag{3.4}$$

The parameters for the two examples are:

Case	D_d	λ_d	$x_0 = y_0$	E_0	σ
1 (momentum jump, unshared)	28	0.20	0.55	16	2.24
2 (position jump, shared)	17	0.25	-0.5	16	1.73

The examples nicely illustrate the competition for the role of accepting mode or, more properly, accepting coordinate. The donor potential in the first example is tighter and has its equilibrium shifted to larger distance, as compared to the accepting potential.

Both differences tend to favor momentum jumps. The donor potential in the second example is looser and has its equilibrium shifted to smaller distance, as compared to the accepting potential. In this case, both differences tend to favor position jumps.

These trends are exactly what is seen in Fig. 3.1 and Fig. 3.2. Both figures show the accepting potential contours, with the contour for $E = 16$ darkened; this is the average final energy on the acceptor potential energy surface. This is the center energy E_0 of the Gaussian energy envelope, Eq. 2.8. It is also the energy E_0 of the classical energy surface (see Eq. 3.1) on which the Wigner density of the donor wave function is evaluated.

The phase space density of the Wigner function $\rho_d(\vec{p}, \vec{q})$ is plotted as a series of line segments representing the momentum distribution at selected positions. The direction of a line segment shows the direction of the momentum, and its length is proportional to the magnitude of ρ_d as a function of momentum for the given position,

not the momentum itself.

In case 1, Fig. 3.1, note that the wave packet and the phase space distribution agree on the predominantly *independent* bond momentum jump in this case (the wave packet is a linear combination of two symmetrically related wave packets, each with energy mostly in one bond). Further, the energy is stored mostly as momentum, as seen from the nodal structure of the wave packet and the fact that the wave packet is very small near the classical contour $V(x, y) = E_0$.

In case 2, Fig. 3.2, the wave packet and the phase space distribution agree on the *correlated* bond position jump (the wave packet has both bonds sharing the energy simultaneously). The energy is stored mostly as potential energy, as seen from the fact that the wave packet is very near the classical contour $V(x, y) = E_0$.

The wave packet has energy uncertainty, given by the energy width of the envelope used. There is a reciprocal time uncertainty implied; one effect of this is that the pulse prepared wave packet has some amplitude and nodes leading away from the region in phase space where the amplitude is largest, according to the Wigner phase space density.

The pulsed prepared wave packets and the Wigner phase space density agree remarkably well. This raises the hope that predictions of the acceptor coordinates in general circumstances will be quite feasible. The wave packet is quite sensitive to the relative shape of the potentials. This should ultimately be a blessing.

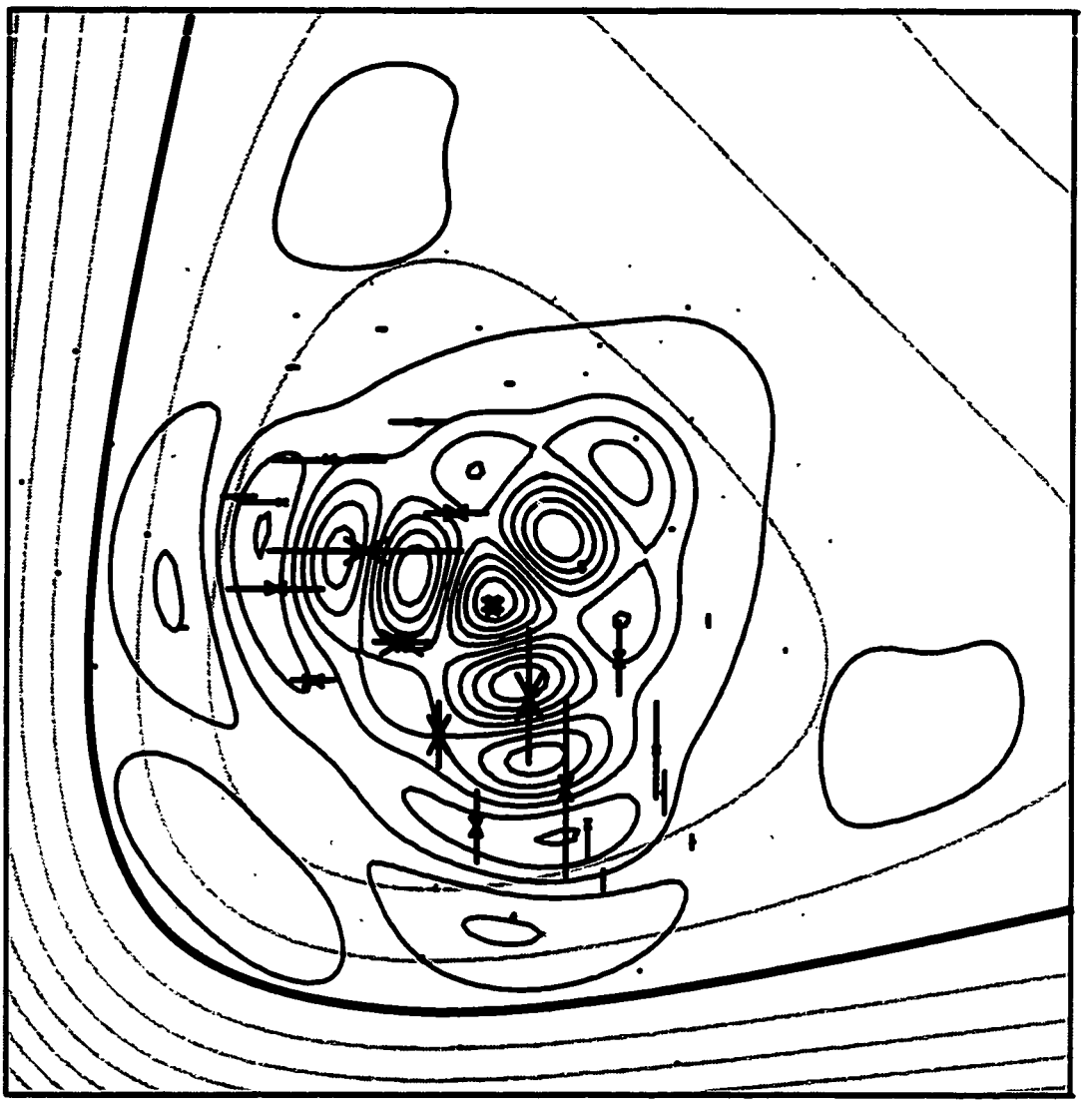

Figure 3.1: The acceptor potential energy surface contours (E=16 darkened) together with the pulse excited wave packet and the phase space density of the Wigner function of the donor ground state, ρ_d at E=16. The latter is plotted as a phase space distribution, as a series of line segments representing the momentum distribution at selected positions. The direction of a line segment shows the direction of the momentum, and its length is proportional to the magnitude of ρ_d as a function of momentum for the given position, not the momentum itself. Note that the wave packet and the phase space distribution agree on the predominantly independent bond momentum jump in this case (the wave packet is a linear combination of two symmetrically related wave packets, each with energy mostly in one bond.

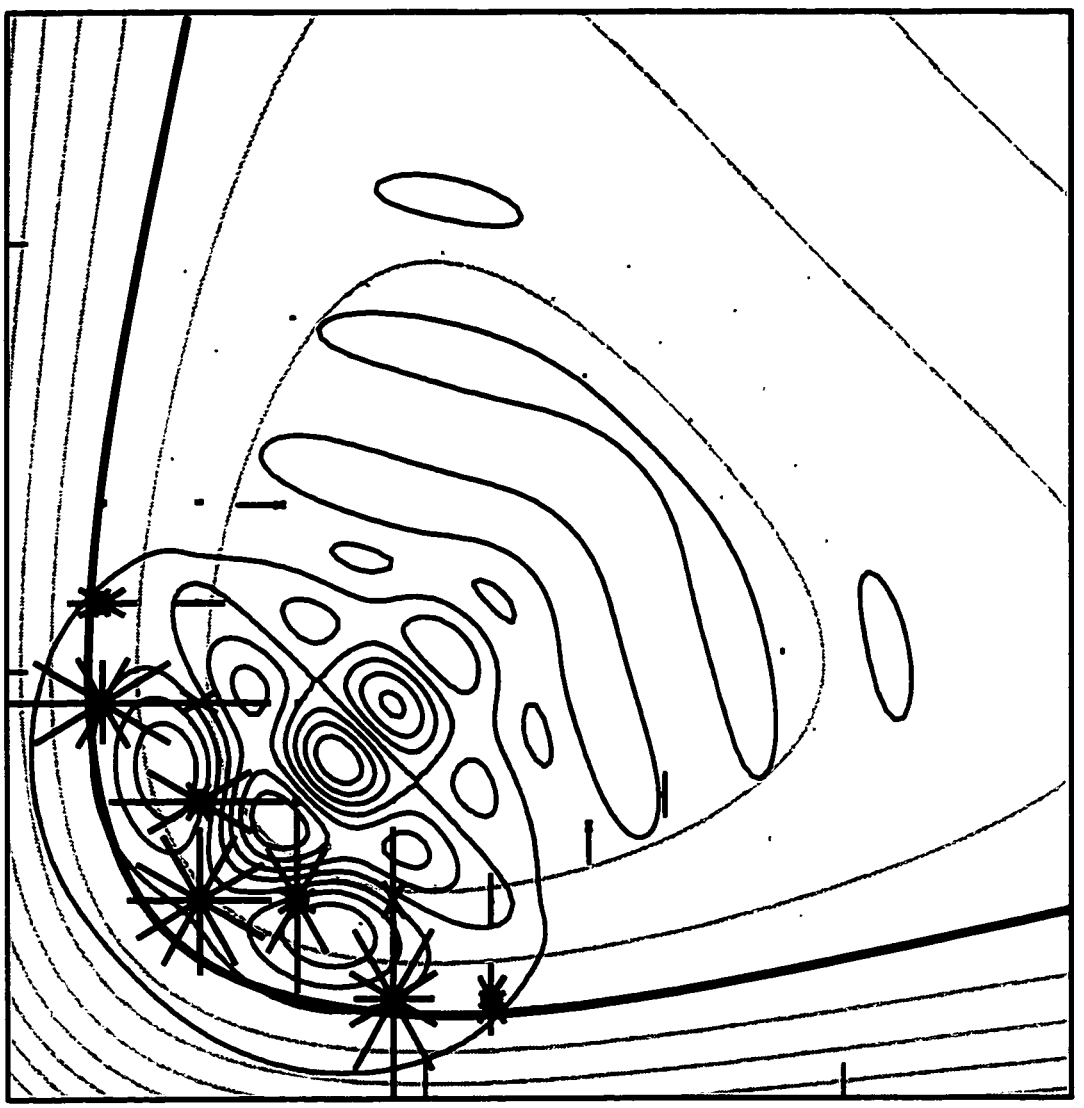

Figure 3.2: Same as Fig. for case 2. The wave packet and the phase space distribution agree on the correlated bond position jump (the wave packet has both bonds sharing the energy simultaneously).

Our simple results have already revealed a case where the electronic energy shows up primarily in one of two nominally equivalent bond modes (case 1) , and another case where the energy is shared equally (case 2). One case (case 1) was primarily a momentum jump, and the other, case 2, a position jump.

Direct or indirect experiments depend critically on the nature of the nonclassical wave packet. In direct measurements, the effects of putting energy into very specific modes (and indeed with specific initial momenta or positions) can have a dramatic effect; e.g. the breaking of a specific bond. In a pulsed laser experiment, the accepting modes can dramatically change, as the energy gap is increased by tuning the center frequency to the blue. Pump-probe [13, 14, 15] experiments would be ideal. By exciting just a part of the blue wing of an absorption band, the nonclassical Franck-Condon wave packet is literally produced in real time, and its potentially bizarre character will appear as changes in the probe transitions with time and detuning.

4

Phase Space Analysis of Benzene Radiationless Decay

4.1 Historical orientation

As previously mentioned, we apply our phase space model to the problem of benzene radiationless decay. After excitation to the S_1 excited state and at pressures < 0.1 Torr, benzene radiationlessly decays. This is manifested via the exponential decay of the fluorescence emission intensity versus time (with a lifetime of $\approx$ 70 ns) and a quantum yield of $\phi_F \approx 0.2$: the low pressure minimizes collisional deactivation for the decay time observed. Therefore, given the decay time and the low pressure, four out of five molecules decay radiationlessly and *intramolecularly.*

Much effort has been applied to the problem of benzene's radiationless decay [3]. There are two mechanisms or pathways for this decay: the energy may decay to the T_1 excited state (intersystem crossing), or it may decay to the S_0 electronic state (internal conversion). In the first case, the primary coupling is a spin-orbit term and in the second case the nonadiabatic terms from the Born-Oppenheimer approximation provide the link.

In our study, we focus on the second case (internal conversion). Our main goal is to test our technique on a well studied molecule and see if we can reproduce results previously obtained. In addition, we go beyond the traditional mode competition analysis and provide a phase space interpretation.

4.2 Issues

We choose, among many, three issues to address. The first issue deals with the best accepting modes for the excess electronic energy. It is well known that the C-H stretching modes provide the most efficient pathway for radiationless decay when the energy separation of the donor and acceptor state is large relative to the coupling; why is this the case? The answer to this question is perhaps best answered by a simple illustration, as shown in Fig. 4.1. The figure is comprised of two separable, two dimensional, harmonic electronic surfaces serving as the donor and acceptor states, where two possible scenarios are depicted. In the first scenario, most of the excess

energy is deposited into the high frequency mode, with the balance deposited into the low frequency mode. The other scenario is the reverse of the first. Given that the Franck-Condon factor is the product of the two separate one dimensional overlaps, it is clear that the first scenario provides the greatest overall product for the two possibilities.

The second issue concerns the possible localization of energy into the separate *local* C-H stretching modes. In chapter 3 we showed a momentum jump scenario where the energy was not shared evenly in both modes. Although not discussed earlier, an equivalent harmonic oscillator model gave entirely different results: the energy was shared rather than localized. In benzene, there are six degenerate local C-H stretch modes. Overtone spectroscopy experiments have shown progressions whose frequencies almost identically match those of a diatomic C-H radical molecule [19]. Thus, given a properly constructed model, we may reasonably expect to see such localization in the proper regions of phase space, for these local C-H stretches. Conversely, since we only show results for a harmonic model, as discussed later, we may not see evidence of such localization, which we will discuss in our results.

The third and final issue we address focuses on the deuterium isotope effect. It has been noticed that complete deuteration of benzene enhances the fluorescence quantum yield, thus reducing the effectiveness of the radiationless pathway. This is easily explained once we realize that the high C-H stretching mode frequencies are

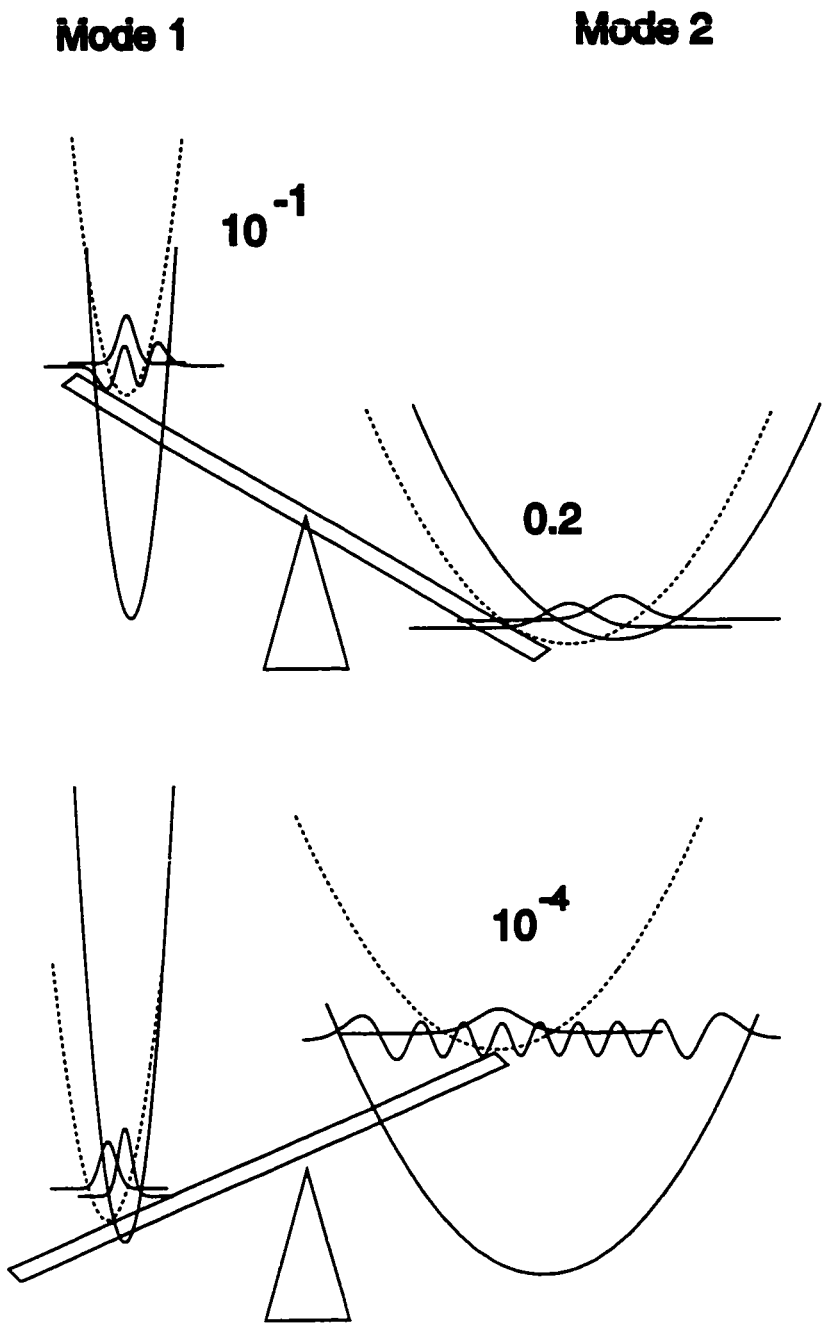

Figure 4.1: The two dimensional energy mode competition for separable harmonic oscillators. Two scenarios are illustrated. As seen, the scenario depicting most of the energy residing in the higher frequency mode results in the largest overall Franck-Condon factor, which is a product of the two one dimensional overlaps.

reduced by a factor of $\approx \sqrt{2}$, as shown in tables 4.1 and 4.2. Consequently, the effectiveness of the C-H stretching modes as energy absorbers is reduced relative to the C-C stretching modes. This effect is apparent in our model, as will be shown subsequently.

Table 4.1: Vibrational frequencies (cm^{-1}) of C_6H_6 for the $^1A_{1g}$ and $^1B_{2u}$ states.

	$^1A_{1g}$		$^1B_{2u}$	
Symmetry	Calculated	Kato(88)	Calculated	Kato(88)
a_{1g}	3081	3082	3123	3127
	969	969	862	862
a_{2g}	1351	1350	1289	1290
b_{1u}	3038	3041	3099	3100
	1011	1010	937	936
b_{2u}	1307	1308	1581	1575
	1145	1144	1100	1104
e_{1u}	1489	1492	1399	1410
	1032	1032	932	928
	3074	3068	3118	3117
e_{2g}	3055	3059	3101	3103
	602	601	507	507
	1163	1163	1103	1104
	1621	1622	1508	1507

4.3 Model

For our starting point, we choose to model benzene using a normal mode coordinate system, although, we are not constrained to this by our method of analysis. Given that benzene is a 12 atom molecule, we have 30 internal degrees of freedom to work with; however, we may simplify this by constraining ourselves to only the planar vibrations. Restricting ourselves in this way is not unreasonable, since both the S_1 and the S_0 states share the same D_{6h} symmetry, i.e. the equilibrium configuration is planar in both states. Thus, since the out of plane modes are not initially excited and, given there low frequency, they will not contribute significantly to the mode competition. Although this model is definitely simplistic, it serves to present some important issues regarding our method of analysis.

In addition to the normal mode assumption, we also choose the ground vibrational state of the S_1 electronic surface for our initial state. We employ the force field provided by Kato [16] and calculate the normal frequencies and coordinates necessary for our surfaces. The results for both benzene and deuterated benzene are compiled in Tables 4.1 and 4.2.

Table 4.2: Vibrational frequencies (cm^{-1}) of C_6D_6 for the $^1A_{1g}$ and $^1B_{2u}$ states.

	$^1A_{1g}$	$^1B_{2u}$
Symmetry	Calculated	Calculated
a_{1g}	2295	2319
	922	823
a_{2g}	1051	1002
b_{1u}	2248	2291
	968	898
b_{2u}	1300	1579
	816	781
e_{1u}	2292	2311
	1330	1216
	807	753
e_{2g}	2268	2293
	1573	1459
	850	807
	575	486

4.4 Method of Analysis

Before we discuss our results, a description of the method of analysis of equation 2.25 is in order. Recall that our objective is to determine which zone of phase space gives the greatest contribution to the integrand of equation 2.25. The planar normal coordinates are comprised of twenty one degrees of freedom, which in turn gives us a 42 dimensional phase space integrand. Thus, our problem is one of maximizing a 42 dimensional phase space Wigner function subject to the constraint that $E = E_0 = 1/2 \sum_{j=1}^{N} (\dot{Q}_j^{\,2} + \lambda_j Q_j^2)$, where the Q's are the normal coordinates for the acceptor state and the λ's are the squares of the frequencies. We employ a simulated annealing technique to achieve this. Assuming that our function is relatively localized, this maximum informs us as to which modes are the best accepting modes and how the energy is distributed among these modes. Our previous results showed promise that this assumption is not unreasonable. However, there may be cases where this assumption may breakdown, as will be shown later.

Our next step is to compare this optimum distribution with the possibilities where each normal mode (or local mode) accepts most of the energy separately. This is achieved by optimizing the Wigner distribution subject to the constraint that all the energy be deposited in one mode only. Thus, this is essentially a 1-D optimization problem where we determine whether a position jump or a momentum jump is the most favorable mechanism. The result of this analysis is then represented as a plot

of the frequency of each mode versus the optimized Wigner amplitude of that mode.

5

Results and Conclusions

In our model, the S_1 electronic surface minimum is displaced relative to the S_0 minimum. Of the 21 normal modes, only the 2 a_{1g} coordinates are displaced. The C–C a_{1g} displacement is the largest, with a value of 0.406 A, and C–H a_{1g} displacement is -0.0139 A.

From the Franck-Condon principle, we might expect the C–C a_{1g} mode to provide the best accepting mode for the electronic transition. For a radiative transition, this is indeed the case, and is supported by our results as shown in the Wigner magnitude plot in Fig. 5.1 (bottom) for C_6H_6. The largest peak corresponds to the C–C a_{1g} symmetric stretch mode (at 969 cm^{-1}), which is the most displaced, as noted earlier. In addition, the maximum for the Wigner function is displaced mostly along the C–C a_{1g} coordinate such that 60.8% of the energy resides in that mode. Furthermore, all

the energy is manifested as potential energy: the mechanism for the transition is a position hop. The energy at which the Wigner function was analyzed corresponds to a "0-0" transition, in our model.

For a radiationless decay, the Franck-Condon picture is no longer valid, since the higher frequency modes are now the best acceptors as shown in Fig. 5.3 bottom. The largest peak is now the C–H a_{1g} symmetric stretch (at 3081 cm^{-1}). This time, we find the maximum displaced primarily along the C-H a_{1g} mode with 80.3% of the energy. Here the energy corresponds to the energy of the donor state (ground vibrational state on S_1 surface) as measured from the S_0 minimum. The fact that displacements dominate at lower energy separations and "distortions" (frequencies) at higher energy, was noted by Siebrand [17] many years ago. Thus, our simple model supports the conclusion that the highest frequency modes are the best acceptors at large energy separations.

In addition to the normal modes, we analyzed the Wigner function for the case where all the energy is deposited into a C–H local stretch mode, (the frequency of that mode closely matches one of the e_{2g} C–H normal modes. The magnitude of the function is of the same order of magnitude as the other high C–H stretches, but lies below that of the totally symmetric C–H stretch. Although the function is large in that region, the greatest contribution appears to arise from the region of the symmetric stretch, indicating a sharing of the energy among all the C–H local modes.

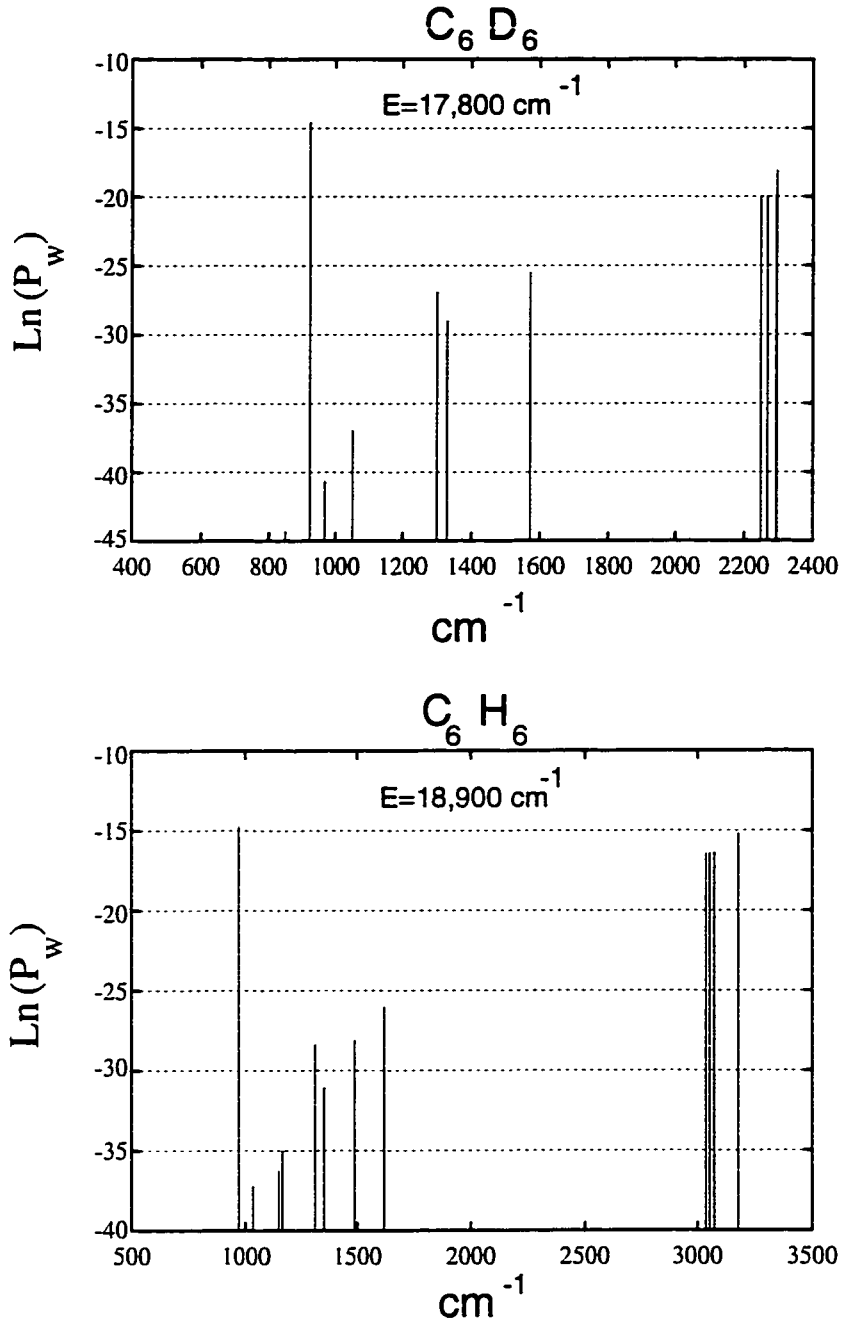

Figure 5.1: Plot of the maximum of $\ln(\rho_W)$ versus frequency of each normal mode for both C_6H_6 and C_6D_6. Each peak corresponds to the classical situation of putting all the vibrational energy into the respective normal mode, as designate by the frequency. The plot represents the "0-0" transition.

This is consistent with results found for simpler systems, as mentioned previously. At this point, we have only "sampled" various regions of phase space to build an idea of the energy distribution. Of course, this is not conclusive by any means, and more work to determine the extent of localization needs to be done.

We also check for the effect of deuteration on the mode competition. The results for three different energy gaps are indicated in figures 5.1, 5.2 and 5.3. As the energy gap is increased, the rate at which the higher frequency modes increase their accepting character relative to the lower frequency modes for C_6H_6 is greater than for C_6D_6. In addition, the ratio of the Wigner functions at maximum is $\approx$ 500 : 1, indicating an overall drop in the magnitude of the integrand and the transition rate for radiationless decay.

Our initial results for the phase space analysis of electronic transitions has shown good qualitative agreement with previous analyses. Qualitatively, our simple model is able to discern how energy is distributed in phase space and consequently among various competing modes. However, in our simple model we found a significant deviation from Franck-Condon overlap calculations in the case of deuterated benzene, as shown in table 5.1. For the comparison, we determine the distribution of quanta into the 21 modes which provides the largest transition probability. As shown, the agreement is quite good for benzene; deuterated benzene however, shows a marked deviation in that it predicts the C–C b_{2u} stretch mode as the best acceptor.

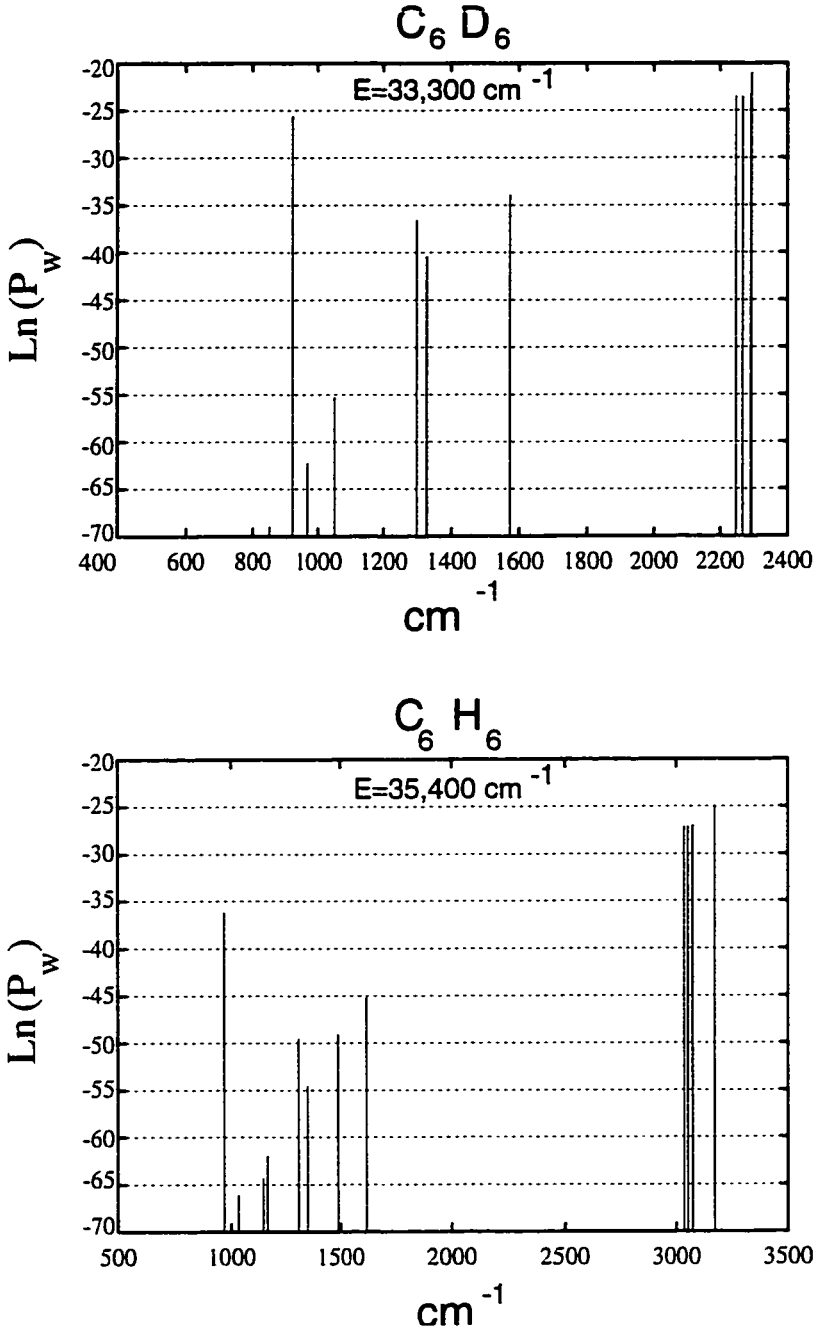

Figure 5.2: Same as 5.1 for the case of a transition to the designated energy. Along with the other plots, this shows how the competition ensues between modes as the energy gap is increased.

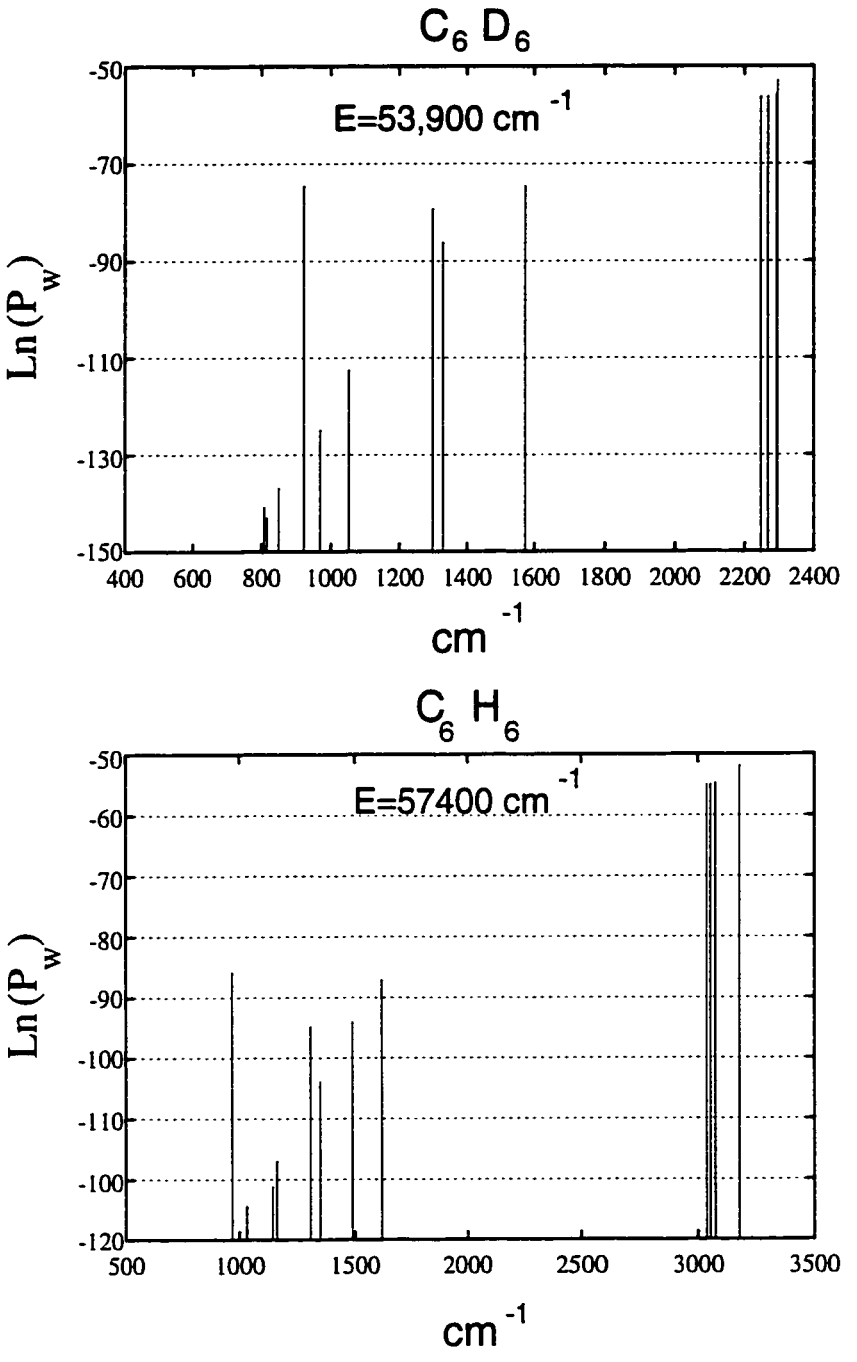

Figure 5.3: Same as 5.1 for the energy gap corresponding to a radiationless transition, for our model. Here, the higher frequency modes clearly dominate.

Table 5.1: Optimum Energy Distributions. Wigner classical energy versus Franck-Condon quantum number distributions.

	C_6H_6			C_6D_6		
		F.C.	Wigner	F.C.	Wigner	
			% Total			% Total
Symmetry	ω	n	Energy	ω	n	Energy
a_{1g}	3082	8	85.2	2295	4	70.7
	969	2	10.6	922	5	15.9
a_{2g}	1351	0	< 1	1051	0	< 1
b_{1u}	3038	0	< 1	2248	2	< 1
	1011	0	< 1	968	0	< 1
b_{2u}	1307	0	< 1	1300	8	< 1
	1145	0	< 1	816	0	< 1
e_{1u}	1489	0	< 1	1330	2	< 1
	1489	0	< 1	1330	0	< 1
	3074	0	1.4	2292	0	5.6
	3074	0	< 1	2292	2	6.3
	1032	0	< 1	807	0	< 1
	1032	0	< 1	807	0	< 1
e_{2g}	3055	2	1.5	2268	0	< 1
	3055	2	< 1	2268	0	< 1
	1621	0	< 1	1573	0	< 1
	1621	0	< 1	1573	2	< 1
	1163	0	< 1	850	0	< 1
	1163	0	< 1	850	0	< 1
	602	0	< 1	575	0	< 1
	602	0	< 1	575	0	< 1

There is another force at play here other than the simple competition between the high and low frequency modes. As stated previously, the overlap decreases exponentially with an increase in the difference of quanta in the respective modes. In addition, for parallel normal coordinates, the closer any two modes are in frequency, the faster the relative drop in the magnitude of the overlap. Note that for deuterated benzene, there is a greater relative difference of frequencies between the donor and acceptor states for the b_{2u} mode, as compared to the higher frequency C–H stretch modes. Consequently, the overlap of these two states decays significantly more slowly than the higher frequency C–H stretch modes, per increase in quanta, so as to outweigh the effect of putting more quanta into this mode (at least for the energy gap studied).

As previously mentioned, Stimulated Emission Pumping (SEP) experiments provide an ideal method for producing and studying the nature of the initial state during an electronic transition. Unlike a radiationless transition, SEP allows the experimentalist to control the energy gap. In SEP, one laser pulse is used to prepare a desired initial state (nanosecond duration), and a second pulse is used to stimulate emission to a desired final state or final energy regime. Consequently, by controlling the time dependent width of the pulse as well as the average frequency, the final energy and desired energy width is chosen. Thus, the nonstationary state shown as equation 2.8 is produced in real time.

Acetylene has been studied extensively both experimentally as well as theoretically. Experimentally, it is quite interesting since the equilibrium geometries of the ground $\tilde{X}$ state and the excited $\tilde{A}$ state have considerably different equilibrium geometries. The $\tilde{X}$ state is collinear and belongs to the point group $D_{\infty h}$ while the $\tilde{A}$ state is *trans bent* and belongs to the point group C_{2h}. Also, the C–C bond is 15% longer in the $\tilde{A}$ state than in the $\tilde{X}$.

Theoretically, given its relatively small size, acetylene has been of much interest to theorists. Consequently, there is a wealth of electronic structure data in existence from which to construct appropriate electronic surfaces. Since the $\tilde{X}$ state is collinear, it requires a total of 7 degrees of freedom to describe the internal dynamics. The $\tilde{A}$ state on the other hand, requires a total of six degrees of freedom to describe the internal dynamics. Thus, relatively speaking, acetylene is a more tractable molecule for theoretical descriptions.

We would like to study the preparation of the initial state in two separate regimes. The first regime corresponds to energies where the normal mode description is still applicable. This regime exists at energies as high as 9,000 cm^{-1} above the ground state. Again, we may probe phase space to determine the best accepting modes for the transition from the ground vibrational state on the $\tilde{A}$ surface to the acceptor vibrational states on the $\tilde{X}$ surface.

The other regime of interest exists in the region at around 27,000 cm^{-1} above the

$\tilde{X}$ state minimum. This region is known to be highly anharmonic. Also, experimental evidence suggests that the eigenstates in this regime are chaotic. Consequently, a description in terms of "modes" is no longer applicable. Thus, employing our more general phase space approach and probing the best *accepting zones* may be more appropriate for understanding the properties of the initial state prepared.

Induced Frequency Shifts of a Water Monomer Embedded in Helium Clusters

6

Introduction

Helium, as is commonly known, is a relatively inert substance with some extremely interesting properties, not the least of which is that it is a superfluid at extremely low temperatures: ^{4}He, a Bose particle, is a superfluid at temperatures below 2.19K, and ^{3}He, a fermi particle, is a superfluid at temperatures below 2.4mK. These properties are due to helium's small mass and weak interatomic potential: it becomes a quantum fluid before it has a chance to freeze [20]. As a result, helium has been the subject of an extensive body of research which continues to this day.

Historically, most research has concentrated on the superfluidity of bulk helium with the subsequent move into smaller systems. While it is known that bulk helium is a superfluid, the question of superfluidity in finite size helium clusters is still an open question; although, there is mounting evidence suggesting superfluidity [22,

23, 24]. If superfluidity does exist in finite systems, at what temperature does it become manifest? Modern experimental methods have increased our ability to probe small clusters and to gain insight into these systems and their interactions. Helium clusters of varying size are currently created using supersonic expansion experiments, which produce the clusters at extremely cold temperatures [21]. Once the clusters are formed they are, ideally, separated and their properties probed as a function of size [26, 27]. Probing and size selecting pure helium clusters is still a challenging practical endeavor and has prompted the development of indirect measures of helium cluster properties. Helium clusters are now known to have a large capture cross section, as demonstrated by Scheidemann et. al. [25], thus giving experimentalists a means to probe helium clusters in a nondestructive manner. The clusters are formed in a supersonic expansion and chromophoric impurities are embedded via a crossed molecular beam, or by passing the clusters through a chamber containing the impurity in the gas phase. Once the chromophores are within the clusters, they are probed spectroscopically and modifications to the spectrum provide insights into the helium-impurity interactions.

Our project is concerned with the effect that helium clusters have on the vibrational motion of an embedded water monomer, where these questions motivate our project:

- Are ^{4}He clusters superfluid?

- If ^{4}He clusters are superfluid, how will they affect the vibrational spectrum of the water monomer as compared to nonsuperfluid He?

Our project is part of an ongoing mission undertaken by many researchers who are addressing the first question. We add to the body of evidence by exploring how the clusters affect the monomer's vibrational spectrum at 0K. The method we employ, Diffusion Monte Carlo, which is elaborated on later in this thesis, is limited by the fact that the monomer intramolecular frequencies are substantially higher than the helium-helium and monomer-helium frequencies; consequently, we focus on small clusters ranging in size from zero to fifteen helium atoms.

Theoretical approaches to frequency shifts of embedded impurities are quite varied and commonly employ multiple approximations[28]. Eichenaur and Leroy [29], for example, implemented a perturbation theory approach which was motivated by the work of Buckingham [31], where they calculated vibrational frequency shifts for SF_6 in argon clusters. The SF_6 molecule was treated as a harmonic oscillator, the SF_6-argon interaction was expanded in the corresponding normal coordinates, and the intermolecular interaction was a perturbation to the pure SF_6 Hamiltonian. In addition to both the harmonic and perturbation approximations, the surrounding cluster configuration was assumed unchanged during intramolecular vibrational excitation. Barnett and Whaley [30] used a similar approach to analyze SF_6 in helium clusters. Since the harmonic approximation ignores anharmonic contributions it is

likely to underestimate the magnitude of the shifts. Brown et. al. [32] performed an adiabatic Diffusion Monte Carlo calculation on N_2^+ embedded in helium clusters: the N_2^+ bond was held fixed while the molecule and the surrounding clusters rotated and translated during the simulation. They performed several simulations for different N_2^+ bond lengths, and thus obtained the total energy as a function of the N_2^+ separation. With the N_2^+ potential energy surface in the field of helium atoms, they were then able to calculate the energy levels and the corresponding frequency shifts. As with the studies of Eichenaur and Leroy, and Barnett and Whaley, they assumed that the cluster configuration is independent of intramolecular vibrational excitation.

Like Brown, we also employed DMC to determine frequency shifts; however, we kept all degrees of freedom in the simulation so that the water monomer high frequency motions were simulated right along with the helium-helium and helium-water interactions. We performed simulations for cluster sizes ranging from zero to fifteen helium atoms for the ground state, the first fundamentals of the asymmetric stretch, the symmetric stretch, and the bend modes of the monomer. Since we performed direct simulations, we avoided any harmonic approximations and assumptions regarding cluster configurations for intramolecular-impurity excitations. The primary drawback of our approach stemmed from the stochastic nature of DMC, since we had to contend with potentially large fluctuations that mask small frequency shifts.

The following chapters are organized as follows. We discuss our particular imple-

mentation of DMC, we present the details of the potential energy surfaces employed, and we discuss our results and the errors associated with our approach. In addition, we introduce a novel technique for calculating excited state properties in chapter 8; however, it was not employed in the monomer-helium work since more development is required.

7

Diffusion Monte Carlo

7.1 Monte Carlo Methods

Quantum Monte Carlo methods are most commonly employed to investigate medium to large quantum systems, such as Van der Waals clusters. Included in this family are Green's function Monte Carlo (GMC) [38], Variational Monte Carlo (VMC) [34], and Diffusion Monte Carlo (DMC). GMC is an exact method which is relatively difficult to implement and suffers from large statistical fluctuations. VMC, as its name implies, rests on the variational principal and provides approximate energies. DMC, like GMC, is an exact method and is often used in conjunction with VMC when biasing (importance sampling) is required.

The literature contains many excellent discussions of DMC [37, 33]. However, in

an attempt to increase accuracy, we utilized it in a slightly different manner. Consequently, we reintroduce the method here and discuss our particular implementation.

7.2 Evolution Operator

The fundamental equation for DMC is obtained by applying a transformation to the time dependent Schrödinger equation. If we substitute $\tau = it/\hbar$, the time dependent Schrödinger equation

$$i\hbar\frac{\partial}{\partial t}\psi(\vec{r},t) = \left[-\frac{\hbar^2}{2}\sum_{\alpha}(\frac{1}{m_\alpha}\nabla_\alpha^2) + V(\vec{r})\right]\psi(\vec{r},t), \tag{7.1}$$

becomes the diffusion equation

$$\frac{\partial}{\partial\tau}\psi(\vec{r},\tau) = \left[\frac{\hbar^2}{2}\sum_{\alpha}(\frac{1}{m_\alpha}\nabla_\alpha^2) - V(\vec{r})\right]\psi(\vec{r},\tau) \tag{7.2}$$

with the addition of a first order rate term in the form of the potential: note that the diffusion coefficient is $\hbar^2/(2m_\alpha)$.

Due to this transformation, the oscillatory solutions

$$\psi(\vec{r},t) = \sum_n e^{(-iE_nt/\hbar)}\,C_n\,\phi_n(\vec{r}) \tag{7.3}$$

are mapped onto pure exponential functions

$$\psi(\vec{r},\tau) = \sum_n e^{(-E_n\tau)}\,C_n\,\phi_n(\vec{r}). \tag{7.4}$$

Consequently, the components of the initial wave function either grow or decay exponentially along the imaginary time axis. Therefore, by using suitable constraints,

as discussed later, the ground state is projected out by propagating some arbitrary initial state in imaginary time (assuming the initial state contains the ground state as one of its components).

DMC implements the propagator in the configuration space representation. As with most propagation techniques, a split operator is utilized:

$$e^{(-\hat{H}\tau)} \approx e^{(-\hat{T}\tau)}e^{(-\hat{V}\tau)} \tag{7.5}$$

Since this form ignores the noncommuting nature of $\hat{T}$ and $\hat{V}$, it is only valid to first order in τ, and neglects terms to second and higher order; as a result, the propagation proceeds in an iterative manner by evolving the system through small increments in time, $\Delta\tau$.

The configuration representation for the potential propagator is straight forward, since it is simply a multiplication and represents a growth or decay, depending on the sign of the potential. With the operators separated, the form for the kinetic portion is obtained by recognizing that it satisfies the pure diffusion equation:

$$\frac{\partial}{\partial\tau}\int_{-\infty}^{\infty}\langle\vec{r}\,|e^{(-\hat{T}\tau)}|\vec{r}\,'\rangle\psi(\vec{r}\,',0)\,d\vec{r}\,' = \int_{-\infty}^{\infty}\nabla^2\langle\vec{r}\,|e^{(-\hat{T}\tau)}|\vec{r}\,'\rangle\psi(\vec{r}\,',0)\,d\vec{r}\,' \tag{7.6}$$

$$\frac{\partial}{\partial\tau}U(\vec{r},\vec{r}\,',\tau) = \nabla^2 U(\vec{r},\vec{r}\,',\tau) \tag{7.7}$$

where ∇^2 incorporates the diffusion constants and the sum over all particles, and

$$U(\vec{r},\vec{r}\,',\tau) = \langle\vec{r}\,|e^{(-\hat{T}\tau)}|\vec{r}\,'\rangle \tag{7.8}$$

is the free particle Green's function. Applying the delta function initial condition

$$U(\vec{r},\vec{r}',0) = \delta(\vec{r}-\vec{r}') \tag{7.9}$$

gives

$$U(\vec{r},\vec{r}'\tau) = \prod_{\alpha=1}^{N}(4\pi D_\alpha \tau)^{-3/2}\, e^{-(\vec{r}-\vec{r}')^2/(4D_\alpha\tau)} \tag{7.10}$$

where $D_\alpha = \hbar^2/(2m_\alpha)$. Hence, the kinetic propagator represents the time distribution obtained from a random walk.

7.3 Ground State DMC

7.3.1 Simple Algorithm

DMC propagation of the wave function proceeds in two stages. Since the kinetic operator represents a distribution from a random walk, the wave function is represented as a linear superposition of delta functions in configuration space (commonly denoted replicas) with a continuous weight, such that the sum of weights within a given volume represents the average amplitude of the wave function within that volume. Each replica is best thought of as a unique system and the collection of replicas comprises an ensemble. To propagate through one time increment, each atom in each replica is given a gaussian random displacement along each cartesian vector, with a root mean square displacement given by the Einstein relation $\sqrt{2D_\alpha\tau}$. The potential for each

replica is then calculated and the new weight of the replica obtained by multiplying its old weight by the potential propagator evaluated at that configuration.

As mentioned previously, the ground state distribution is obtained by inserting a suitable constraint into the propagation scheme; if the evolution operator is applied without a constraint, the replica weights grow without bound or vanish, see equation 7.4. So, many researchers employ the mechanism proposed by Anderson [37] or some variation thereof. In his scheme the DMC equation is modified by subtracting a constant, known as the "reference energy", from the potential energy:

$$\frac{\partial}{\partial \tau}\psi(\vec{r},\tau) = \left[\frac{\hbar^2}{2}\sum_{\alpha}\left(\frac{1}{m_\alpha}\nabla_\alpha^2\right) - (V(\vec{r}) - E_R)\right]\psi(\vec{r},\tau) \tag{7.11}$$

The effect of this modification is apparent in the corresponding solution:

$$\psi(\vec{r},\tau) = \sum_n e^{-(E_n - E_R)\tau}\, C_n\, \phi_n(\vec{r}). \tag{7.12}$$

Hence, when the reference energy is equal to the ground state energy, the time dependent coefficient for that basis state is stabilized, and the other components decay at a rate determined by $(E_n - E_r)$. This behavior is manifested by the sum total of the replica weights, known as the population. If E_R is smaller than E_0, the population decays, and if it is too high the population grows. Therefore, Anderson developed an algorithm for adjusting E_R to modulate population growth and decay, which adds an additional step to the propagation scheme. He derived an estimate for the growth or decay, due to an incorrect E_R, by expanding the potential propagator about $\Delta\tau$. If

only the linear term is kept, the following expression is obtained:

$$E_R = \bar{V} - \alpha \frac{(P - P_0)}{P_0} \tag{7.13}$$

with

$$\bar{V} = \frac{\sum_i w_i V_i}{P} \tag{7.14}$$

and

$$P = \sum_i w_i. \tag{7.15}$$

where α is a positive constant that is optimized via trial DMC simulations (initially set equal to 1 in most cases), w_i is the weight of the i^{th} replica, and P_0 is a constant representing the value at which to stabilize the population P. Notice that the second term on the right of equation 7.13 lowers E_R when the population grows, and raises E_R when the population shrinks. This equation thus acts as a feedback loop that modulates population growth and decay. After a sufficient time has elapsed, the wave function stabilizes to the ground state, and the feedback loop causes the reference energy to oscillate around E_0.

7.3.2 Energy Estimates

The ground state energy is typically estimated in two different ways. The first method is to average E_R over long production runs, after the simulation equilibrates to the ground state. The second method is to average the potential energy over all the

replicas and over time, again, after the simulation converges to the ground state. The first estimate is valid under all conditions, although it is typically subject to larger fluctuations than the second estimate; however, the second estimate is not always an estimate of the eigen energy, as illustrated below.

The equivalent continuous representation for the average potential energy, as shown in equation 7.14 (it is not an expectation value), is

$$\bar{V}(\vec{r}) = \frac{\int_{-\infty}^{\infty} V(\vec{r})\psi_n(\vec{r})\,d\vec{r}}{\int_{-\infty}^{\infty} \psi_n(\vec{r})\,d\vec{r}}. \tag{7.16}$$

To see when equation 7.16 is an estimate of E_n, consider integrating the Schrödinger equation.

$$\int_{-\infty}^{\infty} \frac{-\hbar^2}{2} \sum_{\alpha=1}^{N} \frac{1}{m_\alpha} \nabla_\alpha^2 \psi_n(\vec{r})\,d\vec{r} + \int_{-\infty}^{\infty} \psi_n(\vec{r}) V(\vec{r})\,d\vec{r} = E_n \int_{-\infty}^{\infty} \psi_n(\vec{r})\,d\vec{r} \tag{7.17}$$

The first term on the left is easily integrated and generally vanishes when the wave function asymptotically decays or when symmetry applies, as for the particle in a box. Ground state simulations usually meet these requirements and pose no problems. An excellent example where this estimate fails occurs for antisymmetric excited states, since the integral over ψ is identically zero. In such cases, the only estimate typically available is the time average of E_R (except when importance sampling is used, as shown later).

As discussed, DMC is a stochastic method which gives statistical estimates of ground state properties. For small molecular systems (3 atoms or less), simple DMC

will produce adequate convergence using modern computers. However, for larger systems further modification of the algorithm is required to achieve satisfactory results.

7.3.3 Importance sampling

A method known as importance sampling was initially introduced by Kalos [39] to reduce statistical fluctuations in GMC, and is now routinely implemented in most DMC algorithms. This method is extremely well covered in the literature [41, 33], so here we present the fundamentals of the technique.

Importance sampling makes use of a trial function which represents an approximation to the true wave function for the system of interest. A new function is then defined as $f = \psi\psi_t$, where ψ_t is the analytical representation of the trial function, and ψ is the true wave function for the system. After solving for ψ and substituting into the Schrödinger equation we obtain a modified equation for the function f:

$$\frac{\partial f}{\partial \tau} = \sum_k \frac{\hbar^2}{2m_k}\nabla_k^2 f - \sum_k \frac{\hbar^2}{m_k}\nabla_k(f\nabla_k \ln\psi_t) - (\frac{\hat{H}\psi_t}{\psi_t} - E_R)f \qquad (7.18)$$

The first term on the right is the diffusion term, the last is a modified growth decay term, and the middle is a drift term, with the drift velocity given by this expression:

$$\vec{v}_k = \frac{\hbar^2}{m_k}\nabla_k \ln\psi_t \qquad (7.19)$$

Equation 7.18 incorporates two important modifications to simple DMC. The first

is the addition of a drift step, where each atom in each replica is given a displacement:

$$\Delta\vec{r}_k = \Delta\tau\frac{\hbar^2}{m_k}\nabla_k \ln\psi_t. \tag{7.20}$$

The second is the modified growth-decay term $\frac{\hat{H}\psi_t}{\psi_t}$, known as the local energy. The local energy is now the estimate of the eigen energy, and is more robust than the potential energy estimate of unbiased DMC. The energy of the system is obtained by averaging the local energy over all the replicas and over time. That the local energy is an estimate of the eigen energy is shown here:

$$\frac{\int_{-\infty}^{\infty}\psi_n\psi_t\frac{H\psi_t}{\psi_t}d\vec{r}}{\int_{-\infty}^{\infty}\psi_n\psi_t d\vec{r}} = \frac{E_n\int_{-\infty}^{\infty}\psi_n\psi_t d\vec{r}}{\int_{-\infty}^{\infty}\psi_n\psi_t d\vec{r}} = E_n \tag{7.21}$$

where the fact that $\hat{H}$ is hermitian is utilized. This estimate is valid even for excited states, unlike the average potential energy estimate; without the local energy estimate, E_R is the only way, in general, to obtain excited state energies (see section 7.3.2).

Importance sampling reduces fluctuations via the drift term and the local energy. The drift term guides replicas into regions where the trial function is large, thus if it is a good representation of the true wave function the replicas will sample important regions of the true wave function more frequently. The local energy approaches the true eigen energy in the limit of an exact trial function; consequently, the better the trial function the more invariant the local energy is with respect to varying replica configurations. Conversely, fluctuations are magnified for poor trial functions which, incidentally, provides information on trial function quality. Trial functions

are typically empirical functions optimized by VMC or are obtained from *ab-initio* results.

7.4 Population Renormalization

It has been noted by many authors, most notably Umrigar [40], that the reference energy adjustment introduces a systematic error into the simulation. The reference energy adjustment is designed to adjust the reference energy based on linear decay or growth, due to the deviation from the true ground state energy, see equation 7.13. However, random fluctuations also affect the population size and are subsequently modulated by the reference energy adjustment. This creates a covariance in the fluctuations of the population size and the reference energy, which causes the replica distribution to deviate from the desired distribution $\psi_t\psi_0$. This deviation is usually not a problem until high accuracy is desired, as in our case. Umrigar provides an improved algorithm to reduce the covariance. We propose a simpler method which removes this bias, at the cost of losing the reference energy estimate for the eigen energy; this does not pose a problem since we utilize importance sampling and the local energy estimate.

Equation 7.4 shows that the components of the initial wave function either grow or decay exponentially in complex time. Furthermore, as time evolves, the ground state component becomes relatively larger than the other terms and thus dominates

the expansion after sufficiently long times. Therefore, the expansion converges to the ground state regardless of whether or not we apply a reference energy adjustment. The practical problem exists that the weights of the replicas become numerically intractable if the simulation is left to propagate without intervention (either they grow without bound or vanish). We decided to alter the simulation by simply removing the reference energy adjustment, and by renormalizing the weights after each time step. This keeps the population size constant while the relative changes in the wave function expansion coefficients are preserved. All of our results for the helium clusters were obtained using this modification.

7.5 Excited State Fixed Node DMC

As shown by equation 7.4, DMC projects out the ground state wave function of the system. Thus, all methods for obtaining excited state properties rely on applying constraints to the system so that the simulation relaxes to the excited state of interest. This effectively modifies the problem so that the ground state of the constrained system corresponds to the excited state of the unmodified system. There are several methods available, but each has its limitations and much research is still required to develop more efficient and flexible algorithms. Some currently applied techniques include orthogonalization constraints [51, 52], basis-set approaches coupled with quantum Monte Carlo for integral sampling [43], fixed node simulations,

and nodal relaxation schemes [42]. In our work we employed the fixed node approach and discuss it here. Furthermore, we began the development of a novel technique based on the fixed node implementation. We discuss that in a separate chapter since it was not used in our helium-monomer project, as further development is required.

Fixed node DMC relies on prior knowledge of the location of the node, which is its principal limitation. An absorbing wall is placed at the location of the node which confines the replicas to one region of configuration space. During the simulation the replicas diffuse, grow, and decay as usual with the modification that those which traverse the node meet their demise: their weight is set to zero. At that point the replica with the largest weight has its weight reduced by half and is then copied: the copy is placed in the memory location of the deleted replica. A great pedagogical example is a one dimensional harmonic oscillator, where the node is located at the minimum of the potential, for the first excited state. A typical simulation confines the replicas to either the right or left side of the node. As the propagation proceeds, the replicas remain on one side so that the distribution develops a node at the absorbing boundary. Again, as in ground state DMC, properties such as the energy are calculated once equilibrium is reached.

Since DMC is a finite time step simulation, there exists a source of error due to the presence of the absorbing boundary. During a time step there exists a finite probability that each replica will cross a node twice, i.e. thus crossing and recrossing.

Anderson [36] provides information on the recross probability as follows:

$$P_{recross} = \exp\left(\frac{-4\vec{r}\vec{r}'}{2\sigma^2}\right), \tag{7.22}$$

where $\sigma^2 = 2D_r\,\Delta\tau$ is the variance along the axis normal to the node and $\vec{r}$ and $\vec{r}'$ are the positions before and after the time step, respectively. Therefore, at the end of each time step the weight of each replica is scaled according to equation 7.22. Without this correction the error is quite significant for simple DMC. However, with biasing, using appropriate trial wave functions, the error is negligible [33]. For multiple dimensions it is critical to use the correct variance corresponding to the direction normal to the node.

8

Excited State Dynamic-Node DMC

8.1 Introduction

In this chapter we describe a novel DMC approach for calculating excited state energies, that we began developing with the idea that we would apply it to the monomer-helium project. The ideal method will not be as labor intensive as the orthogonalization constraint, not as restrictive as the fixed node approach, and not as potentially unstable as in the nodal relaxation scheme. Our idea potentially overcomes many of these barriers. In this chapter we describe the theory, present example simulations, and discuss future directions for further research.

8.2 Theory

The starting point for dynamic-node DMC is the simple fixed-node algorithm. Recall from the previous chapter that to obtain the excited state energy a hard absorbing wall is placed at the location of the fixed node. A distribution of replicas is then placed so that the entire ensemble is located within the same region relative to the node: to the left of the node in the first excited state of the harmonic oscillator, for example. As the simulation proceeds, the replicas diffuse and grow-decay as usual, with the exception of those that cross the node: they are eliminated and the replica with the largest weight has its weight halved, itself copied, and its twin placed in the memory location of the deleted replica. Dynamic-node DMC, like fixed-node DMC, also has an absorbing boundary at the predicted location of the node; however, rather than having one ensemble of replicas, multiple ensembles of replicas exist such that each ensemble is located in a separate region of configuration space, as determined by the nodal configuration. For example, in the first excited state of the one dimensional harmonic oscillator there are two ensembles, with one to the left and the other to the right of the node. The two ensembles are best described as interacting simulations. The key to the method is to monitor the difference between the energies from the two simulations as a function of the location of the node. If the location is correct. they will produce identical results and no adjustment is necessary. However, if the location is incorrect, then the energies predicted by the two ensembles will be different. The

algorithm thus incorporates a scheme for changing the location so as to converge the energies of the two simulations.

Given the stochastic nature of DMC, the instantaneous energies of the simulations will differ due to fluctuations. Consequently, the algorithm adjusts the location of the node at the end of each time step so that the time-averaged location is correct and deviations are averaged out. In order to determine how to move the node, we used a particle in a one dimensional box as the starting point. How is the energy of the box changed as the node is moved small distances? The ground state energy for the system is

$$E = \frac{\pi^2 \hbar^2}{2mL^2} \tag{8.1}$$

where L is the length of the box and m is the particle's mass. Now, if the edge of the box is moved a small distance Δx, the expression for the change in energy is

$$\Delta E \approx -\frac{\pi^2 \hbar^2}{mL^3} \Delta x. \tag{8.2}$$

Hence, for small distances, the change in energy is directly proportional to the nodal displacement:

$$\Delta x = -\epsilon \Delta E \tag{8.3}$$

where the proportionality constant, ϵ, is determined in trial DMC simulations to optimize convergence of the energies. The sign indicates that the energy decreases when the box size increases.

The elements for the dynamic-node scheme are now in place. With the node placed in some arbitrary initial position, the replicas diffuse and grow-decay as in simple DMC. At the end of each time step the nodal displacement is calculated: the difference in energies for each ensemble is taken and multiplied by ϵ. The node is then moved by an amount given by this product. The sign indicates that the location moves in a direction such that the higher energy region expands and the lower energy region contracts. This discussion makes two assumptions about the nodal characteristics: (1) the node has a shape, such as a line, plane, or sphere so that the node moves or expands-contracts (the sphere) such that its shape is conserved and (2) the direction to move the node is known. In the following sections we present results for some simple systems which meet these qualifications. In addition, we conclude with a discussion regarding current limitations and future research.

8.3 One Dimensional Morse Oscillator

8.3.1 System Description

In this section we discuss results obtained for a one dimensional Morse potential. The Morse potential, Morse eigen functions, and Morse eigen values are shown in equations 2.9, 2.13, and 2.12, ($\hbar = 1$) respectively. All the simulations used the same parameters, where the values, in dimensionless units, were $D = 10.0$, $a = 0.200$ (D

is the well depth and "a" is the preexponential factor), and the reduced mass was set to 1. Importance sampling was not used, so all energies were calculated from the time averaged E_R and the recross correction (equation 7.22) was applied for higher accuracy.

8.3.2 First Excited State

The objective of the simulation was to calculate the excited state energy as well as locate the node. The location of the node is given analytically as

$$\omega = \alpha - 1 \tag{8.4}$$

where

$$\omega = 2ke^{-ax}, \tag{8.5}$$

$$k = \sqrt{2mD}/a, \tag{8.6}$$

and

$$\alpha = 2k - 1. \tag{8.7}$$

Hence, the node is located at $x = 0.2288$ and the ground and first excited state energies are $E_0 = 0.442$ and $E_1 = 1.297$. The simulations were run using paired ensembles: 250 replicas were on each side of the node and the time step was $\Delta\tau = 0.0125$. Averages were collected over 3000 time steps, after a 500 step equilibration,

and the node's initial position was set to $x = 0$. Table 8.1 shows the results for several simulations with varying values of the nodal adjustment parameter ϵ, see equation 8.3.

Table 8.1: Dynamic-node, Morse first excited state simulation.

	E_1			Error		Error
ϵ	sim 1	sim 2	Average	%	Node	%
1.0×10^{-3}	1.312	1.288	1.300	0.23	0.203	11.
5.0×10^{-4}	1.298	1.290	1.294	0.23	0.218	4.8
2.5×10^{-4}	1.299	1.298	1.299	0.15	0.226	1.1

Notice that the error associated with the location of the node decreases as ϵ decreases. In general, convergence of the energies is more rapid for a larger ϵ, with the caveat that the error increases for both the location of the node and for the energies. Thus, the strategy is to use large values of ϵ for equilibration and small values when gathering data for energy estimates and for other properties (this is analogous to equilibrating with a large time step).

8.3.3 Second Excited State

Simulation of the second excited state required the introduction of 2 nodes, which are labeled as node A and node B. This in turn means that there were 3 nodal pockets and thus 3 ensembles. For the sake of clarity, the regions are labeled I, II, and III.

starting from the far left and proceeding to the far right: node A separated I and II and node B separated II and III. We set up an ensemble in each of the three regions and coupled the energies of regions I and II and the energies of regions II and III. Therefore, the movement of node A depended only on the energies in I and II and that of B depended on II and III, as shown by the following equations:

$$\Delta x_A = -\epsilon_A(E_{II} - E_I) \tag{8.8}$$

$$\Delta x_B = -\epsilon_B(E_{III} - E_{II}) \tag{8.9}$$

The sign indicates that node A moved to the left when E_{II} was greater than E_I, i.e. region II expanded and region I contracted. The same reasoning applies to regions III and II. We again used 250 replicas within each nodal pocket, a time step of 1.25×10^{-3}, and $\epsilon_A = \epsilon_B = 5.00 \times 10^{-4}$. Averages were collected over 8000 time steps, after a 2000 step equilibration, and node A started at $x = -0.5$ and node B at $x = 1.0$. Table 8.2 highlights the results obtained from one simulation. Smaller errors are obtained by decreasing the values of ϵ and by running for longer times.

8.3.4 Third Excited State

The third excited state has 3 nodes which are labeled, from left to right, A, B, and C, and the four concurrent simulations are labeled I, II, III and IV. The coupling followed the same convention as in the second excited state, so that only neighboring nodal pockets were coupled. Average energies were collected over 3000 steps, after

Table 8.2: Dynamic-node, Morse second excited state simulation.

E	$\bar{E}$	Exact E	Error %	DMC Node	Exact Node	Error %
$E_I = 2.094$				A = -0.348	-0.373	6.7
$E_{II} = 2.123$	2.120	2.111	0.4			
$E_{III} = 2.143$				B = 1.206	1.189	1.4

equilibrating for 2000 steps. Each region used 250 replicas, the time step was 1.25×10^{-3} and $\epsilon_A = \epsilon_B = \epsilon_C = 1.00 \times 10^{-3}$. The results are highlighted in table 8.3.

Table 8.3: Dynamic node Morse third excited state simulation.

E	$\bar{E}$	Exact E	Error %	DMC Node	Exact Node	Error %
$E_I = 2.894$				A = -0.759	-0.763	-0.52
$E_{II} = 2.899$	2.901	2.886	0.52	B = 0.528	0.551	4.17
$E_{III} = 2.904$				C = 1.918	1.993	3.76
$E_{IV} = 2.905$						

The energy converged more quickly for this simulation than for the second excited state and required a shorter simulation. The number of replicas within each nodal

region remained constant for the first, second and third excited state examples, but the regions contracted as the number of nodes increased. This led to an increase in the replica density per unit volume and a corresponding decrease in the energy fluctuations per time step. Also note that it is not necessary for ϵ to be the same for each node, as in all the examples shown.

8.4 Hydrogen Fluoride

8.4.1 System Description

As a further test, a simple diatomic molecule was modeled in three dimensions. The molecule chosen was hydrogen fluoride and simulations were conducted in the center-of-mass frame. The Hamiltonian, in relative radial coordinates, has the following form (atomic units):

$$-\frac{1}{2\mu}\frac{1}{r}\frac{\partial^2}{\partial r^2}r + \frac{1}{r^2}\left(\frac{1}{\sin\theta}\frac{\partial}{\partial\theta}\sin\theta\frac{\partial}{\partial\theta} + \frac{1}{\sin^2\theta}\frac{\partial^2}{\partial\phi^2}\right) + V(r) \tag{8.10}$$

where μ is the reduced mass and has the value 1744.68 m_e for HF (m_e is the electron rest mass). The potential used was developed by Sun and Watts [52] with the exception that we chose the unperturbed Morse oscillator form (for easy comparison to exact energies):

$$V(r) = \left(1 - e^{-a(r-r_e)}\right)^2 V_e \tag{8.11}$$

with $V_e = 0.18379$, $a = 1.29938$, and $r_e = 1.73278$.

In order to compare DMC nodal positions and energies to analytical values, the rigid rotor approximation was used. The eigenfunctions are

$$\phi_{\nu,l,m}(r,\theta,\phi) = R(r)Y_l^m(\theta,\phi) \tag{8.12}$$

with

$$R(r) = \frac{1}{r}\chi_\nu(r) \tag{8.13}$$

where $\chi_\nu(r)$ is the solution to the one dimensional Morse Hamiltonian (see equation 2.13) and $Y_l^m(\theta,\phi)$ is a spherical harmonic. The eigenvalues are simply the sum of the Morse-radial energies and the rotational energies:

$$E_{\nu,l} = E_\nu + B\,2\pi\,l(l+1) \tag{8.14}$$

where B is the rotational constant for HF and is equal to 1.5191×10^{-5} *hartrees*.

In the following subsections we describe the simulations and summarize the results. The nodal positions are well determined within the rigid rotor approximation. Simulations were run for both excited rotational and vibrational states as follows: (1) $\nu = 0$, $l = 1$, (2) $\nu = 0$, $l = 2$, (3) $\nu = 1$, $l = 0$ and (4) $\nu = 1$, $l = 1$.

8.4.2 $\nu = 0,\ l = 1$

For the first excited rotational state there are three degenerate eigen values corresponding to the azimuthal quantum numbers $m = -1, 0, 1$. The spherical harmonics

are

$$Y_1^1(\theta,\phi) = -\sqrt{\frac{3}{8\pi}}\sin\theta e^{i\phi} \tag{8.15}$$

$$Y_1^0(\theta,\phi) = \sqrt{\frac{3}{4\pi}}\cos\theta \tag{8.16}$$

$$Y_1^{-1}(\theta,\phi) = \sqrt{\frac{3}{8\pi}}\sin\theta e^{-i\phi} \tag{8.17}$$

Since these states are degenerate, taking the appropriate linear combinations of $Y_1^1(\theta,\phi)$ and $Y_1^{-1}(\theta,\phi)$ produces two new real eigenstates so that there are three real eigenfunctions. The three eigenfunctions each have one planar node which are in the xy, xz, and yz planes. The simulation in this example had a nodal barrier that was parallel to the xy plane. The nodal adjustment moved the entire plane along the z-axis while keeping the plane parallel to the xy plane. Thus, the simulation was analogous to the one dimensional case with a point node.

8.4.3 $\nu = 0,\ l = 2$

The second excited rotational state has five degenerate eigenvalues with five spherical harmonic eigenfunctions. Taking linear combinations of $Y_2^{-2}(\theta,\phi)$ and $Y_2^2(\theta,\phi)$ produces two new real eigenfunctions:

$$\frac{1}{\sqrt{2}}\left(Y_2^2(\theta,\phi) + Y_2^{-2}(\theta,\phi)\right) = \sqrt{\frac{15}{64\pi}}\sin^2\theta\cos 2\phi \tag{8.18}$$

$$\frac{1}{\sqrt{2}}\left(Y_2^2(\theta,\phi) - Y_2^{-2}(\theta,\phi)\right) = \sqrt{\frac{15}{64\pi}}\sin^2\theta\sin 2\phi \tag{8.19}$$

This example corresponds to the state described by equation 8.19. The nodes are both planar and lie in the xz and yz planes. This creates four nodal regions where only three are necessary to move the nodes; therefore, the three simulations were run in the quadrants (x,y), (x,-y), and (-x,y) and are labeled I, II, and III respectively. Similarly to the one dimensional case, the simulations I and II were coupled as well as I and III. The nodes were constrained to remain parallel to the axial planes and were thus moved along the x and y axes.

8.4.4 $\nu = 1, l = 0$

This scenario required a radial node, which is simply a sphere with the center placed at the origin. Movement of this node involved a simple expansion-contraction by Δr, while the center remained fixed. This caused a volume change that scaled as Δr^3, which raises the question as to whether or not we could apply equation 8.3 in this manner. We applied it nonetheless, and found that it was able to converge the energies, as shown in the following results. However, this issue was not thoroughly explored, by any means, and there are, most likely, more efficient ways to achieve convergence.

8.4.5 $\nu = 1, l = 1$

This state has a spherical node centered at the origin and a node parallel to the xy plane. As with the $l = 2$ example, three simulations were run with the replicas placed in the following regions: (I) $+z$ hemisphere and inside the region bounded by the spherical node, (II) in the -z hemisphere and inside the spherical node, and (III) in the $+z$ hemisphere and outside the spherical node. Simulations I and III were coupled and controlled the expansion and contraction of the radial node. Simulations I and II were coupled and controlled movement of the planar node: it moved as in previous examples, so that it was constrained to remain parallel with the xy plane and moved along the z axis.

8.4.6 Results

All the results for HF are shown in table 8.4. All the examples used 500 replicas (within each nodal region), a time step of $\Delta\tau = 0.05\ hartrees^{-1}$, and the average energies were collected for a total of 300,000 time steps. Also, the recross correction was applied to correct for the presence of the nodes and to achieve higher accuracy. In all the cases shown, the nodes were given an arbitrary initial position and all converged to the correct location. Again, better agreement is obtained by reducing the nodal adjustment parameter and by decreasing the time step; which then requires a larger total number of steps. In this simple system dynamic-node DMC easily handled

multiple nodes simultaneously and nodes of different configurations.

Table 8.4: HF dynamic-node DMC results.

	DMC		Exact	
State	Energy cm^{-1}	Node Location	Energy cm^{-1}	Node Location
$\nu = 0, l = 1$	$E_I = 2077.5$ $E_{II} = 2079.0$	0.00654	2085.1	0.0
$\nu = 0, l = 2$	$E_I = 2176.8$ $E_{II} = 2174.8$ $E_{III} = 2179.6$	$A = -0.052$ $B = 0.11$	2168.9	y = 0.0 x = 0.0
$\nu = 1, l = 0$	$E_I = 5954.3$ $E_{II} = 5955.3$	1.78	5970.2	r = 1.773
$\nu = 1, l = 1$	$E_I = 6002.9$ $E_{II} = 6001.9$ $E_{III} = 5997.4$	$A = 1.77$ $B = -0.066$	6012.1	r = 1.773 z = 0.0

8.5 Future Developments

We have demonstrated the dynamic node method for several simple cases. We have seen that, for these examples, it easily estimates energies for states with multiple nodes. It also works with spherical as well as planar nodes. Polyatomic molecules obviously present greater challenges.

An important issue which needs addressing is how to successfully incorporate importance sampling with this method. Large systems with many atoms, such as clusters, require the use of biasing methods to obtain results with satisfactory statistics. In importance sampling, as discussed, a trial function is used to guide the walkers. Consequently, for excited states the trial function will contain nodes. The challenge is to devise a method which allows the node in the trial function to move along with the dynamic node. The other alternative is to devise alternate biasing methods which more easily incorporate moving nodal surfaces.

Another issue concerns cases where the configuration of the node is unknown. One possible way to determine the shape is to assume some initial nodal configuration. It is then possible to couple DMC to an optimization method, such as simulated annealing, which allows the node to deform and move until the configuration which minimizes the energy differences is obtained. The primary obstacle here is to reduce the statistical fluctuations by somehow incorporating a trial wave function that incorporates the dynamic node.

9

System Potentials

9.1 Introduction

Unlike rigid body approaches, we allow all the molecules in the system to translate, rotate and vibrate. Consequently, we need to use potentials which describe the intramolecular motions of the water monomer, the intermolecular interactions of the monomer and the helium, and the interatomic interactions of the helium atoms. We employed potentials given in the literature for the helium-helium interactions and the water intramolecular motions as described below. After searching the literature, we were unable to find a potential which fully models the monomer-helium interactions, so we describe a semiempirical potential we constructed.

9.2 Water Monomer

In order to model the intramolecular distortions of the water monomer, we employed the potential developed by Reimers and Watts and later modified by Coker, Miller and Watts [48, 33, 49]. In their model, the potential is written in terms of the three local modes:

$$s_1 = R_1 \cos\left[\frac{1}{2}(\theta - \theta_0)\right] - R_0, \tag{9.1}$$

$$s_2 = R_2 \cos\left[\frac{1}{2}(\theta - \theta_0)\right] - R_0, \tag{9.2}$$

$$s_3 = \left[\frac{(R_1 + R_2)}{R_0}\right] \sin\left[\frac{1}{2}(\theta - \theta_0)\right]. \tag{9.3}$$

R_1, R_2, and θ are the bond lengths and bond angle respectively, and R_0 and θ_0 are the corresponding equilibrium values. The potential surface is expressed as a sum of three Morse potentials and a simple quadratic coupling between s_1 and s_2 (the modification introduced by Coker, Miller and Watts):

$$V(s_1, s_2, s_3) = M_a(s_1) + M_a(s_2) + M_b(s_3) + f_{12} s_1 s_2 \tag{9.4}$$

$$M_a(s) = D_a(\exp[-\alpha_a s] - 1)^2 \tag{9.5}$$

They fit the parameters in the potential by performing a large basis set vibrational calculation for 56 vibrational levels for H_2O, D_2O, and HDO. The parameters for the potential are given in table 9.1.

Table 9.1: Monomer potential energy parameters, atomic units are used.

$D_a = 0.20916$	$D_b = 0.15660$
$\alpha_a = 1.1331$	$\alpha_b = 0.7060$
$R_0 = 1.8088$	$\theta_0 = 104.52°$
$f_{12} = -0.0067622$	

9.3 Helium-Water Intermolecular Potential

Currently, very little information exists for the full intermolecular interaction between a water monomer and a helium atom. However, Palma and others [44, 45, 46] have performed extensive *ab-initio* calculations on a rigid monomer and a helium atom in order to study broadening of water microwave lines due to helium atom collisions. Consequently, we constructed a semiempirical potential based on their HFD (Hartree-Fock plus damped dispersion) potential which allows intramolecular distortions of the water monomer.

A Hartree-Fock plus damped dispersion model combines the self-consistent field (Hartree-Fock) calculations for the short range repulsive part of the potential with a damped dispersion interaction for the long range attractions. The potentials thus take the form:

$$V(\vec{r}) = V_{SCF}(\vec{r}) - f(\vec{r}) \sum_{n>6} \frac{C_n}{R^n} g_n(\vec{r}) \tag{9.6}$$

where the C_n's are the long range dispersion terms, $f(\vec{r})$ is a damping function, and the $g_n(\vec{r})$'s are general functions used for fitting purposes (such as spherical harmonics). Palma et. al. provide discrete points for the SCF potential and the necessary parameters for the analytical damped dispersion potential. However, their potential only accounts for the interactions of a rigid water molecule and a helium atom. Since we wished to include intramolecular distortions, we fit their SCF data to a pairwise additive site-to-site potential:

$$\begin{aligned} V(r_{H_1}, r_{H_2}, r_{CM}) &= A_H \exp(-a_H r_{H_1} - b_H r_{H_1}^2) \\ &+ A_H \exp(-a_H r_{H_2} - b_H r_{H_2}^2) \\ &+ A_{CM}(\theta,\phi)\, \exp(-a_{CM}(\theta,\phi)\, r_{CM} - b_{CM}(\theta,\phi)\, r_{CM}^2) \\ &- \frac{a_I(\theta,\phi)\, \mu^2 \alpha}{r_{CM}^6 + 0.01} - V_{DISP}(r_{CM},\theta,\phi) \end{aligned} \tag{9.7}$$

$$V_{DISP}(r_{CM},\theta,\phi) = F(r_{CM}) \sum_{\lambda,\mu} \sum_{n} C_n^{\lambda,\mu}\, r_{CM}^{-n}\, P_\lambda^\mu(\cos\theta) \cos(\mu\phi) \tag{9.8}$$

$$\begin{aligned} F(r_{CM}) &= \exp[-\gamma(D/r_{CM} - 1)^2], \quad R \le D \\ &= 1, \qquad\qquad R > D \end{aligned} \tag{9.9}$$

where $n = 6, 8, 10$ for the isotropic part of the potential ($\lambda = \mu = 0$), r_{H_i} is the distance of the helium atom from hydrogen atom H_i, r_{CM} is the distance of the helium atom from the water monomer center of mass, $\alpha = 1.383113\ a_0^3$ is the polarizability of helium, and $\mu = 0.736\ ea_0$ is the dipole moment of water. This pair potential was

fit to equal the rigid body potential when the water monomer is in the equilibrium configuration, and to naturally account for intramolecular distortions.

Notice that the dispersion potential and the center of mass part of the site-to-site potential are angularly dependent. The coordinate system we used to define these angles is described in terms of the monomer bond vectors so that it is consistent with the potential of Palma et. al., and so it is easily applied to a distorted monomer configuration during the quantum simulations. The origin is located at the center of mass of the monomer and the negative z axis points in the direction of the sum of the two O $\rightarrow$ H bond vectors. When the O-H bonds are the same length, as in the equilibrium configuration, the z axis forms the bisector of the H-O-H angle. The x axis is normal to the monomer plane and is formed from the cross product of the two O $\rightarrow$ H bond vectors. The y axis is normal to the xz plane and is formed from the cross product of the z unit vector and the x unit vector. Defining the axes this way makes the positive directions of the x and y axes dependent on the order of the cross products, but these are not important since the angular functions have the water monomer C_{2v} symmetry.

The pairwise potential was fit to the SCF data using a downhill simplex method. The water monomer was held fixed in its equilibrium configuration and placed in the yz plane with the center of mass at the origin: O(0,0,0.12390) and H(0,$\pm$1.43039, -0.98323).

The parameters of the potential were optimized for each of the eight angular directions. Once this was accomplished, we had a discrete angular representation for all the site-to-site functions. The helium-hydrogen terms were essentially constant as a function of angle, so they were simply averaged and made angularly independent: with $A_H = 2.9704$, $a_H = 2.355$, and $b_H = 0.000$ (atomic units). The center-of-mass functions were each fit to eight terms in an associated Legendre polynomial, where only those consistent with the C_{2v} symmetry were kept. The Legendre coefficients for the center-of-mass functions are shown in table 9.3. The resulting pair potential fits the SCF data to better than 1% with the exception of those points with an energy near zero; since the potential in that region is dominated by the attractive dispersion potential, this is not a concern.

The dispersion potential (given by Palma et. al.) is also expanded in associated Legendre polynomials, again, with only even μ included, due to the C_{2v} symmetry of the monomer. As mentioned earlier, the isotropic portion of the dispersion potential contains the three leading terms $n = 6, 8$, and 10, with $C_n^{00} = \sqrt{4\pi}\,\tilde{C}_n^{00}$. Furthermore, the leading anisotropic terms are given below in terms of the polarizability tensors of water $\boldsymbol{\alpha}$ and $\mathbf{A}$, and the coefficients $\tilde{C}_n^{00}$. The parameters are given in table 9.2, as provided by Palma et al [44]:

$$C_6^{20} = \left(\frac{1}{6}\right)\left(\frac{4\pi}{5}\right)^{1/2}\left[(2\alpha_{zz} - \alpha_{yy} - \alpha_{xx})/\alpha\right]\tilde{C}_6^{00} \tag{9.10}$$

$$C_6^{22} = \left(\frac{2\pi}{15}\right)^{1/2}\left[(\alpha_{xx} - \alpha_{yy})/\alpha\right]\tilde{C}_6^{00} \tag{9.11}$$

$$C_7^{10} = \left(\frac{2}{3}\right)\left(\frac{4\pi}{3}\right)^{1/2}[9(A_{zzz}+A_{yyz}+A_{xxz})/(5\alpha)]\,\tilde{C}_6^{00} \quad (9.12)$$

$$C_7^{30} = \left(\frac{4}{15}\right)\left(\frac{4\pi}{7}\right)^{1/2}\{[3A_{zzz}-2(A_{yyz}+A_{xxz})]/\alpha\}\,\tilde{C}_6^{00} \quad (9.13)$$

$$C_7^{32} = \left(\frac{8}{3}\right)\left(\frac{2\pi}{105}\right)^{1/2}\{[A_{zzz}-2(A_{xxz}-A_{zxx}-A_{yyz})]/\alpha\}\,\tilde{C}_6^{00} \quad (9.14)$$

with $\alpha = (\alpha_{xx}+\alpha_{yy}+\alpha_{zz})/3$.

Table 9.2: HFD potential parameters of Palma et al. All values are given in atomic units.

$\tilde{C}_6^{00}$ = 8.13	$\tilde{C}_8^{00}$ = 120.63
$\tilde{C}_{10}^{00}$ = 2079.80	α_{xx} = 9.55
α_{yy} = 10.31	α_{zz} = 9.91
A_{xxz} = -1.786	A_{yyz} = -6.742
A_{zzz} = -2.194	A_{zxx} = 4.070
D = 9.51	γ = 0.5

9.4 Helium Interatomic Potential

We employed the HFD-B form of the interatomic potential constructed by Aziz [47]. The potential reproduces a wide range of experimental data over a wide temperature range. As noted by the authors, it has been fitted to low temperature second virial coefficient data. It reproduces, to within experimental error, viscosities and thermal

Table 9.3: Water-Helium SCF associated Legendre coefficients for center-of-mass parameters. Atomic units are used.

Potential Term	Legendre Term	$c_{\lambda,\mu}$	Potential Term	Legendre Term	$c_{\lambda,\mu}$
A_{CM}	P_0^0	13.6241	a_{CM}	P_0^0	1.53105
	P_1^0	6.40671		P_1^0	0.436038
	P_2^0	-0.96998		P_2^0	-0.0893347
	P_2^2	0.513426		P_2^2	0.0732147
	P_3^0	-5.39231		P_3^0	-0.475025
	P_3^2	-0.73529		P_3^2	-0.0750838
	P_4^0	5.82598		P_4^0	0.414184
	P_4^2	0.0271438		P_4^2	0.0193492
b_{CM}	P_0^0	0.0496693	a_I	P_0^0	1.96122
	P_1^0	-0.0309269		P_1^0	-1.02642
	P_2^0	0.00870105		P_2^0	0.303297
	P_2^2	-0.00993475		P_2^2	-0.0570502
	P_3^0	0.0453224		P_3^0	-0.374764
	P_3^2	0.00707002		P_3^2	-0.0633476
	P_4^0	-0.0424976		P_4^0	0.591206
	P_4^2	-0.00169719		P_4^2	0.0400663

conductivities, differential cross sections, high energy integral cross sections and backward glory oscillations in the integral cross sections. It also supports a weakly bound state, which is critical for cluster formation, in ^{4}He, with well depth of 10.948K. The form of the potential is given below and the parameters are shown in Table 9.4.

$$V(r) = \varepsilon V^*(x) \tag{9.15}$$

$$V^*(x) = A^* \exp(-\alpha^* x + \beta^* x^2) - F(x) \sum_{j=0}^{2} c_{2j+6}/x^{2j+6} \tag{9.16}$$

$$F(x) = \begin{cases} \exp\left[-\left(\frac{D}{x} - 1\right)^2\right], & x < D, \\ 1, & x \geq D, \end{cases} \tag{9.17}$$

$$x = \frac{r}{r_m} \tag{9.18}$$

Table 9.4: Helium Interatomic Potential Parameters of Aziz

Parameters for HFD-B(He) potential	
A^*	1.8443101×10^5
α^*	10.43329537
c_6	1.36745214
c_8	0.42123807
c_10	0.17473318
$C_6/a.u$	1.461
$C_8/a.u$	14.11
$C_10/a.u$	183.5
β^*	-2.27965105
β	-0.259660
D	1.4826
$\frac{\epsilon}{k}$ K	10.948
r_m/A	2.963
σ/A	2.6369

Not all the figures are significant; they are displayed to avoid round off errors.

10

Trial Wave Functions

As discussed, we performed DMC calculations for the ground state, the asymmetric stretch, the symmetric stretch, and the bend first excited states of the monomer embedded in helium clusters. Importance sampling was implemented along with the fixed node approach for calculating the excited state properties. For each excited state calculation, we assumed that the location of the node was invariant and independent of cluster size. Furthermore, for each simulation, we constructed simple product trial wave functions, where each function consisted of products of a monomer intramolecular wave function, a monomer-helium intermolecular wave function, and a helium-helium interatomic wave function:

$$\psi_t(s_1, s_2, s_3, \vec{r}, \vec{q}) = \Phi(s_1, s_2, s_3)\chi(\vec{r})Y(\vec{q}) \tag{10.1}$$

where the s's represent the water intramolecular coordinates, $\vec{r}$ the water-helium coordinates, and $\vec{q}$ the helium-helium coordinates. Consequently, all simulations used identical monomer-helium and helium-helium functions. The excited state intramolecular monomer trial wave functions were constructed to contain the same symmetry as the corresponding normal modes of the isolated monomer. The specifics of each trial wave function are discussed in the following sections.

10.1 Ground State

10.1.1 Monomer Intramolecular Trial Function

In choosing an appropriate intramolecular monomer wave function we drew on the work of Suhm and Watts [33]. In their studies they expanded the wave function in a product basis of the local mode coordinates, where Morse functions were the basis and the local coordinates were defined as in section 9.2:

$$\Phi(s_1, s_2, s_3) = \sum_{j_1}\sum_{j_2}\sum_{j_3} c_{j_1,j_2,j_3} \prod_{i=1}^{3} \phi_{j_i}(s_i) \tag{10.2}$$

$$c_{j_1,j_2,j_3} = \int \psi^*(s_1, s_2, s_3) \prod_{i=1}^{3} \phi_{j_i}(s_i) J_s ds_1 ds_2 ds_3 \tag{10.3}$$

The j's label the basis functions, the i's label the local modes, and J_s is the Jacobian. The wave function was expanded using single oscillator states such that $j = 0, 1, 2$ and the corresponding coefficients in the expansion were calculated using simple DMC:

they averaged over the analytic representations of the basis functions. They found that the leading c_{000} term was at least 20 times larger than the higher order terms, thus indicating that the basis was rapidly convergent. Consequently, we decided to use just the leading term in the expansion and our trial wave function had the following form:

$$\Phi(s_1, s_2, s_3) = \phi_0(s_1)\phi_0(s_2)\phi_0(s_3) \tag{10.4}$$

where, as previously noted, Morse functions were used, see equation 2.13.

10.1.2 Monomer-Helium Intermolecular Trial Function

In section 9.3 we discussed the helium-monomer interaction potential. Given that it is weakly anisotropic and that we concentrated on small to medium clusters, we decided to use a simple Morse function for the intermolecular trial function; consequently, the interaction treats the monomer as a sphere with the center located at the monomer center of mass:

$$\chi(\vec{r}) = \phi_0(r - r_0) \tag{10.5}$$

where $\phi_0(r-r_0)$ is defined in equation 2.13, r is the distance between the helium atom and the monomer center of mass, and μ is the reduced mass determined from the total monomer mass and the helium atom mass. This form of the function works well for cluster sizes where the first shell about the impurity molecule is not yet complete. The parameters for the Morse function were obtained by spherically averaging the

intermolecular potential and fitting it to a Morse potential: the parameters are $D = 7.8 \times 10^{-5}$, $\alpha = 0.95$, and $r_0 = 6.75$.

10.1.3 Helium-Helium Intermolecular Trial Function

There is a wealth of information in the literature on helium-helium interactions and the corresponding wave functions. In our study we made use of a commonly employed 2-body wave function of the form:

$$Y(q_{ij}) = \exp\left\{-\frac{1}{2}\left[\left(\frac{b}{q_{ij}}\right)^5 + \frac{\alpha_0}{q_{ij}^2}\right]\right\} \tag{10.6}$$

where q is the helium-helium distance. In principle, we could include one and three body wave functions; however, the one body wave function, which serves to hold the cluster together, becomes insignificant in the presence of an impurity [55], and three body-effects were found, by Krishna and Whaley [53], to be insignificant for clusters sizes smaller than twenty helium atoms. Using variational Monte Carlo we optimized the parameters and set (atomic units) $b = 6.0$ and $\alpha_0 = 0.0$.

10.2 Asymmetric Stretch

The first fundamental for the asymmetric stretch mode of the monomer has a nodal location which is known exactly. The wave function is antisymmetric with respect to interchange of the two O-H stretch coordinates s_1 and s_2. Consequently, we utilized

the simplest antisymmetric local mode product state $|\psi_t\rangle = |1\rangle|0\rangle|0\rangle - |0\rangle|1\rangle|0\rangle$, where the quantum numbers correspond to the three local mode coordinates s_1, s_2, and s_3 respectively. The node for this state is located at $s_1 = s_2$.

10.3 Symmetric Stretch

Unlike the asymmetric stretch mode, the location of the node for the first fundamental of this state is only approximately known. The trial function however, must be symmetric with respect to interchange of the two local mode coordinates s_1 and s_2. The simplest symmetric product state corresponding to this mode is $|\psi_t\rangle = |1\rangle|0\rangle|0\rangle + |0\rangle|1\rangle|0\rangle$, where again the quantum numbers correspond to the local mode coordinates. The node used in our simulations was located where $s_1 = -s_2$, which is the location of the node for the symmetric stretch normal mode. Although the node of the symmetric local mode wave function and node of the normal mode do not exactly coincide, the results obtained agree remarkably well with the literature, as shown by our results.

10.4 Bend

Similarly to the symmetric stretch, the location of the first fundamental for the bend mode is known only approximately. The simplest bend product state is $|\psi_t\rangle =$

$|0\rangle|0\rangle|1\rangle$ and the node of the corresponding normal mode is $s_3 = 0$. The results for the isolated monomer were compared with experimental results, as shown subsequently.

11

Results and Conclusions

11.0.1 Simulation Parameters and Errors

Using the trial wavefunctions described in the previous chapter, separate simulations were run for the ground state energies and for the fundamentals in the asymmetric, symmetric, and bend modes of the monomer. Placing nodes in the intramolecular wave function implicitly assumes that the intermolecular and intramolecular modes are separable. This is an excellent approximation since the intramolecular frequencies are on the order of 600 times larger than the $He - H_2O$ intermolecular ones. However, as previously mentioned, we included all degrees of freedom, which therefore restricted the time step to small values in order to accurately simulate the intramolecular vibrations. In DMC, the energy fluctuates about the ground state energy as a function of imaginary time, and the frequency of the fluctuation is a function of the potential

or local energy (simple or biased simulations). The great disparity between the intramolecular and intermolecular frequencies creates fluctuations that occur on vastly different time scales. Therefore, in order to calculate energies that were converged to half a wave number required long computational runs.

In addition to the high frequency intramolecular motions, the nodes further restricted the time steps to small values for the excited states: recall that there is a finite probability of a replica crossing and recrossing a node during a single time step. This probability decreases for smaller time steps and so does the associated error. Therefore, all our excited state simulations were conducted using time steps that were smaller than the ground state values.

With some exceptions (some were run for longer times to check convergence), all the simulations for the ground state used 1000 replicas, a time step of 5.0 $hartrees^{-1}$ and were run for a total time of 150,000 $hartrees^{-1}$. The effect of the time step on the ground state energy was tested on the isolated monomer for $\Delta\tau = 0.50$, 5.0 and 10.0 $hartrees^{-1}$ for a total time of 600,000 $hartrees^{-1}$. No significant difference in the energies was observed (they agreed at the first decimal place) for $\Delta\tau = 0.5\, hartree^{-1}$ and $\Delta\tau = 5.0\, hartrees^{-1}$, while $\Delta\tau = 10.0\, hartrees^{-1}$ gave a value that was about 1 cm^{-1} lower. Most of the ground state simulations thus used $\Delta\tau = 5.0\, hartrees^{-1}$ and were run for a total of time $150,000\, hartrees^{-1}$.

The simulations for the first fundamentals of the asymmetric stretch, the sym-

metric stretch, and the bend modes also used 1000 replicas. However, as mentioned previously, the presence of a node introduced an additional source of error that increased with increasing time steps. We tested the isolated monomer asymmetric stretch mode for $\Delta\tau = 0.50$, 1.0, 2.5 and 5.0 $hartrees^{-1}$ for a total time of 300,000 $hartrees^{-1}$. The energy difference for $\Delta\tau = 0.5\ hartree^{-1}$ and $\Delta\tau = 1.0\ hartree^{-1}$ was less than 0.3 cm^{-1} while $\Delta\tau = 2.50\ hartrees^{-1}$ and $\Delta\tau = 5.0\ hartrees^{-1}$ gave energies that were 1.0 cm^{-1} and 2.0 cm^{-1} lower, respectively. Therefore, all the excited state simulations used $\Delta\tau = 1.0\ hartree^{-1}$ and most were run for a total time of $150,000\ hartrees^{-1}$.

We noticed during the simulations that the energy fluctuations in the excited state simulations were small than those of the ground state. As discussed in the dynamic-node DMC chapter, the energy fluctuations for excited state simulations were lower than those of the ground state. This may have to do with the increased number of replicas per unit volume. The presence of the node effectively halves the available configuration space thus increases the replica density.

The frequencies obtained by difference of the ground and respective first fundamentals of the isolated monomer were compared with the experimental values obtained from Robertson and Williams [50]. The results are shown in table 11.1. In addition, our ground state energy of 4622 cm^{-1} matches that obtained by Lewerenz and Watts [54], using DMC, of 4622 cm^{-1} and the variational calculation of Coker

and Watts who obtained 4623 cm^{-1}.

Table 11.1: Comparison for DMC frequencies to the experimental values of Robertson and Williams. All energies are in wave numbers.

Mode	DMC	Exp.	Error %
Bend	1600	1595	0.3
Symmetric	3648	3657	-0.2
Asymmetric	3752	3756	-0.1

11.0.2 Energies

The energies for helium atom cluster sizes ranging from 0 to 15 helium atoms are shown in figures 11.1, 11.2, 11.3, and 11.4. One striking feature of all the plots is the linear decrease in the energy as a function of the number of helium atoms. This is the behavior that is expected if the helium-helium interaction is neglected and the only additional contribution to the total energy is the helium-water interaction. The dissociation energy for the helium-water interaction is approximately 5 cm^{-1} (obtained by fitting the spherically average potential to a Morse potential) for the potential employed, which closely approximates the slopes. The linear decrease continues until we reach 13 helium atoms, at which point the slope changes. This is consistent with the completion of a helium shell about the monomer and the beginning of a second

shell. At that point, subsequent helium atoms are shielded from the monomer by the first shell atoms and the helium-helium interactions become more important. This same behavior was observed by Wu and Watts for a Xe atom embedded in helium clusters [55].

Figure 11.5 shows the approximate helium atom radial density profiles about the water monomer for cluster sizes of 6, 9, 12, and 15 helium atoms. Notice that the increase in the height of the peak is relatively constant from 6 to 12 helium atoms. From 12 to 15 helium atoms the increase in the peak height is not as great and the tail for the 15 helium atom distribution has increased relatively dramatically. Hence, the radial densities show that the first shell about the water monomer is becoming saturated and the second shell is beginning to form, which is consistent with the change in slope of the energy plots near 13 helium atoms.

11.0.3 Frequency Shifts

The frequency shifts for the asymmetric stretch are plotted as a function of cluster size in figure 11.6. The shifts were computed by taking the difference between the respective cluster size frequency and the isolated monomer frequency. The ground are converged to about 0.5 cm^{-1} and the excited state energies to about 0.3 cm^{-1} up to 10 helium atoms, so the shifts are converged to about 1 cm^{-1}. Consequently, taken individually, the shifts may not be significant. However, there is a clear trend towards

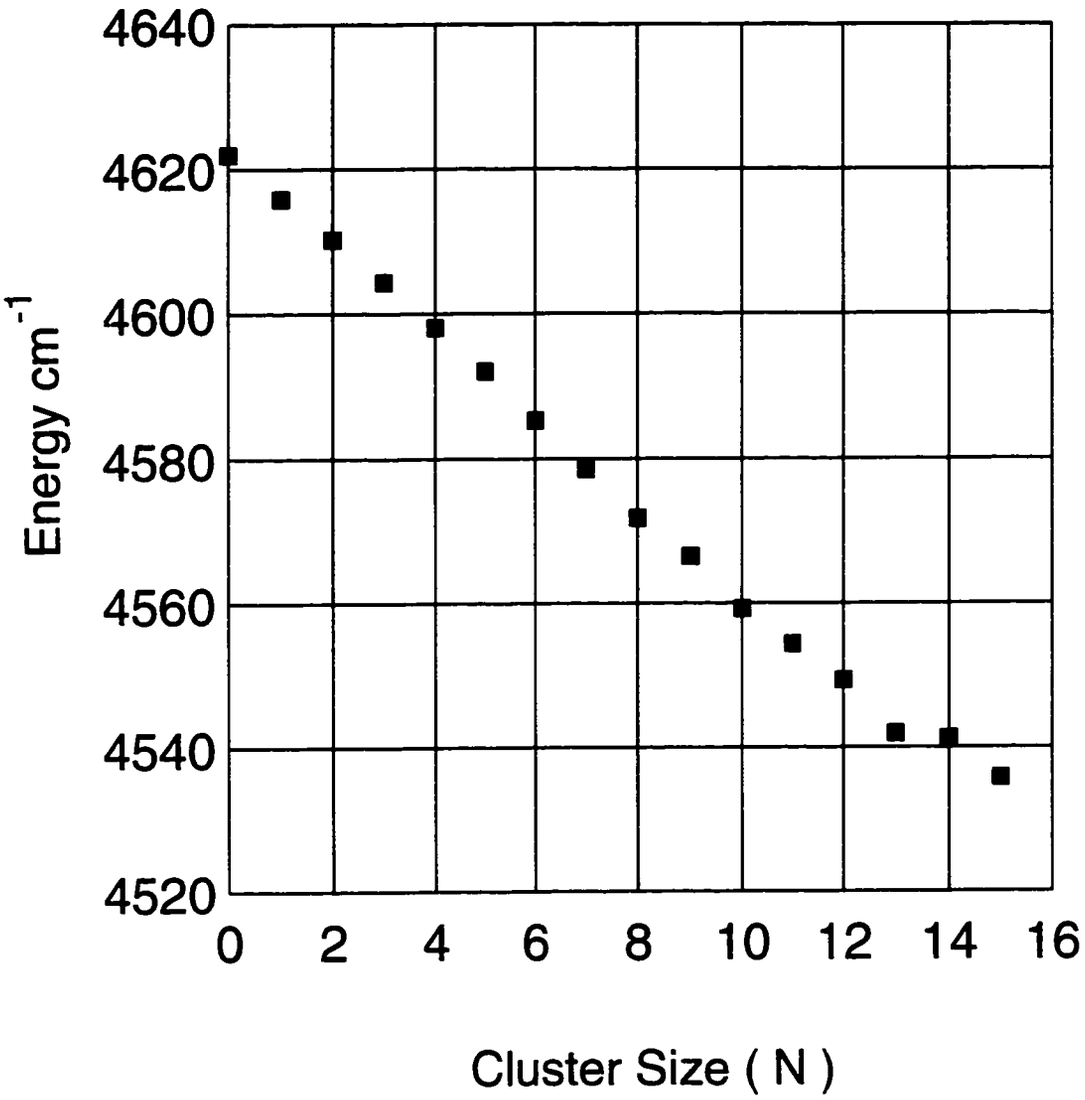

Figure 11.1: Ground State Energy as a function of cluster size.

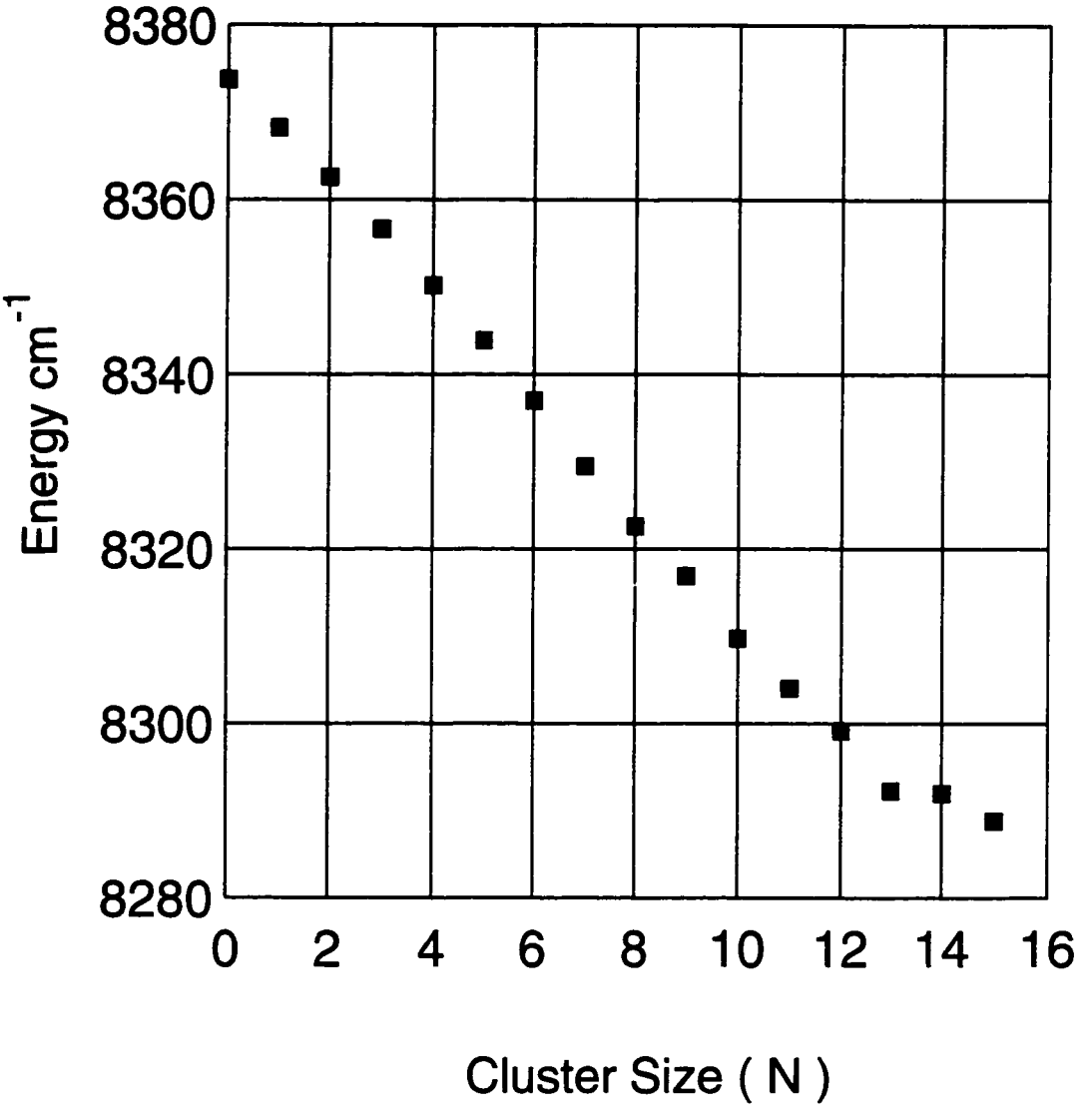

Figure 11.2: Asymmetric stretch fundamental energy as a function of cluster size.

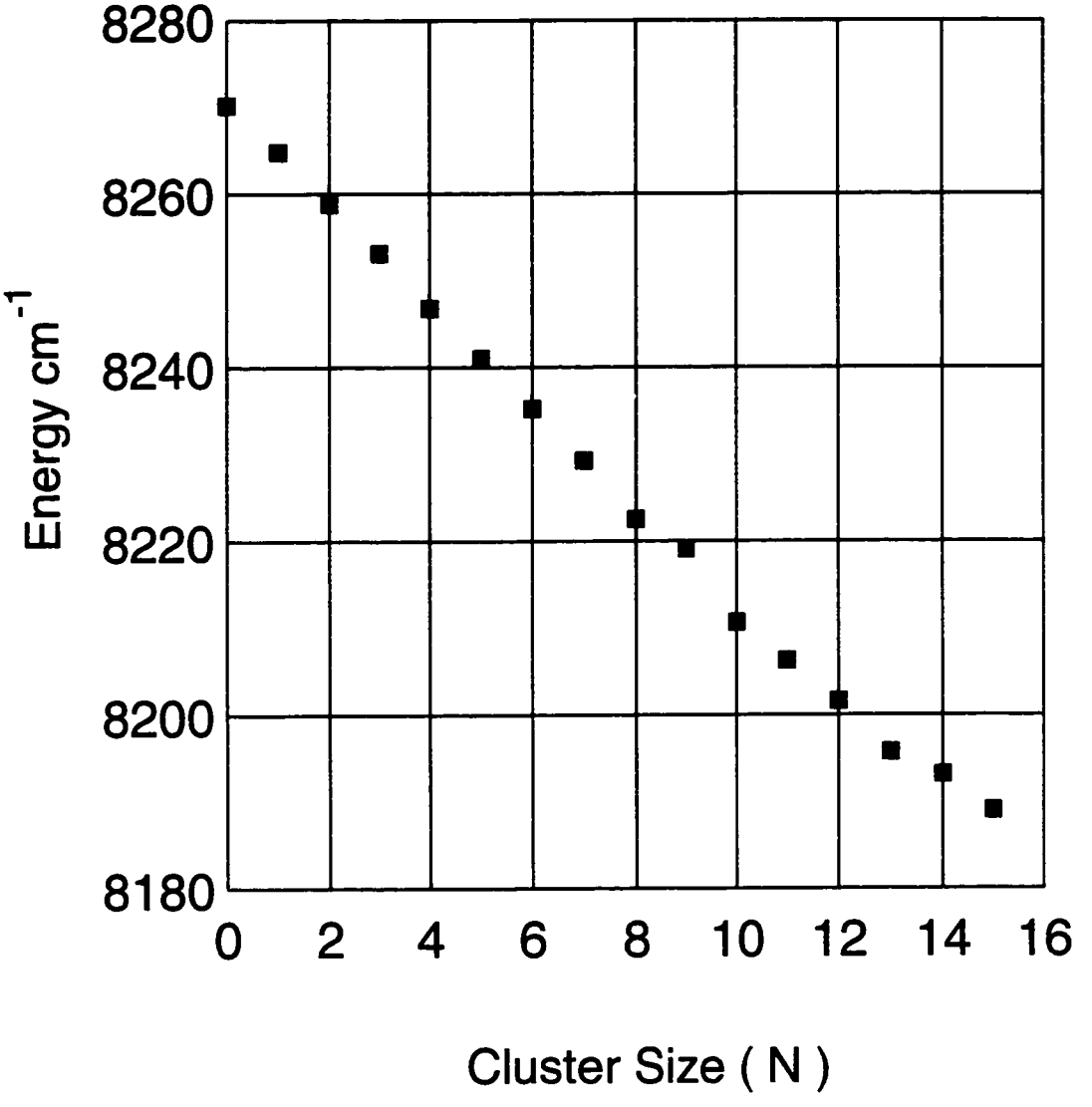

Figure 11.3: Symmetric stretch fundamental energy as a function of cluster size.

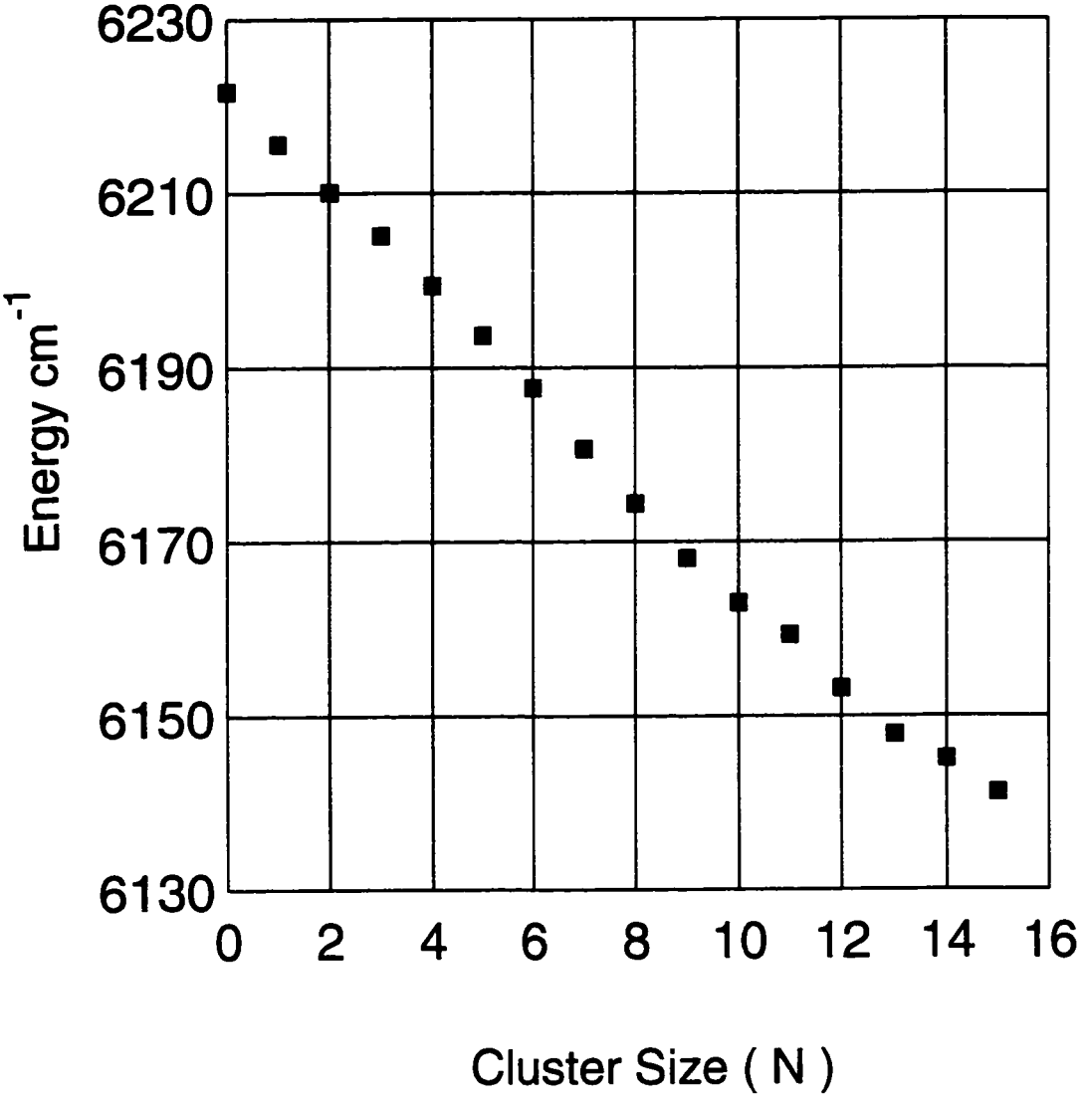

Figure 11.4: Bend fundamental energy as a function of cluster size.

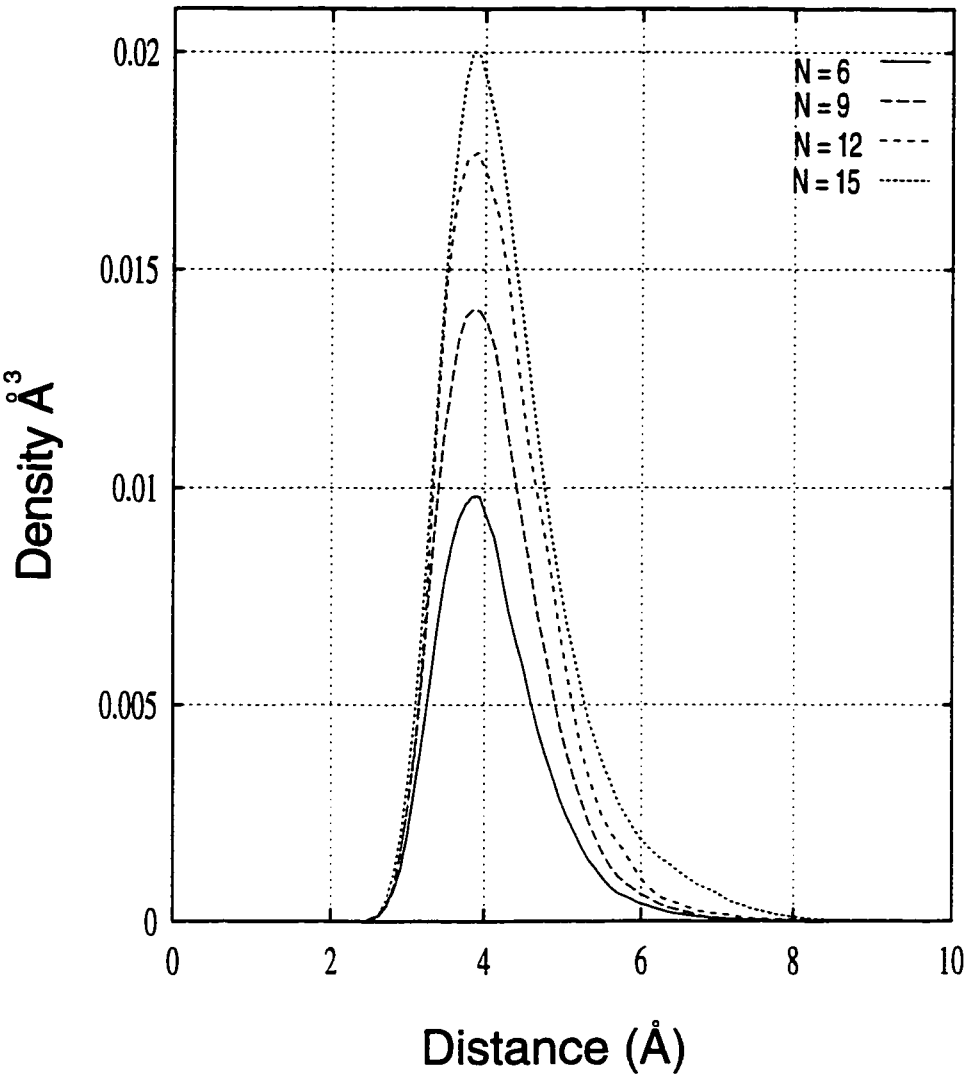

Figure 11.5: Approximate ground state radial density profiles for helium atom cluster sizes of 6, 9, 12, and 15 atoms.

a red shift and the magnitude agrees remarkably well with the experimental results of Huisken et. al. [56] who measured shifts of 1.5 cm^{-1} for a water monomer embedded in large helium clusters: their clusters were composed of 1000+ helium atoms. Although we are comparing small cluster results to large cluster measurements, it is not unreasonable. It is estimated that there are 10 to 20 helium atoms in the first shell surrounding the water monomer (as shown by the change of slope in the energy versus cluster size graphs), and the bulk of the perturbation to the water monomer vibrational frequencies is caused by these helium atoms. As a result, the shifts are expected to increase rapidly as the cluster size grows and to level off as the first shell saturates. This is the trend that is observed in our small cluster calculations. This behavior is supported by the work of Barnett and Whaley [30] in their perturbation study of SF_6 embedded in helium clusters. Their calculations showed a rapid increase in the frequency shifts from 1 to 20 helium atoms and much smaller increases after that. Their dipole-induced dipole mechanism shows that the shift depends on R^{-6}, with R being the distance of the helium atom from the center of mass of the SF_6; consequently, helium atoms beyond the first shell are not expected to perturb the impurity much.

We have attempted to extend our calculations to larger clusters, but the time required to achieve the desired convergence is far too long: on our IBM Risk 6000, Model 350's it took about 7 days to converge the 10 helium atoms cluster to 0.5 cm^{-1}.

The convergence scales as the inverse square root of the number of steps, making for a relatively rapid increase in computational expense; not to mention the fact that the larger clusters have greater fluctuations, which calls for a longer total imaginary time of propagation.

The shifts for the symmetric stretch and bend fundamentals are shown in figures 11.7 and 11.8. Somewhat surprisingly, both modes show shifts to the blue, which is the opposite of that observed for the asymmetric stretch. The shifts show a steady increase and appear to level off at around 4.0 to 6.0 cm^{-1}. The uncertainty for these results are the same as those for the asymmetric stretch. Both of these modes belong to the A_1 irreducible representation of the C_{2v} symmetry group, which may be the cause of their similar behavior. The blue shifts indicate a destabilization of the first fundamentals relative to the ground state.

In an effort to gain some insight into the shifts, we altered the mass of the cluster atoms while keeping the potentials the same. Several simulations were run for clusters containing 7 atoms. This size was chosen since it displayed significant shifts for the helium mass and was of a relatively small size: this keeps the total computation time down. Table 11.2 displays the results obtained. Both the bend fundamental and the symmetric fundamental are significantly affected by a change in the mass whereas the asymmetric fundamental remains relatively unchanged.

We also calculated various approximate structural properties of the cluster in-

cluding the average distance of a helium atom from the center of mass of the helium atoms, the distance of the water monomer from the helium center of mass, the average distance of a helium atom from the water monomer center of mass, and the average distance of a helium atom from the oxygen and from the hydrogen atoms. The results are shown in table 11.3. The water monomer is not located at the center of the helium clusters as seen by the displacement of the monomer from the cluster center of mass. Also, the helium atoms are on average closer to the oxygen atom than the hydrogens for all clusters shown. Consequently, the cluster is not isotropically distributed about the monomer, which most likely accounts for the difference in stability of the asymmetric stretch relative to the symmetric stretch and bend fundamentals.

Table 11.2: Energies and frequency shifts as a function of cluster atom mass. The cluster contained 7 atoms.

	Energy cm^{-1}				Frequency Shift cm^{-1}		
Mass m_e	Ground	Asym.	Sym.	Bend	Asym.	Sym.	Bend
3,674.3 (H_2)	4613.7	8365.3	8264.9	6213.9	-0.2	3.0	0.5
7351.7 (^{4}He)	4578.6	8329.5	8229.3	6180.6	-0.9	2.5	2.3
36,783.6 (Ne)	4542.1	8293.2	8198.5	6148.0	-0.7	8.2	6.2

Table 11.3: Approximate structural characteristics of the helium clusters for N = 6, 9, 12, and 15 helium atoms. Distances are in Å. C is the center of mass of the helium atoms.

N	He-C	He - H_2O	H_2O - C	He - H	He - O
6	4.0	4.3	1.4	4.4	4.3
9	4.2	4.3	1.0	4.4	4.3
12	4.4	4.5	0.8	4.6	4.5
15	4.6	4.6	0.6	4.7	4.6

11.0.4 Conclusions

We have shown that it is possible to calculate frequency shifts by simulating all degrees of freedom using DMC. However, it comes as no surprise that the computation is extremely intensive and subject to noise which is on the same scale as that of the shifts themselves. We calculated shifts for the first fundamentals of the asymmetric stretch, symmetric stretch, and the bend modes of a water monomer embedded in small helium clusters. We observed blue shifts for the symmetric stretch and bend fundamentals and a red shift for the asymmetric stretch.

Future research includes constructing more accurate trial functions and using these functions to study the structure of the clusters. More specifically, what is the mechanism causing the destabilization of the totally symmetric modes and the stabilization

of the asymmetric stretch? More accurate methods for the calculating the shifts are required so that the calculation may be extended to larger clusters. It remains to be seen if the shifts are truly significant and if they converge to the experimental results of Huisken et al.

Given the large difference between the intramolecular frequencies of the impurity and those of the intermolecular modes, adiabatic approaches are well suited to this problem. The water monomer could be held rigid in some configuration consistent with the mode of interest and a DMC simulation used to calculate the total energy. Since this is an adiabatic approach, it is able to use much larger time steps and achieve superior convergence at less computational expense. Then, the configuration could be varied and yet another calculation of the total energy performed. Thus, after multiple rigid body simulations, a discrete representation of the water monomer in the field of helium atoms is obtained. With the surface at hand, any basis set diagonalization scheme could determine energy levels and frequency shifts. This type of calculation is more accurate for these type of systems and is also able to handle much larger quantum clusters.

We would also like to conduct DMC simulations on this system at nonzero temperatures [57]. If helium is a superfluid for these clusters, would monitoring frequency shifts as a function of temperature show a change as a result of a lambda transition? If so, at what temperature would this occur?

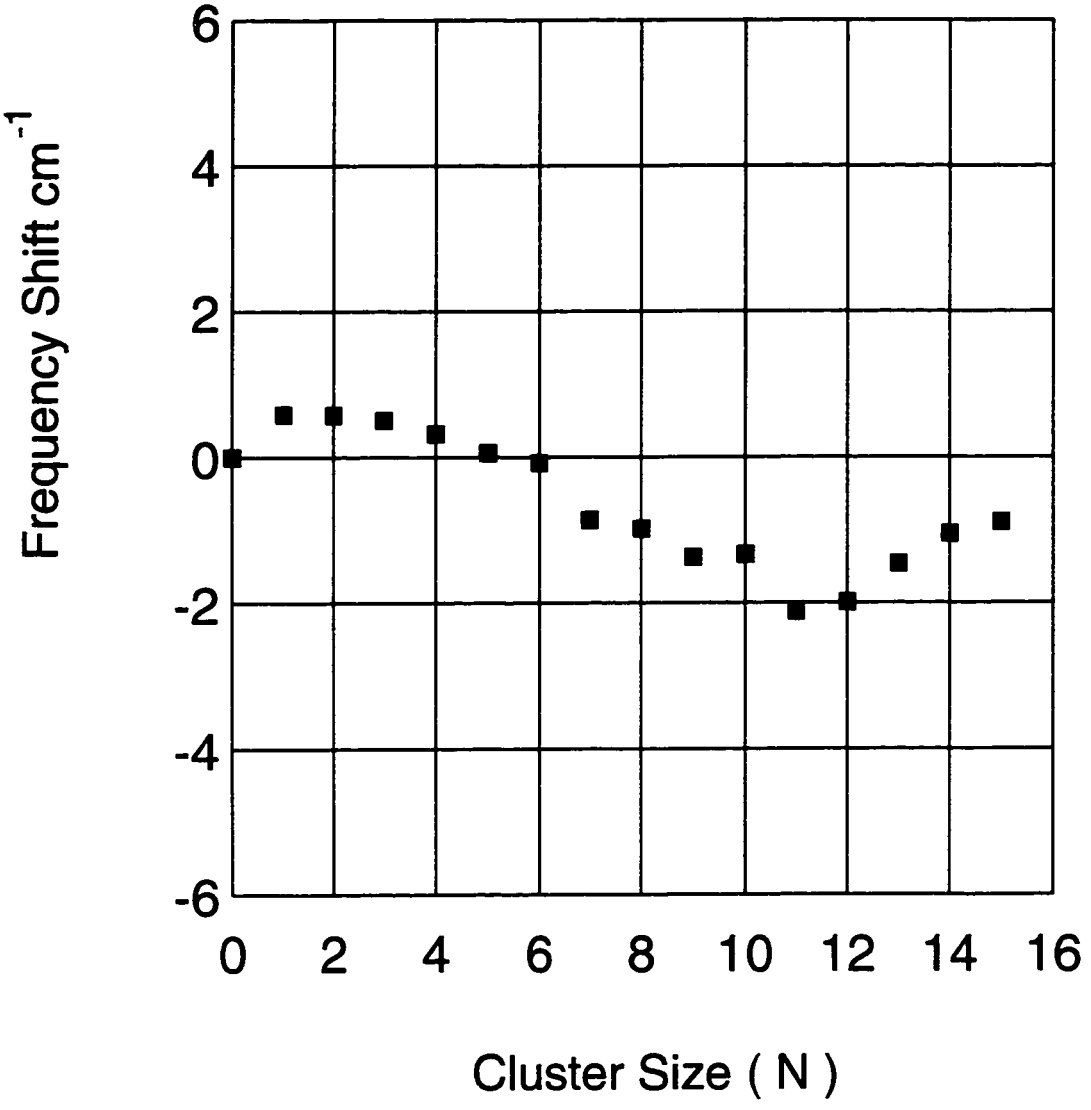

Figure 11.6: Asymmetric stretch fundamental frequency shift as a function of cluster size.

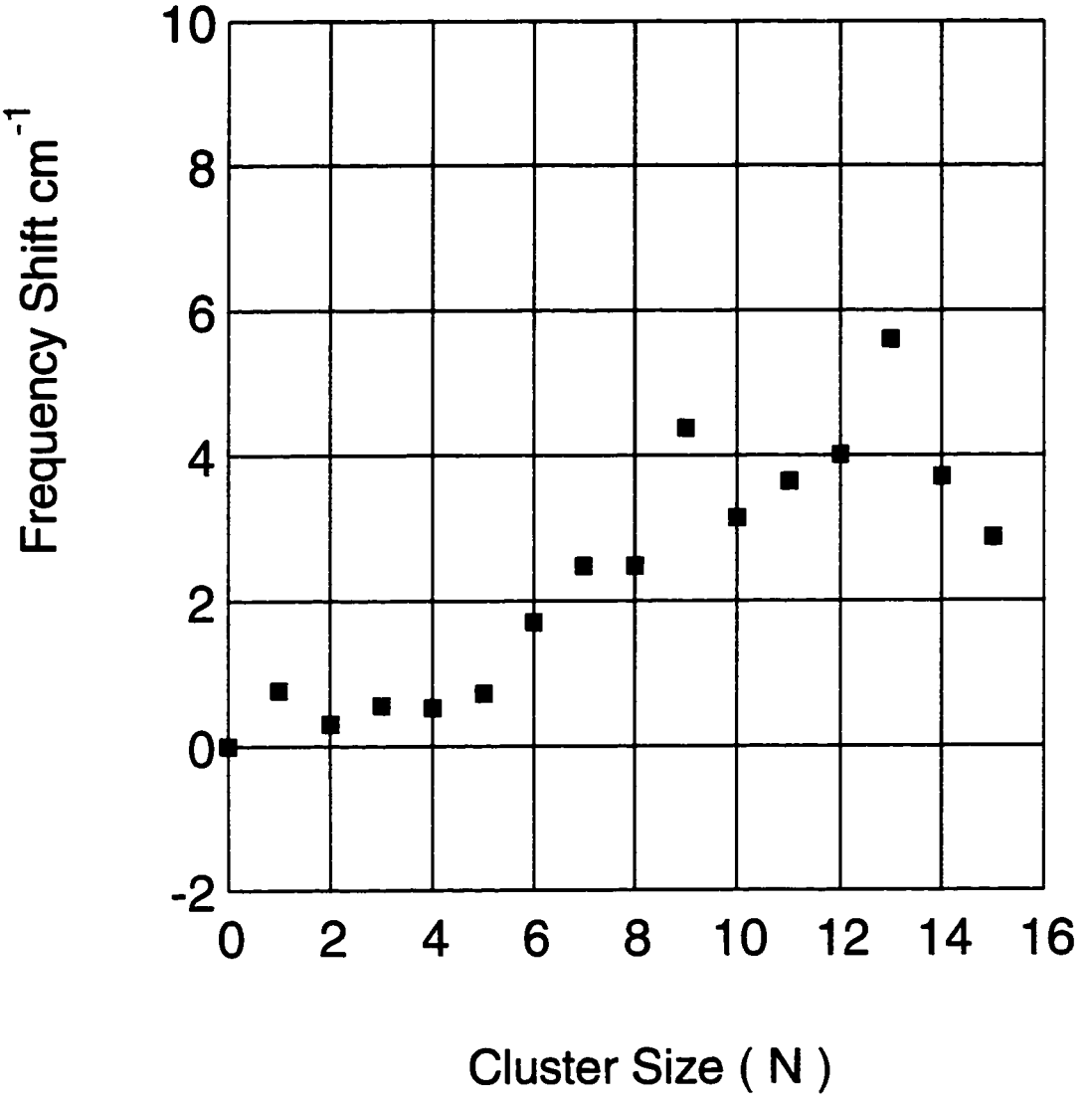

Figure 11.7: Symmetric stretch fundamental frequency shift as a function of cluster size.

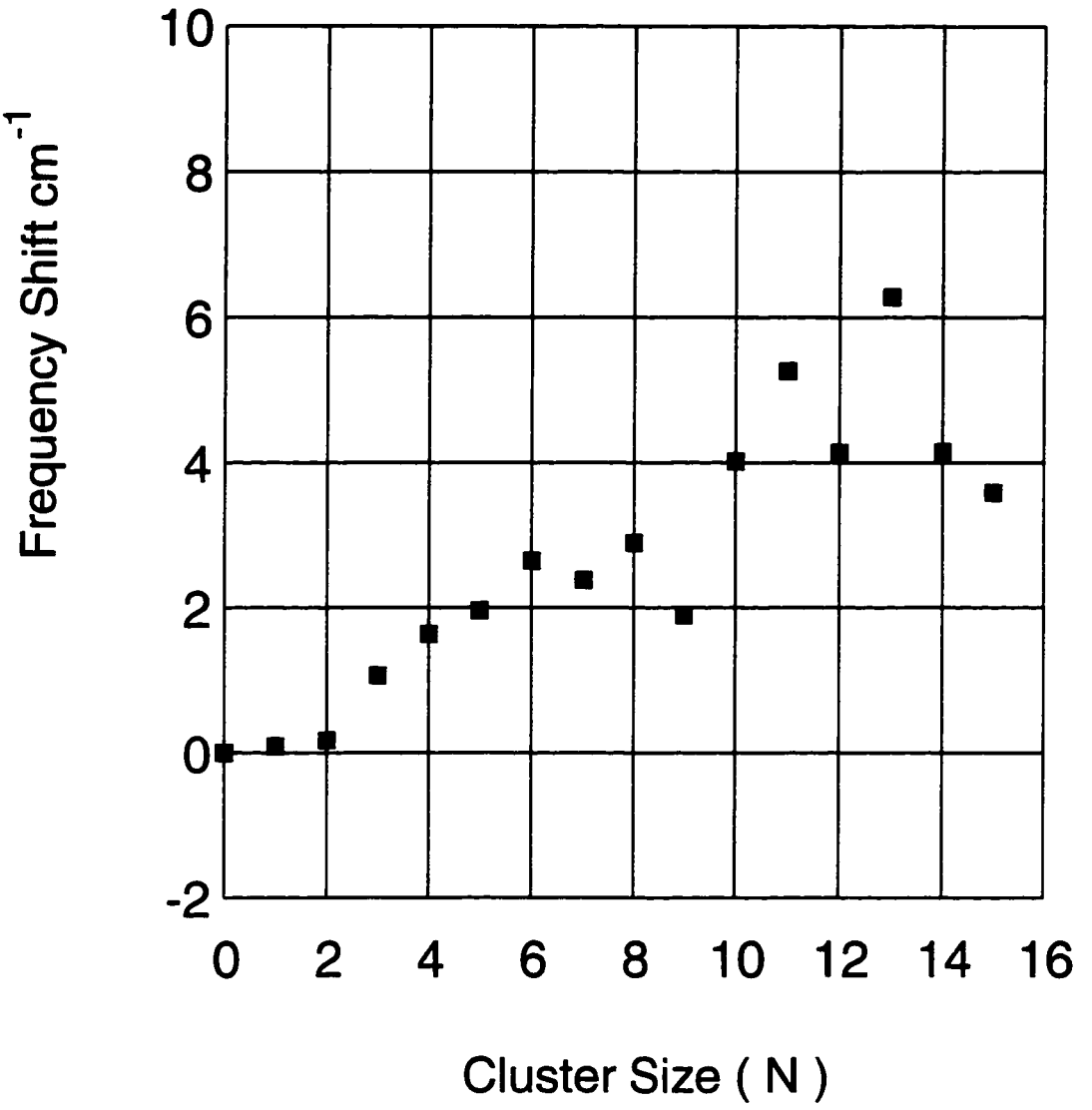

Figure 11.8: Bend fundamental frequency shift as a function of cluster size.

Bibliography

[1] E.J. Heller,*J. Chem. Phys.* **68**, 2066 (1978).

[2] E. Abramson, R.W. Field, D. Imre, K.K. Innes, and J.L. Kinsey, *J. Chem. Phys.* **83**, 453 (1985).

[3] P. Avouris, W.M. Gelbart, and M.A. El-Sayed *Chemical Reviews* **77** 793, (1977).

[4] G. Ewing, *J. Phys. Chem.* **91**, 4662 (1987).

[5] E.J.Heller, *J. Chem. Phys.* **92** 1718 (1990).

[6] E.J. Heller and R.C. Brown, *J. Chem. Phys.* **79**, 3336 (1983).

[7] P. M. Hunt, and M.S. Child *Chem. Phys. Letters* **58** 202 (1978).

[8] E. S. Medvedev, *Chem. Phys. Letters* **120** 173 (1985).

[9] W. H. Miller, *Adv. Chem. Phys.* **25**, 69 (1974).

[10] E. E. Nikitin, *Elementary Processes and Chemical Reactions*, Berlin-Heidelberg-New York (1968).

[11] L. D. Landau, E. M. Lifshitz,*Quantum Mechanics*, Oxford: Pergamon Press, Third Edition, (1977).

[12] B. I. Makshantsev, *Spectroscopy Lett.* **5** 1 (1972).

[13] M. Dantus, R.M. Bowman, J.S. Baskin, and A.H. Zewail, *Chem. Phys. Letters* **159**, 406 (1989).

[14] N.F. Scherer, R.J. Carlson, M. Alexander, M.Du, A.J. Ruggiero, V. Romero-Rochin, J. A. Cina, G.R. Fleming, and S.A. Rice, *J. Chem. Phys.* **95**, 1487 (1991).

[15] R. A. Mathies, C. H. Brito Cruz, W. T. Pollard, and C.V. Shank

[16] S. Kato, *J. Chem. Phys.* **88**, 3045 (1988).

[17] W. Siebrand, *J. Chem. Phys.* **46**, 440 (1967).

[18] K. Imre, E. Ozizmir, M. Rosenbaum, and R. F. Zweifel, *J. Math. Phys.* **8** 1097 (1967).

[19] B.R. Henry and W. Siebrand, *J. Chem. Phys.* **49**, 5369 (1968).

[20] I. M. Khalatnikov, *The Physics of Liquid and Solid Helium, Part I*, edited by K. H. Bennemann and J. B. Ketterson (Wiley, New York, 1976).

[21] J. P. Toennies, *Proceedings of the International School of Physics "Enrico Fermi", Course CVII, Varenna, June 28 - July 7, 1988 "The Chemical Physics of Atomic and Molecular Clusters"*, North Holland, 597-617 (1990).

[22] R. S. Kagiwada, J. C. Fraser, I. Rudnick and D. Bergman, *Phys. Rev. Let.* **22**, 338 (1969).

[23] P. Sindzingre, M. L. Klein, and D. M. Ceperley, *Phys. Rev. Let.* **63**, 1601 (1989).

[24] M. V. R. Krishna and K. B. Whaley, *Phys. Rev. Lett.* **64**, 1126 (1990).

[25] A. Scheidemann, J. P. Toennies, and J. A. Northby, *Phys. Rev. Let.* **64**, 1899 (1990); A. Scheidemann, B. Schilling and J. P. Toennies, *J. Phys. Chem.* **97**, 2128 (1993).

[26] U. Buck and H. Meyer, *Phys. Rev. Let.* **52**, 109 (1984); Surface Sci. **156** 275 (1985).

[27] M. Lewerenz, B. Schilling, and J. P. Toennies, *Chem. Phys. Let.* **206**, 381 (1993).

[28] M. R. Zakin and D. R. Herschbach *J. Chem. Phys.* **85**, 2377 (1986).

[29] D. Eichenauer and R. J. LeRoy, *J. Chem. Phys.* **88** 2898 (1988).

[30] R. N. Barnett and K. B. Whaley, *J. Chem. Phys.* **99**, 9730 (1993).

[31] A. D. Buckingham, it Trans. Faraday Soc. **56**, 753 (1960); *Proc. Roy. Soc. A.* **248**, 169 (1957).

[32] D. F. R. Brown, J. K. Gregory and D. C. Clary, *to be published.*

[33] R. O. Watts and M. A. Suhm, *Phys. Rep.* **204**, 293 (1991).

[34] W. L. McMillan, *Phys. Rev.* **138**, A442 (1965).

[35] J. B. Anderson, *J. Chem. Phys.* **63**, 1499 (1975).

[36] J. B. Anderson, *J. Chem. Phys.* **65**, 4121 (1976).

[37] J. B. Anderson, *J. Comp. Phys.*, **31**, 425 (1979); *J. Chem. Phys.* **73**, 3897 (1980); *J. Chem. Phys.* **82**, 2662 (1985).

[38] M. H. Kalos, *Phys. Rev.* **128**, 1791 (1962); J. Comp. Phys. **2**, 257 (1967); *Phys. Rev. A.* **2**, 250 (1970).

[39] M. H. Kalos, D. Levesque and L. Verlet, *Phys. Rev. A.* **9**, 2178 (1974).

[40] C. J. Umrigar, M. P. Nightingale and K. J. Runge, *J. Chem. Phys.* **99**, 2865 (1993).

[41] D. M. Ceperley and B. Alder, *Science* **231**, 555 (1986).

[42] D. M. Ceperley and B. J. Alder, *J. Chem. Phys.* **81**, 5833 (1984).

[43] D. M. Ceperley and B. Bernu, *J. Chem. Phys.* **89**, 6316 (1988); B. Bernu, D. M. Ceperley and W. A. Lester, *J. Chem. Phys.* **93**, 552 (1990).

[44] A. Palma, S. Green, D. J. Defrees and A. D. McLean, *J. Chem. Phys.* **89**, 1401 (1988).

[45] S. Green, D. J. Defrees, and A. D. Mclean, *J. Chem. Phys.* **94**, 1346 (1991).

[46] S. Maluendes, A. D. Mclean, and S. Green, *J. Chem. Phys.* **96**, 8150 (1992).

[47] R. A. Aziz, F. R. W. McCourt and C. C. K. Wong, *Mol. Phys.* **61**, 1487 (1987).

[48] J. R. Reimers and R. O. Watts, *Mol. Phys.* **52**, 357 (1984).; J. R. Reimers, R. O. Watts and M. L. Klein, *Chem. Phys.* **64**, 95 (1982).

[49] R. E. Miller, D. F. Coker, and R. O. Watts, *J. Chem. Phys.* **82**, 3554 (1985); D. F. Coker and R. O. Watts, *J. Phys. Chem.* **91**, 2513 (1987).

[50] C. W. Robertson and D. Williams, *J. Opt. Soc. Am.*, **61**, 1316 (1971)

[51] D. F. Coker and R. O. Watts, Mol. Phys. **58**, 1113 (1986).

[52] H. Sun and R. O. Watts, *J. Chem. Phys.* **92**, 603 (1990); M. Quack and M. A. Suhm, Mol. Phys. **69**, 791 (1990).

[53] M. V. R. Krishna and M. V. Whaley, *J. Chem. Phys.* **93**, 6738 (1990).

[54] M Lewerenz and R. O. Watts, *unpublished.*

[55] J. Wu and R. O. Watts, thesis.

[56] F. Huisken, *Max-Planck-Institut für Strömungsforschung, Bunsenstrasse 10, D-37073 Göttingen, FRG*, private communication.

[57] D. F. Coker and R. O. Watts, *J. Phys. Chem* **91**, 4866 (1987).

VITA

Douglas Beck was born in Renton, Washington in 1966. He attended Oliver M. Hazen High school and from there went on to attend Whitman College. He graduated from Whitman in May of 1988 with a B.A. in Chemistry. He then enrolled in a Ph.D. program in chemistry at the University of California, Riverside. For many reasons, he left Riverside at the end of the first quarter and returned to the Seattle area. From there he applied to the chemistry program at the University of Washington and began the program in September of 1989. Doug began work under the supervision of E. J. Heller which continued until April of 1994. He left the Heller group after his advisor moved to Harvard University. He then began a new project under the supervision of Robert O. Watts and will receive his Ph.D. in June of 1996.